NONLINEAR TIME-FREQUENCY CONTROL OF PERMANENT MAGNET ELECTRICAL MACHINES

A Dissertation

by

XIN WANG

Submitted to the Office of Graduate and Professional Studies of
Texas A&M University
in partial fulfillment of the requirements for the degree of

DOCTOR OF PHILOSOPHY

Chair of Committee,	C. Steve Suh
Committee Members,	Alan Palazzolo
	Mehrdad Ehsani
	Reza Langari
Head of Department,	Andreas A. Polycarpou

December 2017

Major Subject: Mechanical Engineering

ABSTRACT

Permanent magnet (PM) electrical machines have been widely adopted in industrial applications due to their advantages such as easy to control, compact in size, low in power loss, and fast in response, to name only a few. Contemporary control methods specifically designed for the control of PM electrical machines only focus on controlling their time-domain behaviors while completely ignored their frequency-domain characteristics. Hence, when a PM electrical machine is highly nonlinear, none of them performs well.

To make up for the drawback and hence improve the performance of PM electrical machines under high nonlinearity, the novel nonlinear time-frequency control concept is adopted to develop viable nonlinear control schemes for PM electrical machines. In this research, three nonlinear time-frequency control schemes are developed for the speed and position control of PM brushed DC motors, speed and position control of PM synchronous motors, and chaos suppression of PM synchronous motors, respectively. The most significant feature of the demonstrated control schemes are their ability in generating a proper control effort that controls the system response in both the time and frequency domains. Simulation and experiment results have verified the effectiveness and superiority of the presented control schemes. The nonlinear time-frequency control scheme is therefore believed to be suitable for PM electrical machine control and is expected to have a positive impact on the broader application of PM electrical machines.

ACKNOWLEDGEMENTS

I would like to express my sincere appreciation to my supervisor and committee chair, Dr. C. Steve Suh, not only for his support and insightful instruction, but also for bringing me to the world of nonlinear time-frequency control. His idea in control has completely changed my opinion about modern control theory and I really love the research I was doing. In addition, I really appreciate him for guiding and encouraging me when I encountered difficulties.

I would also like to thank my committee member, Dr. Alan Palazzolo, Dr. Mehrdad Ehsani, and Dr. Reza Langari, for their generous advice and suggestion throughout the course of this research.

I also wish to thank the Texas A&M University for providing me excellent education resources and great research environment. Many thanks also go to my friends and colleagues for their companion and assistance.

Finally, I wish to thank my parents. Without their unconditional love and support, my life at A&M would not be the same.

CONTRIBUTORS AND FUNDING SOURCES

Contributors

This work was supervised by a dissertation committee consisting of Professor C. Steve Suh, Professors Alan Palazzolo and Reza Langari of the Department of Mechanical Engineering and Professor Mehrdad Ehsani of the Department of Electrical & Computer Engineering.

All work for the dissertation was completed independently by the student.

Funding Sources

There are no outside funding contributions to acknowledge related to the research and compilation of this document.

TABLE OF CONTENTS

Page

Page

LIST OF FIGURES

Page

Page

Page

Page

Page

Page

Page

Page

Page

Page

Page

LIST OF TABLES

Page

Page

Page

1. INTRODUCTION*

1.1 Overview and Literature Review

Electrical machines are widely used in various applications due to the convenience and low cost of electric energy. In recent years, with the evolution of permanent magnet materials, especially high-intensity permanent magnet materials, PM electrical machines have become increasingly popular. In PM electrical machines, field windings necessary for non-PM electrical machines (wound-field brushed DC motors, induction motors, etc.) are replaced with permanent magnets thus rendering them possess the merits of ease in control, compact in size, low in power loss, and fast in response, to name only a few.

Currently, PM brushed DC motors and PM synchronous motors are the two common types of PM electrical machines available in the market. Among them, PM brushed DC motors are a mature technology and have seen extensive applications since their debut around 60 years ago [1]. Although it is well-known that motors of this type often suffer from wearing at the brush-and-commutator interface [2], comparing with other options, PM brushed DC motors still possess unique benefits and thus continue to be a favorable choice for industrial applications.

Specifically speaking, systems adopting PM brushed DC motors are less complex for power conversion. Unlike AC motors and brushless DC motors which require intricate inverters, machines using PM brushed DC motors only require a single converter for rectification. The implications of this are smaller sizes, less heat losses, easier maintenance and the ability to operate under harsh conditions. Since the stator field windings in conventional brushed DC motors are replaced with permanent magnets, PM brushed DC motors lack armature interaction and hence are capable of providing high starting and acceleration torques (up to 1,000% of the rated value). This unique characteristic qualifies them as the perfect contender for applications where temporary power burst is needed. In addition, the cost of PM brushed DC motors is generally the lowest compared with other types of motors. Being the primary adjustable speed drives for decades, much focus has been given to improve their performance. The effort of designing smaller commutators, adopting longer brushes, adding brush wear sensors, and reducing the difficulty of brush/commutator replacement have greatly enhanced the performance of PM brushed DC motors and minimized the maintenance cost.

Contemporary research on PM brushed DC motor control has mainly focused on formulating control schemes that are fast, accurate, robust and efficient under system uncertainties. Even though brushed DC motor with permanent magnet is almost a linear system due to the elimination of the nonlinear field flux versus armature current magnetization characteristic, it would still demonstrate strong nonlinearity when afflicted by disturbance such as noise. To address such undesirable behavior, a properly designed controller is essential. Common techniques applicable to PM brushed DC motor control

include PID control, adaptive PID control, fuzzy logic control (FLC), and model reference adaptive control (MRAC), to name only a few.

PID control is popular due to its simplicity and reliability. The algorithm employs a proportional term, an integral term, and a derivative term to calculate appropriate control effort based on the exact value of present error, the accumulation of past error, and the prediction of future error, respectively. In Reference [3], Sabir and Khan explored the possibility of using metaheuristic techniques to replace classical PID tuning method for DC motor speed control. They demonstrated that with the metaheuristic algorithm, the performance of the optimized PID was much better than classical algorithms. In Reference [4], Pérez-Molina and Pérez-Polo studied the dynamics of a DC servomechanism with cubic nonlinearity and developed a procedure to choose the PID gains such that the system could reach steady-state even in the presence of noise. In general, PM brushed DC motors with PID controller could achieve ideal performance if the controller gains are well tuned. However, since PID controller is a linear controller, and in particular symmetric, its performance under complex working conditions remains an issue.

Adaptive PID control is an update over the conventional PID control. PID parameters in this algorithm are adjusted on-line following an appropriate scheme to be adaptable to system variations. In Reference [5], Reza et al. suggested a self-tuning PID with fuzzy logic for DC motor speed control. They illustrated through a series of simulations that by combining two self-tuning PIDs with error and integral error as inputs, system response could be significantly improved. In Reference [6], Hsu and Lee presented an adaptive PID control algorithm exploiting sliding mode control for the position control

of a rotor. The algorithm utilized both fuzzy compensator and gradient descent method to attain system stability in the Lyapunov sense. Experimental results show that the algorithm is suitable for DC servo system. However, even though results obtained with adaptive PID control seem to be promising, this approach is still a PID control. It shares the same downsides of PID control. When DC motor systems are highly nonlinear, adaptive PID controllers irrevocably underperform. In addition, accuracy and rapid response usually cannot be coordinated well in adaptive PID control scheme, especially under wide system variations.

FLC is a favorable choice for nonlinear system due to its flexibility in design, tolerance to imprecise data, independence on modeling, and ability to incorporate human experience. FLC controllers usually consist of an input stage, a processing stage, and an output stage [7, 8]. The input stage maps the controller inputs, such as speed and position, to the appropriate membership functions and truth values. The processing stage invokes the relevant fuzzy rules corresponding to the mapped inputs, generates a fuzzy set for each rule, and then combines all the fuzzy sets into a single fuzzy set. Finally, the output stage converts this single fuzzy set into a specific control output value. In Reference [9], Murugananth and Vijayan introduced a 56-rule fuzzy logic controller for the speed control of a PM brushed DC motor in an orthopedic surgical simulator and achieved satisfactory results in the presence of external loadings. In Reference [10], Prasad and Nair evaluated the performance of a 25-rule fuzzy logic controller against a conventional PID controller for the position control of a DC motor. The controller is shown to be superior to the PID controller in the presence of constant torque. However, to achieve optimal performance in

a broad operation range, the number of fuzzy rules required in FLC could be formidably huge, thus preventing it from been widely adopted in practical applications. In addition, since the design of fuzzy rules is mainly based on the specific behavior of the system and designer's personal experience, tuning of fuzzy logic controller oftentimes can be tedious and time-consuming. Moreover, due to its inherent operating mechanism, fuzzy logic control is vulnerable to noise.

Unlike FLC, which adopts a trial-and-error design approach, the plant parameters in MRAC are first estimated on-line using measured system signals. These estimated parameters are then used to compute appropriate control inputs following a specific algorithm. This advantageous feature makes MRAC suitable for DC motor control when the majority parameters are unavailable and the external loading varies with time. In Reference [11], Prakash and Vasanthi proposed a neural network based MRAC to improve the speed tracking performance of a DC motor. The results show that the proposed compensator was superior to the conventional MRAC scheme, especially at low speed. In Reference [12], Sun et al. presented a novel MRAC with external filter. The illustrated control strategy not only ensures the real system has similar performance with the desired system, but also guarantees satisfactory robustness by avoiding a large adaptation gain. Simulation results on a positioning motion system driven by a DC motor verifies the effectiveness of the proposed scheme. However, to achieve satisfactory performance under a wide operation range, the required adaptive algorithm in MRAC would be too involved to be practical. When the motor system experiences an abrupt change in the

external torque load, MRAC would display overshoot during transient and cause undesirable oscillations in motor speed and output torque.

As for PM Synchronous motor, comparing with its main competitor - AC induction motors, PM synchronous motors have the advantages of low inertia, compact size, strong air-gap flux, and high efficiency due to the absence of rotor coils [13, 14]. These distinguished features renders it suitable for motion control applications where efficiency and precision are of paramount concern.

PM synchronous motor is intrinsically a nonlinear, multivariable, and highly coupled system due to its complex structure and sophisticated operating principle. In order for it to achieve satisfactory dynamic performance, advanced control algorithms are essential. Of the numerous methods proposed for the control of PM synchronous motors, scalar control, filed oriented control (FOC), and direct torque control (DTC) are the most widely recognized. Among them, scalar control, also named V/f control, is the simplest. It maintains a constant relationship between the stator voltage amplitude and frequency, which in turn guarantees that the motor air gap flux stays at the desired steady-state value. In Reference [15], Perera et al. proposed a sensorless, stable V/f speed control method for PM synchronous motor without damper windings. They illustrated that by adjusting the ratio of the applied voltage frequency to the perturbation in the input power, stable operation of the motor can be realized under a wide speed range. In Reference [16], Ancuti et al. presented a fast and robust V/f control approach that implicitly provided maximum torque per ampere through regulating the interior reactive power using two stabilizing loops for a high-speed surface mounted PM synchronous motor. In Reference [17],

Agarlita et al. introduced another stable V/f control for PM synchronous motors with an active power variation based voltage-vector speed correction loop and a controlled power factor angle based voltage amplitude correction loop. Results showed that the proposed scheme has satisfactory performance under both steady and transient states. In Reference [18], Consoli et al. demonstrated a novel V/f control which extends the energy-saving capability of an interior-mounted PM synchronous motor to flux weakening and maximum torque per ampere/voltage regions through assigning polynomial relationships between the operating angles of the motor. They demonstrated that the system efficiency is greatly improved compared to that of the standard V/f control. However, in essence, scalar control is simply a rough approximation method. Incorporating extra stabilizing loops or error corrections does not guarantee better performance for precise PM synchronous motor control, let alone that system complexity and unreliability are also greatly increased during this process.

Field oriented control, also referred to as vector control, is a popular PM synchronous motor control scheme. In this scheme, the stator phase winding parameters are transformed from a three-phase static reference frame into a two-axis rotating reference frame which rotates synchronously with the rotor. Such a coordinate transformation not only eliminates the sinusoidal changing property of stator parameters, but also expresses the motor model in a mutually decoupled two-axis reference frame (*d*-*q* reference frame) [19]. By controlling the stator current component along each axis individually, proper control of a PM synchronous motor can be achieved. Standard FOC is based on three PI controllers which controls the rotor speed, *d*-axis current, and *q*-axis

current, respectively. The two PI controllers controlling rotor speed and *q*-axis current are cascaded. Since the electrical inertia of the two current loops are much smaller than the mechanical inertia of the speed loop, the two current loops in FOC runs much faster than the speed loop [20]. In Reference [14], Vu et al. replaced the PI controller for speed control in classical FOC with a certainty equivalence principle based adaptive speed controller. Experimental results show that the designed adaptive control law is insensitive to motor parameter and torque load variations. In Reference [21], Ananthamoorthy and Baskaran used a hybrid fuzzy logic controller as the speed controller in FOC and achieved satisfactory dynamic response. In Reference [22], Alexandrous et al. presented a novel predictive current controller which combines deadbeat and direct predictive control for high performance PM synchronous motor control. The proposed predictive current controller replaces the two PI controllers used for current control in the standard FOC and only one PI controller is used for the speed control loop. In Reference [23], Mynar et al. presented a linearized reference model based model predictive controller for high quality PM synchronous motor control. The introduced controller is multiple inputs and multiple outputs which completely replaces the PI controllers in the traditional FOC. However, even though FOC is capable of providing smooth and reliable operation, the high computational complexity involved in coordinate transformation restricts its applicability in super high speed PM synchronous motors.

Rather than controlling the V/f ratio in scalar control or the current components in FOC, DTC controls the motor torque and flux directly in which the stator flux and output torque are first calculated online using measured stator voltages and currents.

Subsequently, the estimated flux and torque are compared with their reference values simultaneously. If either one deviates from their reference values more than a specified range, certain stator voltage vectors are applied to the motor following a predefined look-up table to force the flux and torque to return to their tolerant band at the first opportunity. Therefore, DTC can be considered as a combination of space vector modulation and hysteresis band control. In Reference [24], Zhang et al. applied two kinds of neural network controllers, namely, radial basis function based and back-propagation based, to the DTC of an interior mounted PM synchronous motor. The added neural network controller in the DTC scheme functioned as a replacement for the switching table. Results showed that both neural network controllers had a significant advantage over the traditional switching table based DTC topology and that the neural network with the radial basis function provided the best performance. In Reference [25], Song et al. proposed an adaptive fuzzy control based DTC that can effectively improve PM synchronous motors' performance using an enhanced algorithm that optimizes the efficiency of both computation and transformation of the fuzzy rules. In Reference [26], Preindl and Bolognani designed a novel model predictive DTC with a finite control set. At each sampling period, the future behavior of the motor was predicted using a discrete-time state-space model in the *d*-*q* reference frame and the corresponding control voltage vectors were selected based on a predefined cost function. Physical results confirmed that the controller was satisfactory in performance with respect to both dynamic and steady-state operations. In Reference [27], Sivaprakasam and Manigandan presented three modified DTC schemes to reduce the torque ripple and mechanical vibration in a PM synchronous

motor. In the proposed DTC schemes, the two-level inverter commonly adopted in classical DTC was first replaced with a three-level neutral point clamped inverter that provided 27 available voltage vectors. These 27 voltage vectors were then separated and formed three different groups. Three particular switching tables were designed for each group and formed the core of the modified DTC scheme. All the three DTC schemes were effective in reducing torque ripple and mechanical vibration than the classical DTC topology. However, even though DTC scheme has a fast and robust dynamic response compared with V/f control and FOC, the stringent requirement for high accuracy current measurement restricts its performance under complex working conditions. Besides, as DTC is a switching table based control method, it is difficult to integrate it with other advanced control techniques.

Evidently, the aforementioned PM synchronous motor control schemes all have their individual pros and cons and should be chosen depending on the application. However, neither of them is applicable to a particular challenge in PM synchronous motor control. That is, in the event that the corresponding parameters fall into a certain range, a PM synchronous motor could behave chaotically with the output torque changing haphazardly and motor speed oscillating over a wide range. Such an occurrence could gravely degrade the stability and controllability of the PM synchronous motor, thus inevitably compromising its performance.

Techniques applied to mitigate chaotic responses in PM synchronous motors include feedback linearization, time-delayed feedback, Takagi-Sugeno fuzzy control, sliding-mode control, adaptive control, back-stepping control, and dither signal injection.

Feedback linearization is a method which reduces a nonlinear system to a fully controllable linear system through change of coordinates and transformation of feedback, thus allowing the resulted close-loop dynamics to be completely manipulated using common linear control theories. In Reference [28], Ren and Liu eliminated the coupling terms in the motor equations using feedback linearization and the resultant system was able to reach stable equilibrium using simple proportional controllers. However, this approach suffers from not being able to control the aperiodic behaviors of the PM synchronous motor globally.

Time-delayed feedback is another powerful control tool which stabilizes the unstable fixed points or periodic orbit of a chaotic system through constructing a proper control law using the difference between the present state and the delayed state of the given chaotic system [29]. In Reference [30], Ren et al. used stator current based delay feedback to control chaos in a PM synchronous motor. Simulation results verified the effectiveness of the proposed method. While easy to implement and practical for controlling systems of fast dynamics, this approach is not popular due to the difficulty in determining the required time-delay and the strict requirement for the desired response.

Takagi-Sugeno fuzzy control [31] has been extensively studied for the chaos control in PM synchronous motors. Its basic idea is that through decomposing a given nonlinear system into several linear systems via a set of fuzzy rules, the global control objective can be achieved by controlling each subsystem with appropriate local components. In Reference [32], Hou designed a guaranteed cost control for the asymptotic stabilization of a chaotic PM synchronous motor via Takagi-Sugeno fuzzy method. The

designed controller is based on Lyapunov stability theory and linear matrix inequality technique and simulation results verified the validity of the proposed controller. In general, nonlinear system described by Tagagi-Sugeno fuzzy rules is suitable for stability analysis and hence is easy to combine with other control methods. Nevertheless, due to the complex chaotic nature of the PM synchronous motor, the number of fuzzy rules required to represent the motor system is too large to be realized.

Sliding-mode control is well-known for its robustness in response to system parameter variation and external disturbance. This method starts from choosing a sliding-mode surface, followed by designing an appropriate control input which forces the system output to move towards the sliding-mode surface. In Reference [33], Yang et al. proposed a fuzzy sliding-mode controller to control chaos in PM synchronous motors. The designed sliding control law consists of a feedback linearization controller and a robust controller. Its effectiveness is validated through a series of simulations. Even though systems with sliding-mode control are of fast response, satisfactory transient performance, and low order, to guarantee robustness, a large control gain is necessary, thus risking causing the so-called chatter. In addition, it is difficult to determine an appropriate sliding-mode surface for a chaotic system.

Characterized by estimating parameters of both the plant and controller on-line, adaptive control is widely applied to suppress chaos in systems where physical models are incomplete and corresponding parameters are unavailable. In Reference [34], Hu et al. presented an adaptive nonlinear feedback controller to eliminate chaos in PM synchronous motors. The designed controller could estimate system parameters on-line and generate

appropriate control forces. While suitable for system suffers from parameter uncertainty and disturbance, when system are highly chaotic, adaptive controller would display large overshoots during transient.

Back-stepping control decomposes a complex dynamic system into subsystems that can be stabilized using other methods. Because of the recursive structure, back-stepping controller can be designed from known stable subsystems and "back out" new controllers which progressively stabilize each outer subsystem. The final controller is an integration of all the individual controllers for each subsystem. In Reference [35], Harb presented a nonlinear controller using back-stepping control to mitigate chaos induced in PM synchronous motors. The performance of the proposed design was validated through comparing with sliding mode control. Though systems adopting this method oftentimes demonstrate satisfactory control performance subject to parameter uncertainty, it usually requires tedious design process to reach a final controller design that can be too involved to be practical if the dynamics of a given PM synchronous motor system is highly chaotic.

Dither signal injection is a relatively new approach for the suppression of chaos in PM synchronous motors. This method is based on the discovery that the injection of an external high frequency dither signal has the effect of improving the performance of a nonlinear system. Ideal control effects can be realized through manipulating the frequency and amplitude of the external dither signals without the need to engage in other measures. In Reference [36], Wei and Wang studied the effect of sinusoidal dither signal with difference frequencies on the chaos control of PM synchronous motor and the results turns

out to be promising. However, as an open-loop approach, this method lacks the adjustability and flexibility needed for chaos control.

In summary, all the previously reviewed methods acquire different levels of capability in addressing the nonlinearity in PM electrical machines. However, all of them have ignored the fact that nonlinearity is a dynamical behavior occurs in both the time and frequency domains. None has considered both the fundamental temporal and spectral qualities inherent of a nonlinear PM electrical machine system and exerts control efforts accordingly. Therefore, when a PM electrical machine system is highly nonlinear, these approaches cannot capture the true dynamics of the system, thus preventing them from generating suitable control forces to stabilize the system in both the time and frequency domains.

1.2 Research Objectives

The objective of the dissertation is to formulate proper control schemes that explore the nonlinear time-frequency control (NTFC) concept first proposed by Liu and Suh in 2012 [37] so as to (1) address the aforementioned issues with the contemporary control theory and (2) improve PM electrical machines' performance. The core principles of the nonlinear time-frequency control concept are, first, it advocates elimination of linearizing the system model. Second, it stresses the importance of identifying the time and frequency information carried by the dynamic states of the system simultaneously. Last and most importantly, it requires generating control effort based on both the time and frequency responses of the system. With the key elements of NTFC incorporated, the final

control scheme is able to identify the true dynamics of the PM electrical machine system and negate its nonlinear behaviors in both the time and frequency domains simultaneously.

To meet the stated objectives, the following research tasks are proposed:

1. Develop a viable nonlinear time-frequency control scheme for the control of PM brushed DC motors.
2. Demonstrate the feasibility of the designed control scheme through numerical studies using a PM brushed DC motor model of high nonlinearity.
3. Develop a viable nonlinear time-frequency control scheme for the control of PM synchronous motors.
4. Demonstrate the feasibility of the designed control scheme through both simulation and physical testing using a PM synchronous motor model of high nonlinearity.
5. Develop a viable nonlinear time-frequency control scheme for the chaos suppression of PM synchronous motors.
6. Validate the effectiveness and superiority of the designed control scheme through a series of simulations using a chaotic PM synchronous motor model.

2. NONLINEAR TIME-FREQUENCY CONTROL CONCEPT

2.1 Introduction

As mentioned previously, nonlinearity is a dynamic behavior that manifests in both the time and frequency domains. When perturbed, not only the trajectory of the nonlinear system would drastically change in time, its frequency components would deteriorate as well. However, modern control theories formulated to control PM electrical machines only focus on minimizing error in the time-domain. Therefore, they are not able to contain the frequency spectrum of the system response [38].

To address this issue, a nonlinear time-frequency control concept was proposed by Liu and Suh [37] in 2012. The concept was initially intended for the chaos control of non-stationary, non-autonomous systems and was shown to be effective through a series of simulations [39]. The major advantage is its ability in applying control effort based on both the temporal and spectral qualities inherent of a given dynamic system, thus making it suitable for complicated nonlinear systems. To be specific, as linearization serves to change the genuine underlying features of a system, on-line identification is incorporated to eliminate the need for adopting linearization to facilitate the generation of control force. Recognizing that nonlinearity occurs in both the time and frequency domains, discrete wavelet transformation (DWT) is selected as the vehicle of choice to simultaneously identify the temporal and spectral information carried by the dynamic states of the system. Lastly, since feedback serves to perturb a nonlinear system, the concept of adaptive feedforward control is used to generate control force based on both the time and frequency

responses of the system. A reasonable in-depth review of all the basic ideas featured in NTFC is provided as follows.

2.2 Active Noise Control

The idea of nonlinear time-frequency control is largely inspired by the concept of active noise control [40]. As the name indicates, active noise control (ANC) is initially proposed to address acoustic noise in industrial equipment such as engines, motors, pumps, and fans, to name only a few. Before active noise control was invented, passive control were the main approach for attenuating acoustic noise in real-world applications [41]. This technique is based on the principle that emitted acoustic noise can be trapped through using massive, impervious layers and the retained sound energy can be dissipated through using porous sound-absorbing lining. The effectiveness of this method depends on the ratio of the noise frequency to the thickness of the layers. The lower the noise frequency is, the thicker the layers must be. Generally speaking, passive control works well for medium and high frequency noise problems. However, for problems involving low frequency noise, applying passive control requires adding heavy and bulky acoustical enclosures. This is oftentimes impractical. In addition, due to the need for wiring, heat dissipation, or air intake, among others, most enclosed industrial equipment must have openings and the noise, low frequency noise in particular, would leak through these openings.

To address the aforementioned flaws of passive control, active noise control emerges [42]. This method employs the principle of destructive interference, which is illustrated in Figure 2.1.

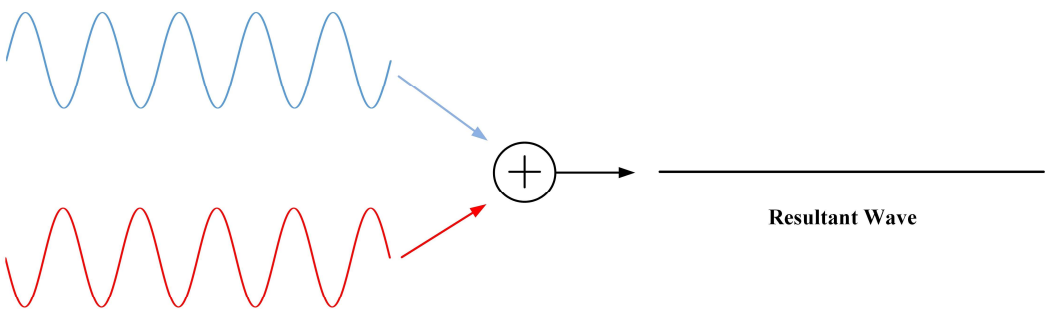

Figure 2.1 Illustration of destructive interference

In Figure 2.1, the frequency and peak amplitude of the blue and red waves are exactly the same. However, at each time instant, their amplitudes have the opposite sign. If the two waves are added together, a flat line of zero amplitude is obtained. In other words, the two waves cancel each other out. This is called destructive interference.

In ANC [43], sensors are used to measure the incoming noise, controllers and actuators are used to generate the cancelling noise that is opposite in phase with the incoming noise. Figure 2.2 illustrates a typical ANC system for noise cancellation in a simple duct.

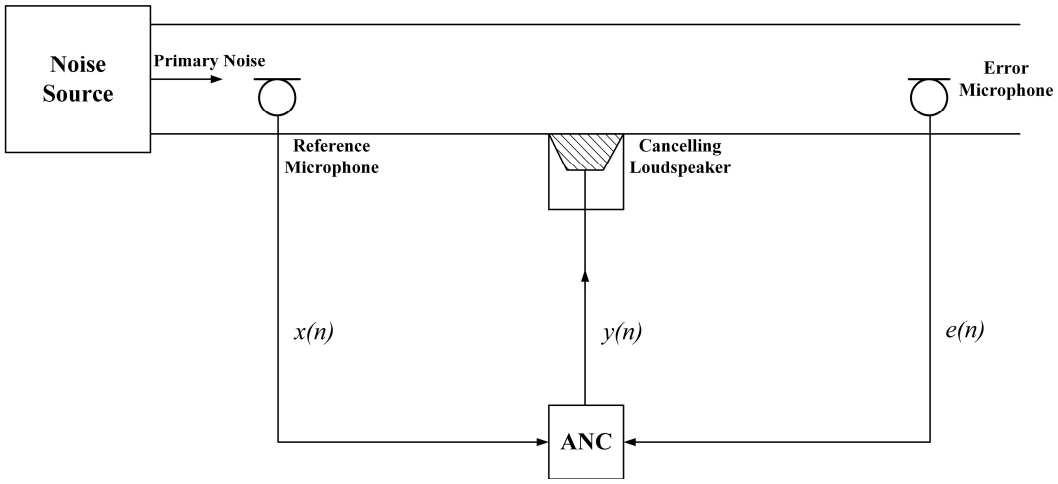

Figure 2.2 Illustration of ANC system in a duct

In Figure 2.2, noise (primary noise) is emitted from a noise source placed at the left-most end of the duct. A reference microphone is placed close to the noise source and the reference input signal *x(n)* is measured by it. The ANC module uses this reference input signal *x(n)* to generate an anti-noise signal *y(n)* of equal amplitude but opposite in phase with *x(n)*. *y(n)* is used to drive the cancelling loudspeaker to produce the cancelling sound wave that neutralizes the incoming noise. To monitor and improve the performance, an error microphone is placed after the cancelling loudspeaker. A residual noise signal *e(n)* is then gathered by it and sent to the ANC module to optimize the generation of *y(n)* for better noise cancellation.

Figure 2.3 illustrates a block diagram representation of the demonstrated ANC system with adaptive filters being used to realize the ANC module.

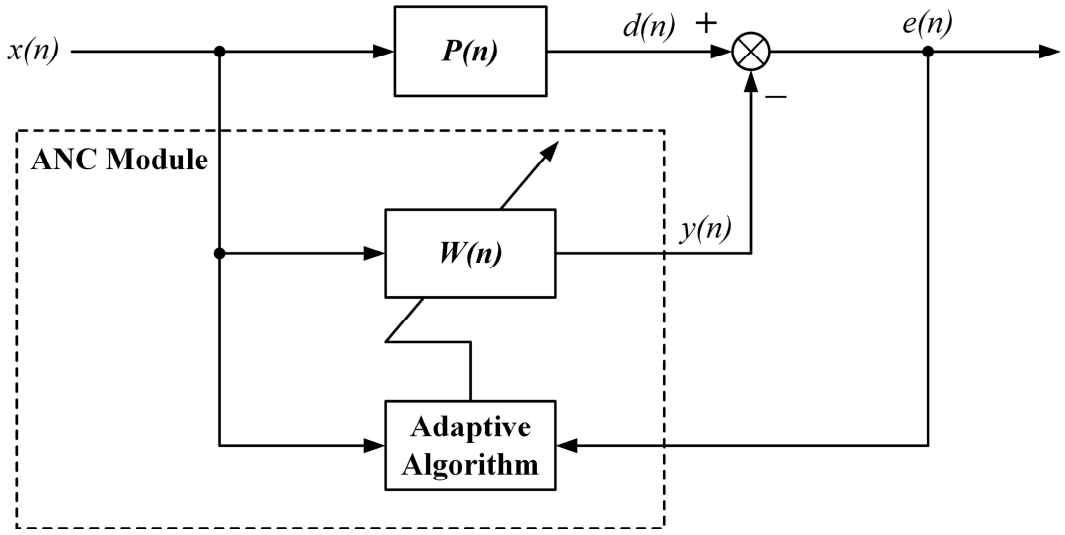

Figure 2.3 Block diagram representation of the ANC system

In Figure 2.3, ***P(n)*** stands for the mathematical model of the unknown acoustic effect from the input microphone to the error microphone. ***W(n)*** is an adaptive filter used to estimate ***P(n)***. When the adaptive algorithm adjusting the coefficients of ***W(n)*** is properly designed, ***W(n)*** would equal to ***P(n)*** after its coefficients converge. This implies that *d(n)*, the actual noise signal after the primary noise measured as *x(n)* passes through ***P(n)*** and reaches the error microphone, is identical to *y(n)*, the cancelling noise signal generated by the cancelling loudspeaker. When *d(n)* is cancelled out by *y(n)* the residual noise signal *e(n)* measured by the error microphone would be zero.

However, there is a couple of issues with the ANC system. The first challenge is related to transmission delay. In Figure 2.2, after the input reference signal *x(n)* is measured by the reference microphone and send to the ANC module, the adaptive ANC controller will need some time to generate cancelling noise *y(n)*. If this delay is longer

than the time the primary noise takes to travel from the reference microphone to the cancelling loudspeaker, the performance of the ANC system would be seriously degraded. The second challenge is the limitation of acoustical techniques. The performance of a well designed ANC system is largely determined by the cancelling loudspeaker's ability in faithfully imitating the cancelling signal $y(n)$ generated by the ANC controller. However, due to the technical limitation of acoustical equipment, it is extremely difficult for the cancelling loudspeaker to generate high frequency acoustic waves. Therefore, ANC is mainly applied to address low frequency noise. Lastly, there is a serious issue with the so-called secondary path effect.

Figure 2.4 demonstrates an illustration of the primary path and secondary path in an ANC system. The primary path is the $\boldsymbol{P(n)}$ defined in Figure 2.3. It consists of all the acoustic response from the reference microphone to the error microphone. As for the secondary path, it is defined as the path between the ANC module output $y(n)$ and the residual error $e(n)$ measured by the error microphone.

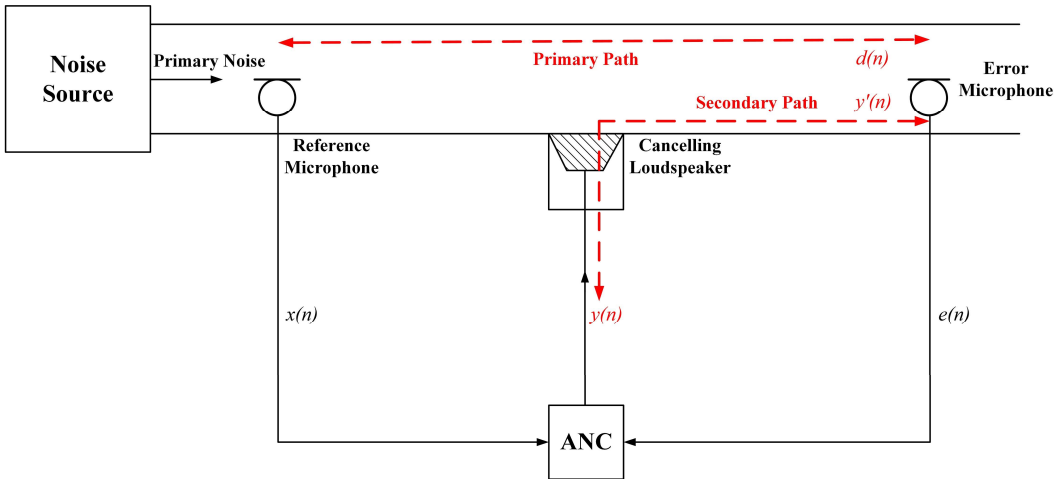

Figure 2.4 Illustration of primary path and secondary path

In the ANC system shown in Figure 2.2 and Figure 2.3, the primary noise reaches the error microphone and is measured as $x(n)$. It then transmits along the primary path modeled as $\boldsymbol{P(n)}$ and changes into $d(n)$ after it reaches the error microphone. It is initially believed that what the error microphone captures is the difference between $d(n)$ and the cancelling signal $y(n)$ generated by the ANC controller. However, in reality, $y(n)$ varies to a large extent before it reaches the error microphone. The presence of propagation medium, analog-to-digital or digital-to-analog converters, amplifiers, and filters in the path of $y(n)$ would cause it to vary significantly. This change of $y(n)$ is the secondary path effect and is illustrated in Figure 2.4, where $y(n)$ has changed into $y'(n)$ after it reaches the error microphone. Figure 2.5 shows a block diagram of the ANC system where the secondary path effect has been taken under consideration and the corresponding effect is modeled as $\boldsymbol{S(n)}$. Note that $y'(n)$ is the actual cancelling signal collected by the error microphone.

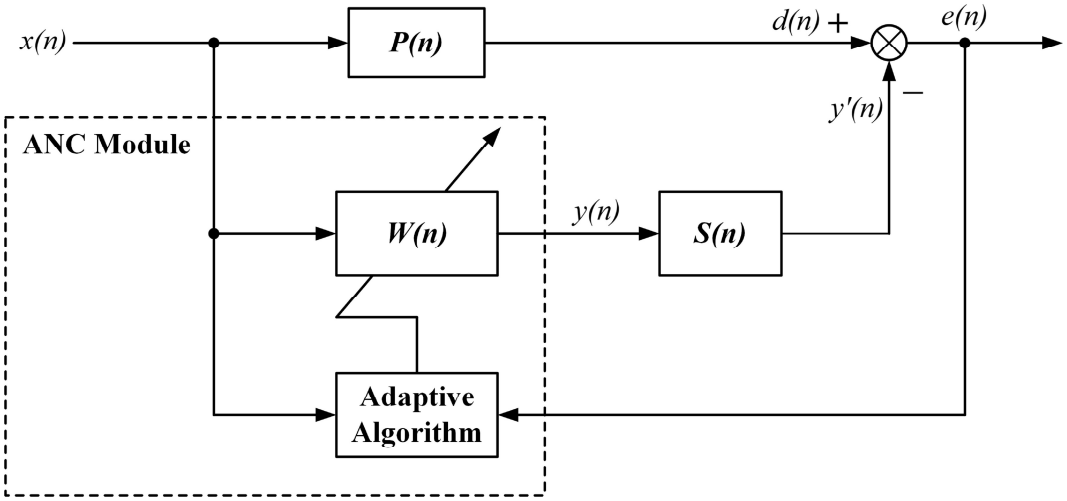

Figure 2.5 Block diagram of ANC system with secondary path effect considered

To compensate the secondary path effect and improve the performance of the ANC system, a revised ANC system is given in Figure 2.6.

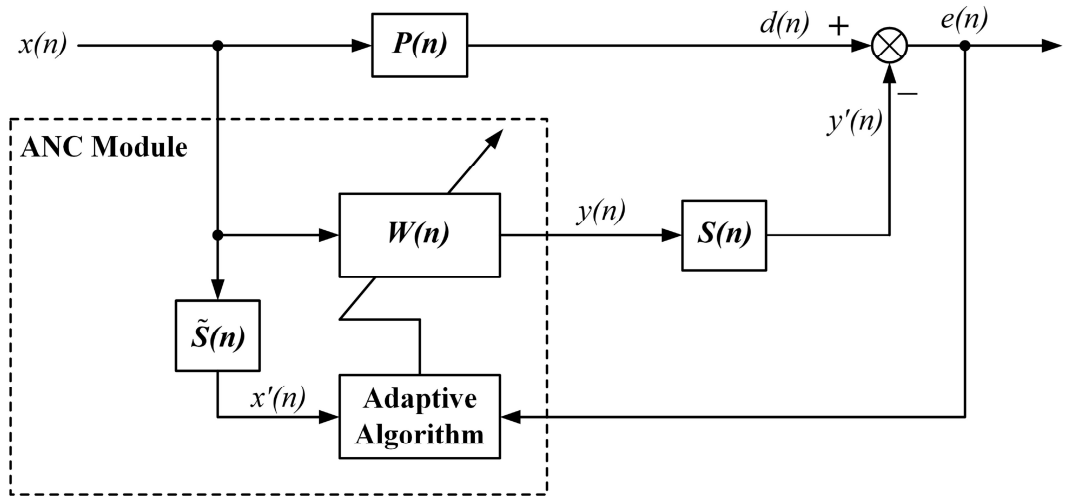

Figure 2.6 Block diagram of the revised ANC system

In the figure an extra filter $\tilde{S}(n)$, which is identical to $S(n)$, is placed between the input reference signal $x(n)$ and the weight update algorithm of the adaptive filter $W(n)$ for the sake of ensuring the convergence of the ANC module. Therefore, the adaptive algorithm uses $x'(n)$ instead of $x(n)$ to update the coefficients of $W(n)$. In practice, the modeled secondary path effect, $S(n)$, is usually unknown and oftentimes time-varying due to the aging of the cancelling loudspeaker, changes in temperature, or air flow in the transmission path, to name a few. Therefore, to guarantee the precise estimation of $\tilde{S}(n)$, on-line identification of $S(n)$ is usually adopted.

The merits of the ANC system in Figure 2.6 is that it uses feedforward adaptive control to generate the required cancelling noise, which not only avoids perturbation resulted from feedback, but facilitates the integration of time and frequency information into the control algorithm as well. Additionally, since it adopts on-line identification, the need for linearization is eliminated. When properly modified, such a framework ideal for realizing nonlinear time-frequency control.

2.3 Discrete Wavelet Transformation

Time-frequency control, as the name indicates, is a method for controlling a system in both the time and frequency domains. To do so, there must be a signal processing tool that can provide the time and frequency information of the target system simultaneously. There are many signal processing tools available such as fast Fourier transform [44], short time Fourier transform [45], and discrete wavelet transform [46]. Fast Fourier transform is a mature algorithm. It has the advantages of being simple to implement and fast to

calculate. However, even though it is able to resolve the frequency components existed in a signal, it is not capable of telling when these frequency components appear. Therefore, it is only applicable to stationary signals. Although it is able to extract time and frequency information from a signal, the time-frequency window in short time Fourier transform has a fixed temporal width that renders uniform resolution in the frequency domain. For highly nonlinear systems where frequency spectra are broad in bandwidth and time-varying, short time Fourier transform falls short in providing the resolution needed.

In nonlinear time-frequency control concept, discrete wavelet transformation is selected as the vehicle of choice for providing time and frequency information of the target system. The attractive features of it are its capabilities in extracting time and frequency information from a target signal and in providing adaptive resolution in both the time and frequency domains.

Discrete wavelet transformation is basically a multiresolution analysis [47]. It analyzes a given signal at different scales with varying resolution. Figure 2.7 illustrates how DWT works.

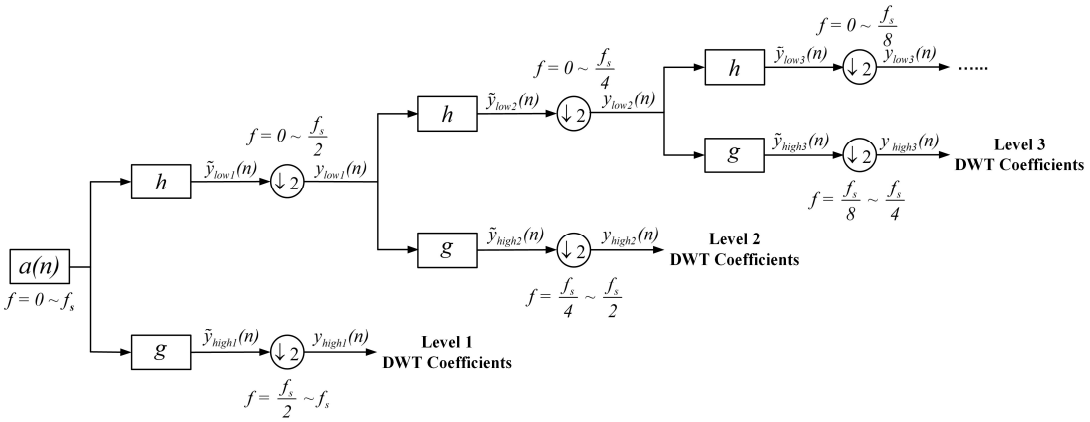

Figure 2.7 Illustration of discrete wavelet transformation

In Figure 2.7, a discrete signal $a(n)$ containing N samples and frequency components ranging from $0 \sim f_s$ is first passed through a half-band low-pass filter h and a half-band high-pass filter g simultaneously. Two new signals, $\tilde{y}_{low1}(n)$ and $\tilde{y}_{high1}(n)$, which corresponds to $a(n)$ passing through h and g, respectively, are then obtained. Since $\tilde{y}_{low1}(n)$ results from $a(n)$ passing through h, it has the same number of samples as $a(n)$, but all the frequency components that are above $f_s / 2$ in $a(n)$ are removed in $\tilde{y}_{low1}(n)$. Similarly, $\tilde{y}_{high1}(n)$ is a discrete signal of N samples but only contains the frequency components ranging from $f_s / 2 \sim f_s$ in $a(n)$. This "filter" operation has doubled the frequency resolution in the two obtained signals. Compared with the frequency band in $a(n)$, the range of the frequency components existed in either $\tilde{y}_{low1}(n)$ or $\tilde{y}_{high1}(n)$ is halved.

To acquire the first level DWT coefficients, the next step is eliminating half of the samples existed in $\tilde{y}_{low1}(n)$ and $\tilde{y}_{high1}(n)$. This is called down-sampling by 2 (realized by dropping every other samples in the signal) and is denoted as $\downarrow 2$ in Figure 2.7. The reason for this operation is due to the Nyquist Sampling Theorem, which states that the minimum sampling frequency required to present a discrete signal is two times the highest frequency existed in that signal. Since the frequency band in $\tilde{y}_{low1}(n)$ and $\tilde{y}_{high1}(n)$ are halved comparing with that in $a(n)$, only $N / 2$ samples are needed now to represent $\tilde{y}_{low1}(n)$ and $\tilde{y}_{high1}(n)$ without losing any frequency information. However, it is noted that although $\tilde{y}_{low1}(n)$ and $\tilde{y}_{high1}(n)$ now only use $N / 2$ samples to represent $\tilde{y}_{low1}(n)$ and $\tilde{y}_{high1}(n)$ after the down-sampling operation, the time resolution of the two signals, however, is halved.

In summary, to acquire the first level DWT coefficients, the original signal $a(n)$ has to first go through a filter operation, which decomposes $a(n)$ into a low frequency band signal ($\tilde{y}_{low1}(n)$) and a high frequency band signal ($\tilde{y}_{high1}(n)$). This process has doubled the frequency resolution since the frequency band in the low frequency band signal and high frequency band signal now only spans half of the frequency band in $a(n)$. After the filter operation, half of the samples in the low frequency band signal ($\tilde{y}_{low1}(n)$) and high frequency band signal ($\tilde{y}_{high1}(n)$) can be eliminated without losing any frequency information stored in the two signals. This is called subsampling by 2 and it has halved the time resolution of the two signals as only half of the samples are now used to represent

the entire signal. Equation (2.1) illustrates a mathematical representation of the first level DWT decomposition.

$$y_{low1}(n) = \sum_{k=-\infty}^{\infty} a(k)h(2n - k)$$
$$y_{high1}(n) = \sum_{k=-\infty}^{\infty} a(k)g(2n - k) \quad (2.1)$$

where $\tilde{y}_{low1}(n)$ and $\tilde{y}_{high1}(n)$, referred to as coarse coefficients and detail coefficients, are the outputs from the low-pass filter h and high-pass filter g after the subsampling by 2 operation.

To obtain further levels of decomposition, the above operation is repeated by passing the outputs from the low-pass filter h after the subsampling by 2 operation through the same low-pass and high-pass filters (Figure 2.7). This process can keep continuing until only 2 samples are left. The DWT of $a(n)$ is then obtained by concatenating all levels of DWT coefficients starting from the last level of decomposition and the DWT of $a(n)$ will have the same length as $a(n)$.

In addition to providing joint time and frequency information with adaptive resolutions, DWT also possesses the benefit of data size reduction. Frequency components that are not dominant in $a(n)$ would appear as low amplitude DWT coefficients and can be neglected without seriously distorting the signal.

Despite the aforementioned benefits, DWT, however, has its limitations. Even though frequency components existed in $a(n)$ are all manifested in its DWT, each frequency component has its own time-domain resolution determined by which level of DWT coefficients it appears on. Specifically, for high frequency components, DWT

provides a precise time-domain resolution because the majority of DWT coefficients are used to represent them. However, for low frequency components, the time-domain resolution is not satisfactory, because only a few number of DWT coefficients are used to describe them. That is to say, DWT offers excellent time resolution at high frequency band and good frequency resolution at low frequency band. If a given signal is not suitable to analyze using DWT, other signal processing tools would need be selected.

2.4 Nonlinear Time-Frequency Control Scheme

After a proper signal processing tool has been selected, the next essential element to realize nonlinear time-frequency control is to design a proper control scheme that is able to generate proper control effort based on both the time and frequency information gathered from the target system. This is achieved by modifying the ANC framework illustrated in Figure 2.6 and integrating DWT into it.

In an ANC framework, an adjustable adaptive filter uses the measured noise signal as the reference to generate an anti-noise signal which has exactly the same amplitude as the noise signal but of an opposite phase. The residual error is then acquired and sent to the weight updating adaptive algorithm of the adaptive filter to adjust its coefficients so as to minimize the residual error. In addition, to compensate the secondary path effect, an extra adaptive filter which models the secondary path effect is placed in the path of the reference input signal to the weight updating adaptive algorithm.

Following this idea, a DWT-based nonlinear time-frequency control scheme with parallel on-line modeling technique is devised in Figure 2.8.

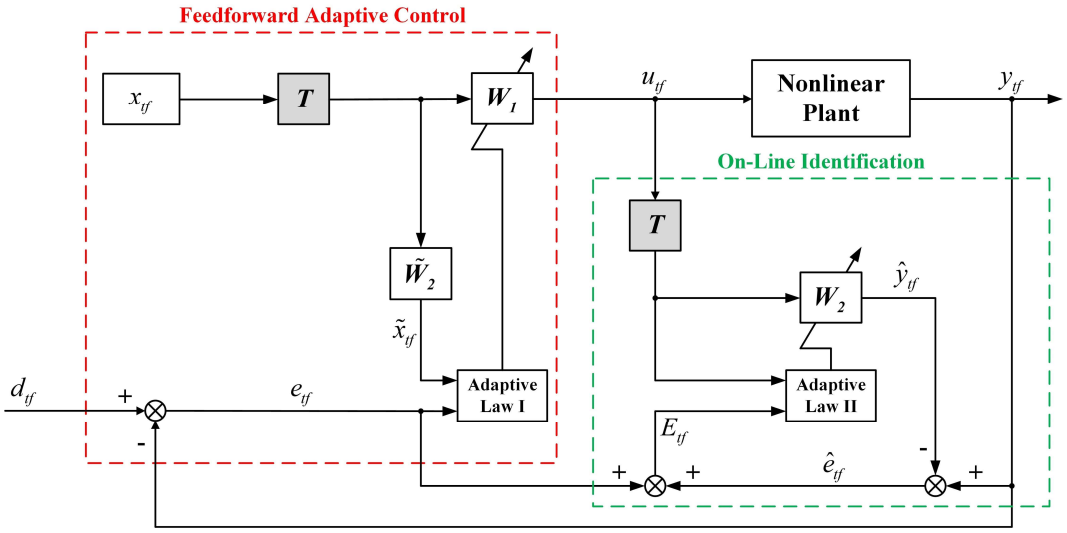

Figure 2.8 Illustration of nonlinear time-frequency control scheme

In Figure 2.8, $\boldsymbol{T}$ represents an N by N discrete wavelet transformation matrix used to extract the time and frequency information from its input signal; $\boldsymbol{W}_1$ is an adaptive filter acting as the main controller for feed-forward control; $\boldsymbol{W}_2$ represents another adaptive filter for on-line identification; $\tilde{\boldsymbol{W}}_2$ is the mirror image of $\boldsymbol{W}_2$.

It is seen that the presented nonlinear time-frequency control scheme consists of two major modules - one for feedforward adaptive control and one for on-line identification. Differing from contemporary PM electrical machine control methods, this nonlinear control scheme is able to mitigate nonlinearity in both the time and frequency domains simultaneously. Rooted in the notion that the time and frequency information of a signal can be extracted using proper signal processing tools, discrete wavelet transformation is selected to extract the time and frequency information of the system response simultaneously. As feedback serves to perturb a system, the notion of feed-

forward adaptive control ($\boldsymbol{W_1}$) is used to manipulate the coarse and detail coefficients obtained from DWT [48]. Lastly, an adaptive filter ($\boldsymbol{W_2}$) is adopted for on-line identification of the nonlinear plant.

Specifically, the adjustable adaptive controller $\boldsymbol{W_1}$ takes the residual error, e_{tf}, which is the difference between the desired nonlinear plant output d_{tf} and the actual nonlinear plant output y_{tf}, to generate the control effort u_{tf} through manipulating a specifically designed input signal x_{tf} following the Adaptive Law I. Meanwhile, the adaptive on-line identification filter, $\boldsymbol{W_2}$, takes the generated control effort u_{tf} and the total error E_{tf}, which is the sum of the residual error e_{tf} and the identification error $\hat{e}_{tf}$ (difference between y_{tf} and the estimated $\hat{y}_{tf}$), to update its coefficients following the Adaptive Law II. During the process, DWT is employed to process signals x_{tf} and u_{tf} before they transmitted to the adaptive filters [49].

The mathematical representations [50-54] of the above control algorithm is summarized in the followings. With n being the current time-step and N the vector length, the equation that governs the main feed-forward controller $\boldsymbol{W_1}$ used to calculate the control effort $u_{tf}(n)$ is

$$u_{tf}(n) = \boldsymbol{W_1^T(n)TX_{tf}(n)} \tag{2.2}$$

where $\boldsymbol{W_1(n)}$ represents the weight vector of $\boldsymbol{W_1}$ of the following form

$$\boldsymbol{W_1(n)} = [w_{1,1}(n),\ w_{1,2}(n),\ \cdots,\ w_{1,N}(n)]^T \tag{2.3}$$

$$\boldsymbol{T} = \begin{bmatrix} T_{11} & T_{12} & \cdots & T_{1N} \\ T_{21} & T_{22} & \cdots & T_{2N} \\ \vdots & \vdots & \ddots & \vdots \\ T_{N1} & T_{N2} & \cdots & T_{NN} \end{bmatrix} \tag{2.4}$$

is the selected N by N DWT matrix, and

$$\boldsymbol{X_{tf}(n)} = [x_{tf}(n),\ x_{tf}(n-1),\ \cdots,\ x_{tf}(n-N+1)]^T \tag{2.5}$$

is the signal vector of the specifically designed input signal. The coefficients of $\boldsymbol{W_1(n)}$ is updated using the adaptive law

$$\boldsymbol{W_1(n+1)} = \boldsymbol{W_1(n)} + \mu_{tf1}(n)\boldsymbol{T}\tilde{\boldsymbol{X}}_{\boldsymbol{tf}}\boldsymbol{(n)}e_{tf}(n) \tag{2.6}$$

where $\mu_{tf1}(n)$ is the optimization step size.

$$e_{tf}(n) = d_{tf}(n) - y_{tf}(n) \tag{2.7}$$

is the residual error, and

$$\tilde{\boldsymbol{X}}_{\boldsymbol{tf}}\boldsymbol{(n)} = [\tilde{x}_{tf}(n),\ \tilde{x}_{tf}(n-1),\ \cdots,\ \tilde{x}_{tf}(n-N+1)]^T \tag{2.8}$$

is the compensated signal vector formed by passing $\boldsymbol{X_{tf}(n)}$ through $\tilde{\boldsymbol{W}}_{\boldsymbol{2}}\boldsymbol{(n)}$, which is identical to the weights of the on-line identification filter

$$\boldsymbol{W_2(n)} = [w_{2,1}(n),\ w_{2,2}(n),\ \cdots,\ w_{2,N}(n)]^T \tag{2.9}$$

This process can be mathematically represented as

$$\tilde{x}_{tf}(n) = \boldsymbol{W_2^T(n)TX_{tf}(n)} \tag{2.10}$$

The coefficients of the on-line identification filter $\boldsymbol{W_2(n)}$ is updated using the adaptive law

$$\boldsymbol{W_2(n+1)} = \boldsymbol{W_2(n)} + \mu_{tf2}(n)\boldsymbol{TU_{tf}(n)}E_{tf}(n) \tag{2.11}$$

where $\mu_{tf2}(n)$ is another optimization step size.

$$\boldsymbol{U_{tf}(n)} = [u_{tf}(n), u_{tf}(n-1), \cdots, u_{tf}(n-N+1)]^T \tag{2.12}$$

is the control effort vector;

$$E_{tf}(n) = e_{tf}(n) + \hat{e}_{tf}(n) \tag{2.13}$$

is the summation of the residual error $e_{tf}(n)$ and the estimation error $\hat{e}_{tf}(n)$ defined as

$$e_{tf}(n) = y_{tf}(n) - \hat{y}_{tf}(n) \tag{2.14}$$

where

$$\hat{y}_{tf}(n) = \boldsymbol{W_2^T(n) T U_{tf}(n)} \tag{2.15}$$

is the estimated nonlinear plant output calculated by passing the control effort vector $\boldsymbol{U_{tf}(n)}$ through the adaptive on-line identification filter $\boldsymbol{W_2(n)}$.

2.5 Summary

As stated earlier, nonlinearity is a dynamic deterioration occurs in both the time and frequency domains. In highly nonlinear PM electrical machine systems, not only the amplitude of the dynamic state drastically changes in the time domain, its frequency components aggravates as well. However, all the reviewed contemporary control methods for PM electrical machines only focus on regulating its nonlinearity in the time domain, while neglecting the significance of restraining its frequency components from deteriorating in the frequency domain. Most control approaches reviewed earlier require the linearization of the PM electrical machine system in order to facilitate controller design. This would inevitably alter the underlying dynamics of the PM electrical machine system and hence degrade the performance of the designed controller. Therefore, a control method

that not only is able to identify the true dynamics of the PM electrical machine system in both the time and frequency domains without using linearization, but also is capable of generating proper control effort based on the identified information.

Following the idea, a nonlinear time-frequency control scheme is developed. It is basically an integration of adaptive active noise control theory and discrete wavelet transformation. Rooted in the fact that simultaneous time-frequency control of a signal can be achieved through manipulating its detail and coarse coefficients that together explicitly carry all the inherent time and frequency information pertaining to the signal, adaptive control and discrete wavelet transformation is combined to generate proper control effort based on the temporal and spectrum information extracted from the signal. As feedback serves to perturb a nonlinear system, the notion of feed-forward adaptive control is employed. Lastly, on-line identification using adaptive filters is incorporated to eliminate the need of linearization and to compensate the effect of parameter variation.

3. NONLINEAR TIME-FREQUENCY CONTROL OF PM BRUSHED DC MOTORS

3.1 Introduction

PM brushed DC motors have seen extensive applications since their debut around 60 years ago [55, 56]. Unlike AC motors and brushless DC motors, which use complicated electronic mechanisms for current control, PM brushed DC motors adopt a mechanical structure to regulate the current. In PM brushed DC motors, a wound armature is attached to the rotor shaft in the center with stator permanent magnets rather than field windings surrounding it. As the rotor turns, brushes on the stator would successively come into contact with the commutators mounted to different rotor windings and pass the supply current to the armature coil. This distinguished feature renders PM brushed DC motor many advantages such as simple in structure, compact in size, low in power loss, fast in response, and linear in performance curve [10, 55]. However, they also bring potential problems [2, 57]. The frequent interaction between the brush and commutator would cause the two components to wear out over time, thus demanding periodic maintenance. In addition, vibrations induced by this brush/commutator junction also restrict the performance of PM brushed DC motors at high speed. As a result, their popularity declines. However, as stated in section 1.1, PM brushed DC motors possess unique benefits over their main competitors including AC motors and brushless DC motors, thus continuing to be a favorable choice for industrial applications.

Contemporary research on PM brushed DC motor control mainly focuses on formulating speed and position control schemes that are effective, efficient, and accurate under external disturbances. Even though PM brushed DC motor is almost a linear system due to the elimination of the nonlinear field flux versus armature current magnetization characteristics, it would still demonstrate strong nonlinearity when afflicted by disturbances such as noise. Techniques applied to mitigate this undesirable behavior include PID control, fuzzy logic control, model reference adaptive control, and adaptive PID control, to name only a few. However, all these approaches share a common issue. While the notion "nonlinearity" represents a dynamical behavior occurs in both the time and frequency domains, none of the mentioned methods consider the fundamental temporal and spectral qualities inherent of PM brushed DC motors and exert control effort accordingly.

In the sections that follows, a nonlinear time-frequency control scheme specifically designed for the speed and position control of PM brushed DC motor is discussed. Simulation results show that the designed controller is feasible for alleviating the nonlinear behavior of the PM brushed DC motor that hampers the tracking of speed and position with desired precision. The nonlinear time-frequency control scheme demonstrates a significantly better capability in resolving the nonlinear state of the PM brushed DC motor system with excellent precision and robustness. In addition, the proposed control scheme also significantly improves the waveform of the armature voltage/current, thus greatly enhancing the energy efficiency of the system. Moreover, with a simple proportional

controller, the incompatibility of precision concurrent speed and position control is resolved using the same basic control configuration.

3.2 PM Brushed DC Motor Model

There are many different types of brushed DC motors available in the market. Depending on the way the stator magnetic field is generated, they can be roughly classified into five different types: PM brushed DC motors, shunt-wound brushed DC motors, series-wound brushed DC motors, compound-wound brushed DC motors, and separately excited brushed DC motors. Each type has its own pros and cons and is suitable for certain range of applications.

Among them, PM brushed DC motor is a special one. Unlike other four types of brushed DC motors where field windings are used to generate the stator magnetic field, PM brushed DC motor uses permanent magnets as the source of stator magnetic field. This has eliminated the armature reaction effect and brings PM brushed DC motors many advantages as stated earlier. In addition, due to the availability of high-intensity permanent magnets, large-scale PM brushed DC motors become increasingly popular. Therefore, PM brushed DC motors are an ideal choice for applications where high control precision is required.

Figure 3.1 gives the schematic of the equivalent circuit of a PM brushed DC motor, which illustrates the electrical and mechanical power conversion inside the motor system. An input voltage source $V_{a_{PMDC}}$ is applied to the coil of the rotor armature, which is modeled as a resistance $R_{a_{PMDC}}$ in series with an inductance $L_{a_{PMDC}}$ and an induced voltage $e_{a_{PMDC}}$. The induced voltage $e_{a_{PMDC}}$ is generated by the rotation of the armature coil through

the fixed flux lines of the stator magnets. This voltage opposes the applied armature voltage $V_{a_{PMDC}}$ and is often referred to as back-emf.

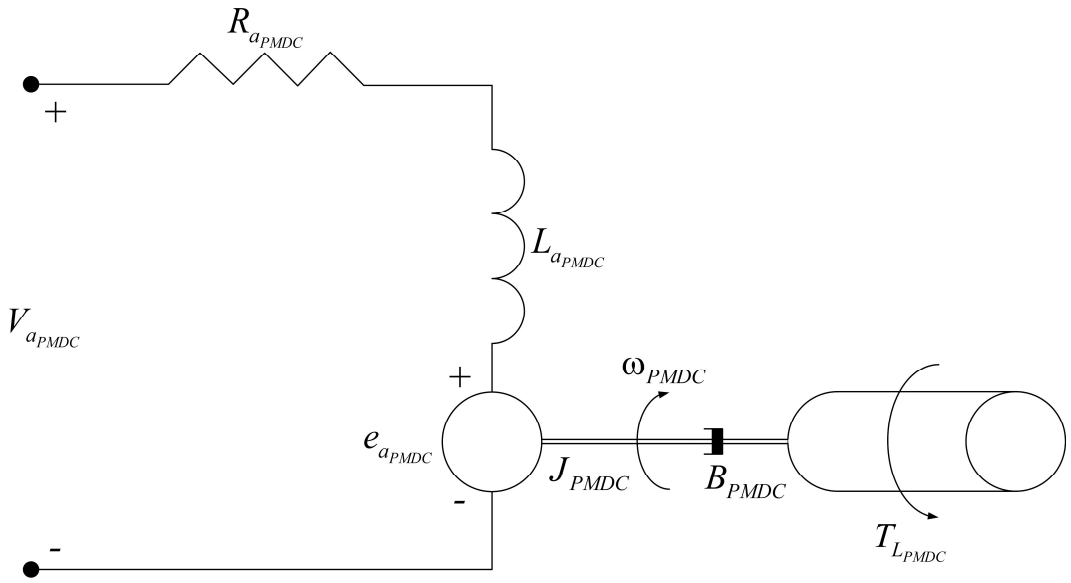

Figure 3.1 Equivalent circuit of a PM brushed DC motor

The applied armature voltage $V_{a_{PMDC}}$ overcomes the back-emf $e_{a_{PMDC}}$ together with the voltage drop across the armature resistance $R_{a_{PMDC}}$ and armature inductance $L_{a_{PMDC}}$, and induces the armature current $i_{a_{PMDC}}$ to flow. Applying the Kirchoff's voltage law, which states that the summation of all the electrical voltages around a loop is zero, to the electrical side, the following equation is obtained

$$V_{a_{PMDC}} - V_{R_{a_{PMDC}}} - V_{L_{a_{PMDC}}} - e_{a_{PMDC}} = 0 \tag{3.1}$$

According to the Ohm's law, the voltage drop across the resistor is

$$V_{R_{a_{PMDC}}} = R_{a_{PMDC}} i_{a_{PMDC}} \tag{3.2}$$

The voltage drop across the inductance is proportional to the rate of change of the armature current as

$$V_{L_{a_{PMDC}}} = L_{a_{PMDC}} \frac{di_{a_{PMDC}}}{dt} \tag{3.3}$$

The back-emf $e_{a_{PMDC}}$ is calculated using

$$e_{a_{PMDC}} = K_{E_{PMDC}} \omega_{PMDC} \tag{3.4}$$

where $K_{E_{PMDC}}$ is the voltage constant of the motor and ω_{PMDC} is the angular velocity of the rotor as follows

$$\omega_{PMDC} = \frac{d\theta_{PMDC}}{dt} \tag{3.5}$$

with θ_{PMDC} being the angular displacement of the rotor.

On the mechanical side, according to the law of conservation of angular momentum, the summation of the torques on the rotor should equal to zero, thus

$$T_{e_{PMDC}} - T_{\omega_{PMDC}} - T_{B_{PMDC}} - T_{L_{PMDC}} = 0 \tag{3.6}$$

where $T_{e_{PMDC}}$ is the electromagnetic torque, $T_{\omega_{PMDC}}$ is the toque caused by the acceleration of the rotor, $T_{B_{PMDC}}$ is the torque due to the viscous damping, and $T_{L_{PMDC}}$ is the external torque load. Their corresponding mathematical expressions are

$$\begin{cases} T_{e_{PMDC}} = K_{T_{PMDC}} i_{a_{PMDC}} \\ T_{\omega_{PMDC}} = J_{PMDC} \dfrac{d\omega_{PMDC}}{dt} \\ T_{B_{PMDC}} = B_{PMDC} \omega_{PMDC} \\ T_{L_{PMDC}} = T_{L_{PMDC}} \end{cases} \tag{3.7}$$

where $K_{T_{PMDC}}$ is the torque constant of the motor, J_{PMDC} is the moment of inertia of the motor, and B_{PMDC} is the friction coefficient of the motor.

Combining Equations (3.1) - (3.7), the final mathematical description of the PM brushed DC motor model is [55],

$$\begin{cases} L_{a_{PMDC}} \dfrac{di_{a_{PMDC}}}{dt} = -R_{a_{PMDC}} i_{a_{PMDC}} - K_{E_{PMDC}} \omega_{PMDC} + V_{a_{PMDC}} \\ J_{PMDC} \dfrac{d\omega_{PMDC}}{dt} = K_{T_{PMDC}} i_{a_{PMDC}} - B_{PMDC} \omega_{PMDC} - T_{L_{PMDC}} \\ \omega_{PMDC} = \dfrac{d\theta_{PMDC}}{dt} \end{cases} \tag{3.8}$$

Table 3.1 lists the corresponding unit of each parameter.

Table 3.1 Units of each PM brushed DC motor parameter

Parameter	Unit
armature inductance, $L_{a_{PMDC}}$	H
armature voltage, $V_{a_{PMDC}}$	V
armature current, $i_{a_{PMDC}}$	A
armature resistance, $R_{a_{PMDC}}$	ohms
induced back-emf, $e_{a_{PMDC}}$	V
moment of inertia of the motor, J_{PMDC}	kg.m^2
angular velocity of the rotor, ω_{PMDC}	rad/s
electromagnetic torque developed, $T_{e_{PMDC}}$	Nm
friction coefficient of the motor, B_{PMDC}	Nm/rad/s
external torque load, $T_{L_{PMDC}}$	Nm
voltage constant, $K_{E_{PMDC}}$	V/rad/s
torque constant, $K_{T_{PMDC}}$	Nm/A
angular displacement of the rotor, θ_{PMDC}	rad

It is noted in Equation (3.8), that the electrical and mechanical components of the DC motor are coupled. The induced back-emf $e_{a_{PMDC}}$ in the electrical equation depends on the rotor speed ω_{PMDC} ; while the generated electromagnetic torque $T_{e_{PMDC}}$ in the mechanical equation depends on the armature current $i_{a_{PMDC}}$. A PM brushed DC motor can exhibit strong nonlinearity subject to such a complexity and the presence of the external torque load $T_{L_{PMDC}}$ and disturbances - an unacceptable response in practical application as

it not only degrades motor performance but also restricts its applicability. Therefore, control of the nonlinearity in a PM brushed DC motor system is of great significance.

3.3 Nonlinear Time-Frequency Speed Control of PM Brushed DC Motors

3.3.1 Nonlinear Time-Frequency Speed Control Scheme for PM Brushed DC Motors

To make the speed tracking performance of PM brushed DC motors more stable and energy efficient than conventional control approaches, the novel nonlinear time-frequency control scheme presented in section 2 is followed to realize the speed control of PM brushed DC motors. Differing from all the previously reviewed methods in philosophy as well as control strategy, instead of simply controlling the time or frequency response of the motor, the nonlinear time-frequency speed control law developed here denies dynamic deteriorations in both the time and frequency domains simultaneously. Specifically, recognizing that nonlinearity is a dynamic behavior registered in both the time and frequency domains, DWT is selected as the vehicle of choice for providing simultaneous temporal and spectral resolutions of system states. As feedback serves to perturb a nonlinear system, the notion of feed-forward control is adopted to address the issue of vulnerability to disturbances of large temporal gradient. Lastly, an adaptive controller for on-line identification is incorporated to address non-stationarity and parameter variations.

Figure 3.2 illustrates the basic configuration of the proposed nonlinear time-frequency speed control scheme for the PM brushed DC motor model presented in Equation (3.8) with the reference rotor angular velocity ω_{NTFC}^{*} being d_{tf}, actual rotor

angular velocity ω_{NTFC} being y_{tf}, armature control voltage $V_{a_{NTFC}}$ being u_{tf}, and $T_{L_{NTFC}}$ being the external torque load.

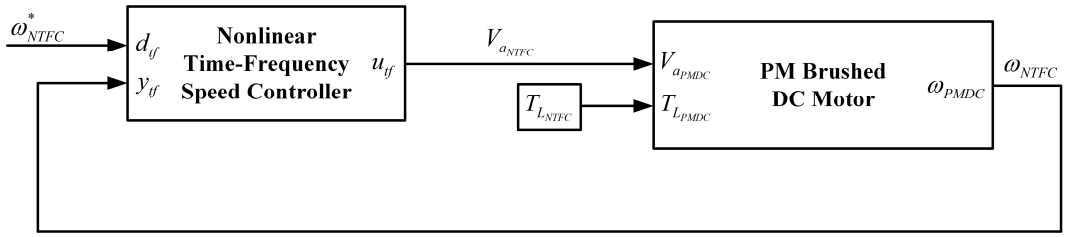

Figure 3.2 Illustration of the nonlinear time-frequency speed control scheme for PM brushed DC motors

To demonstrate the quality of the above nonlinear time-frequency speed control scheme, its performance in negating system disturbances during speed tracking is evaluated against the traditional PID speed control scheme and the popular fuzzy logic speed control scheme using a PM brushed DC motor whose specifications are tabulated in Table 3.2.

Table 3.2 PM brushed DC motor specifications

Motor parameters	Value
Motor rating	1,500W
Rated Voltage	110V
Rated Speed	3,000rpm
Rated Torque	4.8Nm
Armature resistance, $R_{a_{PMDC}}$	0.22Ω
Armature inductance, $L_{a_{PMDC}}$	0.00073H
Rotor inertia, J_{PMDC}	0.0051Kg.m^2
Voltage Constant, $K_{E_{PMDC}}$	0.3342V/rad/s

3.3.2 PID Speed Control Scheme for PM Brushed DC Motors

The PID speed control scheme employed for the speed tracking of PM brushed DC motors is illustrated in Figure 3.3.

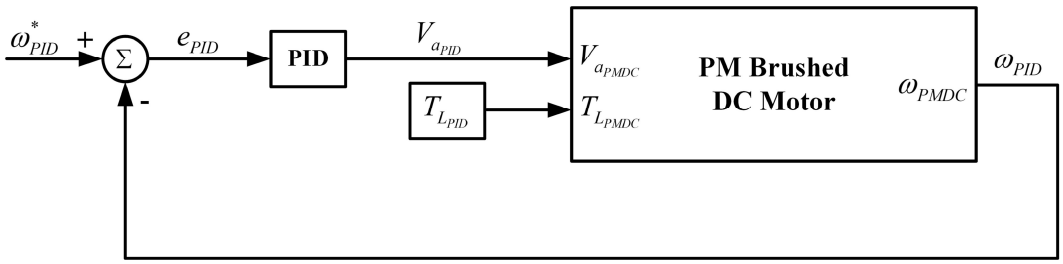

Figure 3.3 Illustration of the PID speed control scheme for PM brushed DC motors

where e_{PID} is the error between the desired rotor speed ω_{PID}^{*} and the actual rotor speed ω_{PID}; $T_{L_{PID}}$ is the external torque load; $V_{a_{PID}}$ is the control output generated by the PID controller following the algorithm below

$$V_{a_{PID}}(n) = k_p e_{PID}(n) + k_i [V_{a_{PID}}(n-1) + \frac{e_{PID}(n) + e_{PID}(n-1)}{2} T_s] + k_d \frac{e_{PID}(n) - e_{PID}(n-1)}{T_s} \tag{3.9}$$

with k_p being the proportional gain, k_i the integral gain, k_d the derivative gain, and T_s the sampling time. In order for the PID controller to function properly, parameters k_p, k_i, and k_d need to be tuned accurately. Table 3.3 presents the gain values of the PID speed controller following the Ziegler-Nichols tuning method [58].

Table 3.3 Parameters of the PID speed control scheme for PM brushed DC motors

PID Parameters	Value
k_p	0.2521
k_i	22.3931
k_d	0.0001

3.3.3 Fuzzy Logic Speed Control scheme for PM Brushed DC Motors

The fuzzy logic speed control scheme employed for the speed tracking of the target PM brushed DC motor is illustrated in Figure 3.4.

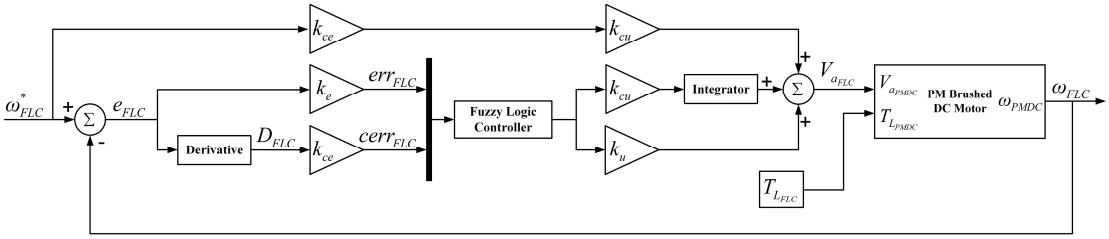

Figure 3.4 Illustration of the fuzzy logic speed control scheme for PM brushed DC motors

where e_{FLC} is the error between the reference rotor speed ω_{FLC}^* and the actual rotor speed ω_{FLC}; D_{FLC} is the derivative of e_{FLC} calculated using the present error $e_{FLC}(n)$ and the previous error $e_{FLC}(n-1)$; k_e, k_{ce}, k_u, and k_{cu} are scaling factors used to scale the corresponding input and output signals; $V_{a_{FLC}}$ is the final armature control voltage generated by the fuzzy logic speed control scheme; $T_{L_{FLC}}$ is the external torque load.

The structure of a fuzzy logic controller is very simple in concept. It commonly consists of three main components: fuzzification, inference engine, and defuzzification (Figure 3.5). The fuzzification component fuzzifies the inputs using the input membership functions. The inference engine component calculates the fuzzy output based on the fuzzified inputs and linguistic rules stored in the rule base. Finally, the defuzzification component generates the output of the fuzzy logic controller using the output membership functions.

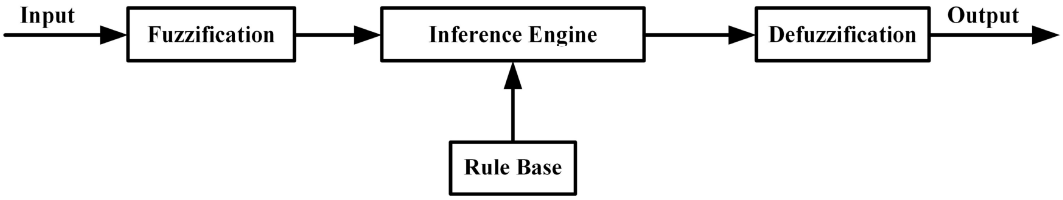

Figure 3.5 Structure of a fuzzy logic controller

In the illustrated fuzzy logic speed control scheme, err_{FLC} (obtained by passing e_{FLC} through k_e) and $cerr_{FLC}$ (obtained by passing D_{FLC} through k_{ce}) are selected as the first and second input to the fuzzy logic controller, respectively. The corresponding membership functions and fuzzy rules are indicated in Figure 3.6 - Figure 3.8 and in Table 3.4, where NL stands for negative large, NS stands for negative small, N stands for negative, Z stands for zero, P stands for Positive, PS stands for positive small, and PL stands for positive large.

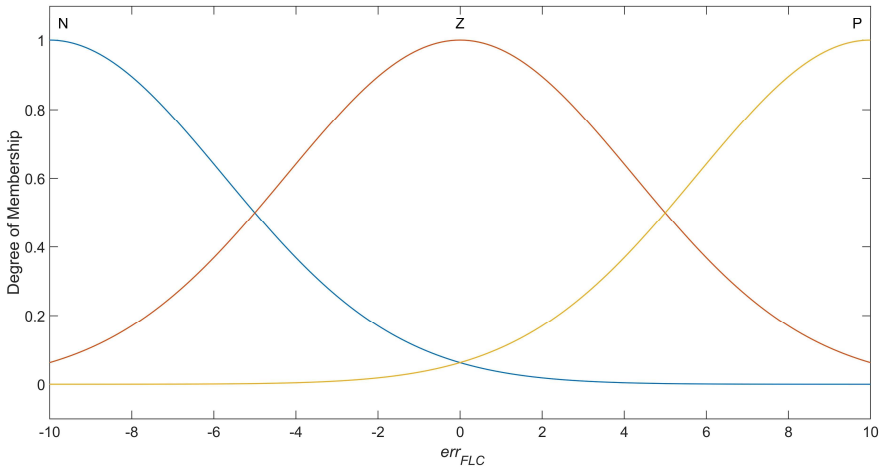

Figure 3.6 Input membership function of err_{FLC} for fuzzy logic speed control scheme

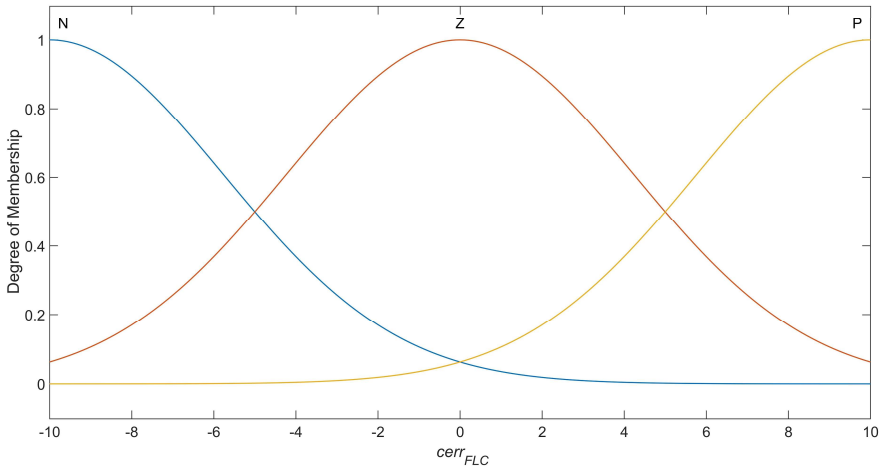

Figure 3.7 Input membership function of $cerr_{FLC}$ for fuzzy logic speed control scheme

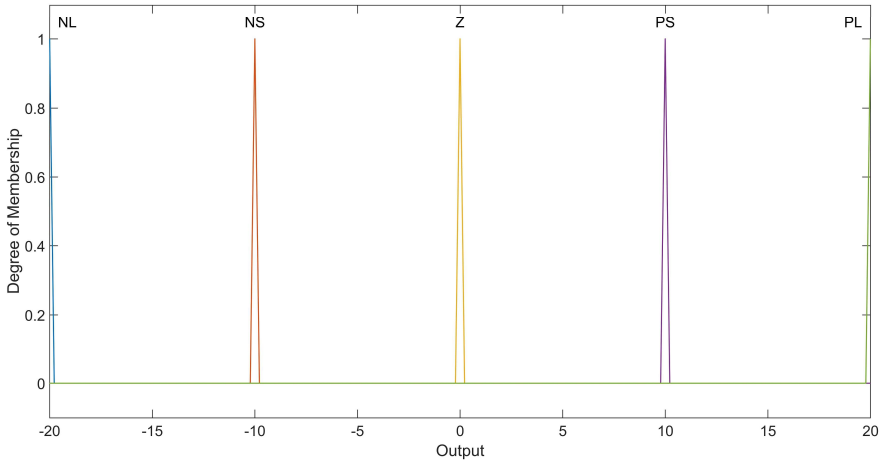

Figure 3.8 Output membership function for fuzzy logic speed control scheme

Table 3.4 Fuzzy rules for fuzzy logic speed control scheme

Rule 1	If err_{FLC} is N and $cerr_{FLC}$ is N, then Output is NL
Rule 2	If err_{FLC} is N and $cerr_{FLC}$ is Z, then Output is NS
Rule 3	If err_{FLC} is N and $cerr_{FLC}$ is P, then Output is Z
Rule 4	If err_{FLC} is Z and $cerr_{FLC}$ is N, then Output is NS
Rule 5	If err_{FLC} is Z and $cerr_{FLC}$ is Z, then Output is Z
Rule 6	If err_{FLC} is Z and $cerr_{FLC}$ is P, then Output is PS
Rule 7	If err_{FLC} is P and $cerr_{FLC}$ is N, then Output is Z
Rule 8	If err_{FLC} is P and $cerr_{FLC}$ is Z, then Output is PS
Rule 9	If err_{FLC} is P and $cerr_{FLC}$ is P, then Output is PL

It is important to note that even though the number of membership functions and fuzzy rules can be increased to improve the performance of the fuzzy logic controller, it is not sufficient to overcome the drawback of being vulnerable to the noise caused by fuzzy logic control's inherent operating mechanism. The membership functions and fuzzy rules presented herein are designed to be simple for demonstration purpose,

3.3.4 Evaluation of the Speed Tracking Performance

In this section, the nonlinear time-frequency speed control scheme for the target PM brushed DC motor is implemented in Matlab/Simulink and its performance is evaluated against the PID speed control scheme and fuzzy logic speed control scheme. The solver selected for the simulation is fixed-step (discrete) and the sampling time (T_s) is 0.00001 seconds.

To achieve a reasonable comparison, all three control schemes are tuned to have similar step response under zero torque load. Figure 3.9 - Figure 3.11 display the step response of the target PM brushed DC motor with PID speed control scheme, fuzzy logic speed control scheme, and nonlinear time-frequency speed control scheme under zero torque load, respectively. Detailed comparisons of their time-domain performance are listed in Table 3.5, where Rise Time is the time the response takes to rise from 10% to 90% of the reference value, Time to Settle is the time the response takes to reach its steady-state when the error between the actual response and reference response becomes less than 2% of the reference value, and Overshoot is the percentage ratio of the peak value of the actual response minus its reference value divided by the reference value.

Table 3.5 Speed step response comparisons of the three speed control schemes

Performance	PID	FLC	NTFC
Rise Time	0.034 s	0.029 s	0.039 s
Settling Time	0.069 s	0.073 s	0.068 s
Overshoot	0%	0%	0%

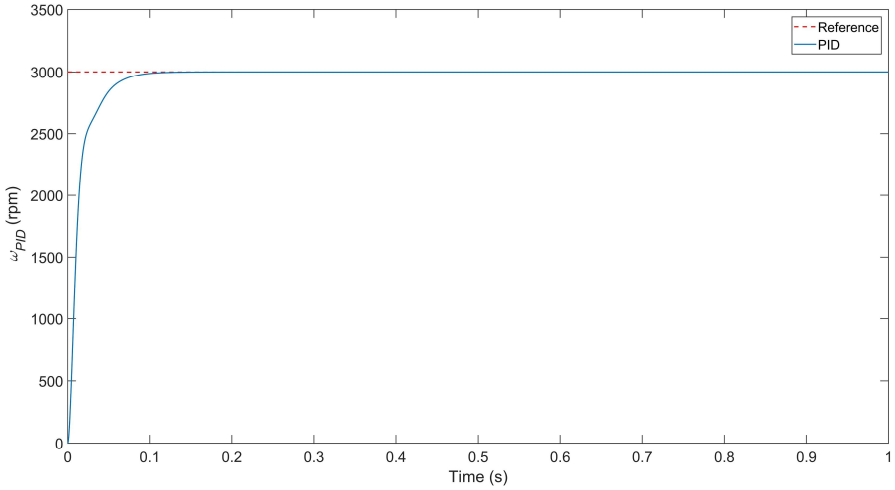

Figure 3.9 Step response of PID speed control scheme under zero torque load

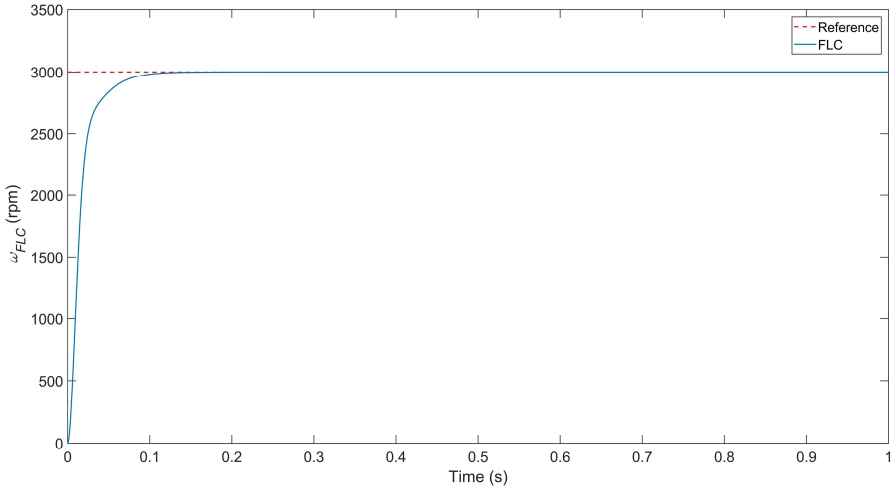

Figure 3.10 Step response of fuzzy logic speed control scheme under zero torque load

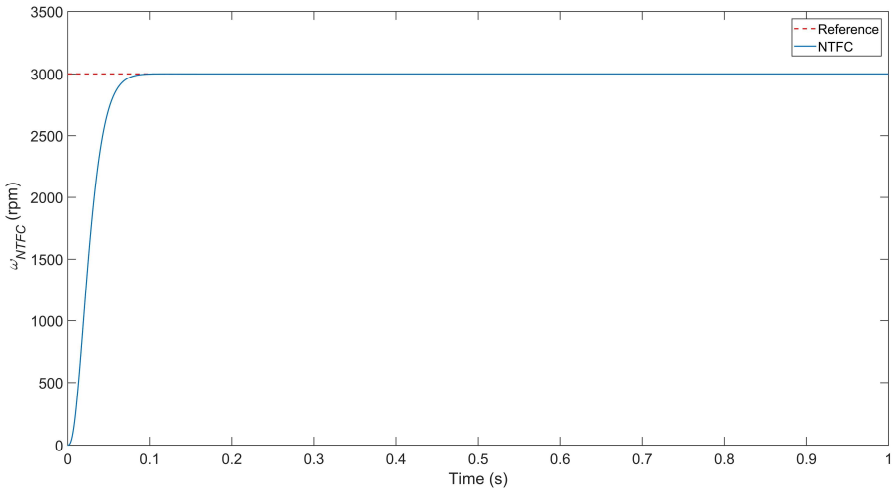

Figure 3.11 Step response of nonlinear time-frequency speed control scheme under zero torque load

Based on Figure 3.9 - Figure 3.11 and Table 3.5, it is clear that the three control schemes have very similar transient behavior when there is a step change of the reference from 0 rpm to 3,000 rpm at $t = 0$ s.

To demonstrate the superiority of the nonlinear time-frequency speed control scheme, a series of studies are performed. The first study being considered for the evaluation is described as follows:

$$Reference\ Speed = \begin{cases} 10\%\ Rated, 0.0 \le t \le 0.5 \\ 90\%\ Rated, 0.5 \le t \le 1.0 \\ 10\%\ Rated, 1.0 \le t \le 1.5 \end{cases}, \text{ and } External\ Load = Rated, 0.0 \le t \le 1.5 .$$

The motor system is operated initially at a low speed (10% rated speed) and then switched to a high speed (90% rated speed) at $t = 0.5$ second. After 0.5 second, it changes back to low speed. During the whole process, a constant external torque load with the rated

value is applied to the rotor shaft. This case is designed to test the performance of the three control schemes when reference speed suddenly changes.

Figure 3.12 - Figure 3.14 are the corresponding speed tracking responses of PID speed control scheme, fuzzy logic speed control scheme, and nonlinear time-frequency speed control scheme, respectively. Detailed comparisons of their time-domain performances are listed in Table 3.6.

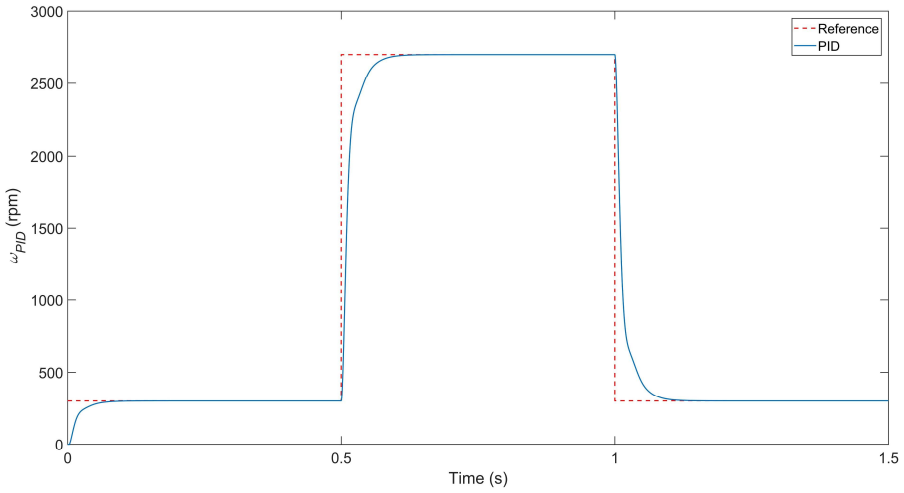

Figure 3.12 Speed tracking response of PID speed control scheme when reference speed suddenly changes

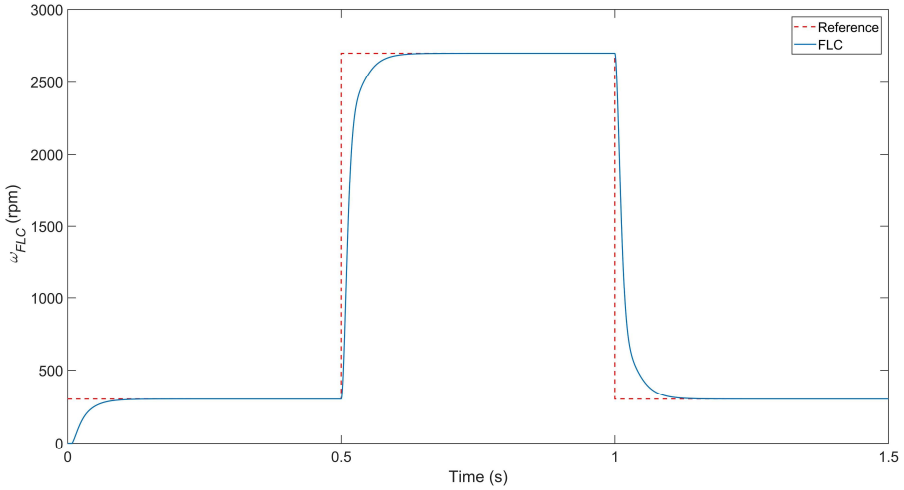

Figure 3.13 Speed tracking response of fuzzy logic speed control scheme when reference speed suddenly changes

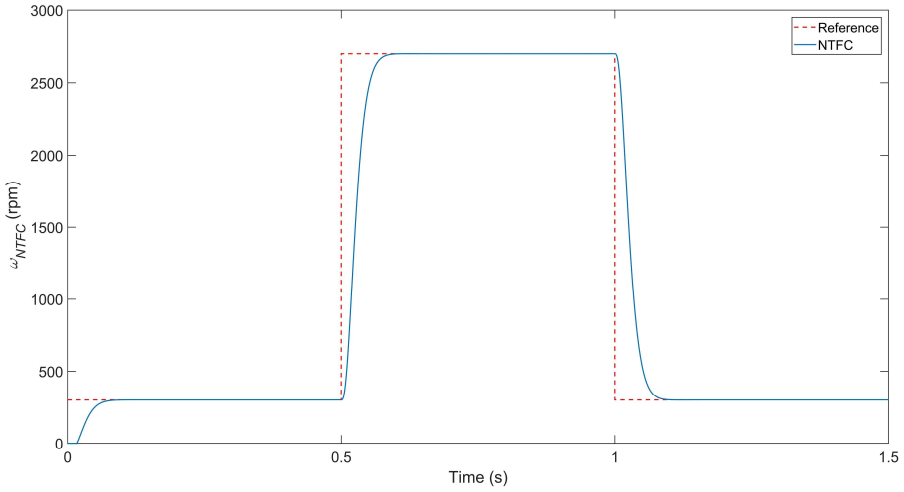

Figure 3.14 Speed tracking response of nonlinear time-frequency speed control scheme when reference speed suddenly changes

Table 3.6 Comparisons of time-domain performance of the three control schemes when reference speed suddenly changes

Time (sec)	Rise Time (sec)			Time to Settle (sec)			Overshoot (%)		
	PID	FLC	NTFC	PID	FLC	NTFC	PID	FLC	NTFC
0.00 - 0.50	0.039	0.049	0.036	0.076	0.098	0.074	0	0	0
0.50 - 1.00	0.034	0.032	0.039	0.069	0.075	0.068	0	0	0
1.00 - 1.50	0.034	0.032	0.039	0.069	0.075	0.068	0	0	0

It is seen from Figure 3.12 - Figure 3.14 and Table 3.6 that all three speed control schemes demonstrate similar performance when the reference speed suddenly changes. They are all shown to be accurate, fast, and robust.

Figure 3.15 - Figure 3.17 illustrate the armature control voltage generated by the three control schemes considered. Clearly, the armature voltage profile of fuzzy logic speed controller and nonlinear time-frequency speed controller are much smoother than the PID speed controller. The corresponding armature current induced in the PM brushed DC motor are displayed in Figure 3.18 - Figure 3.20.

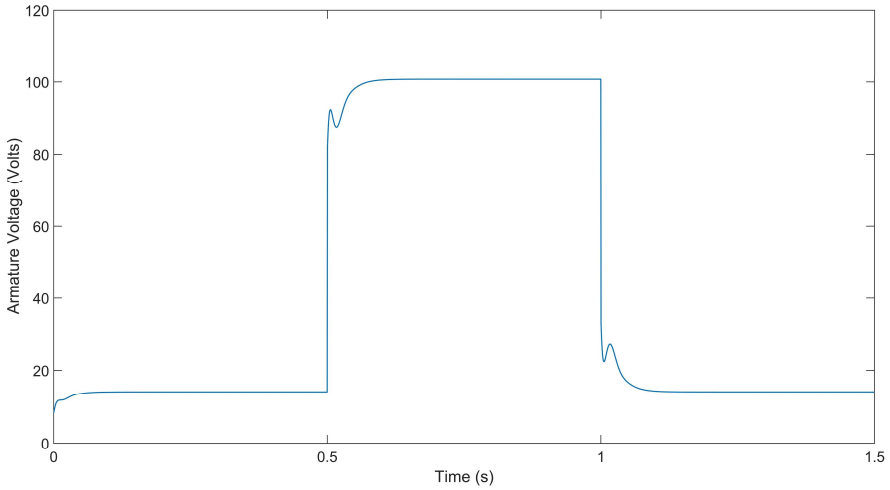

Figure 3.15 Armature control voltage generated by PID speed control scheme when reference speed suddenly changes

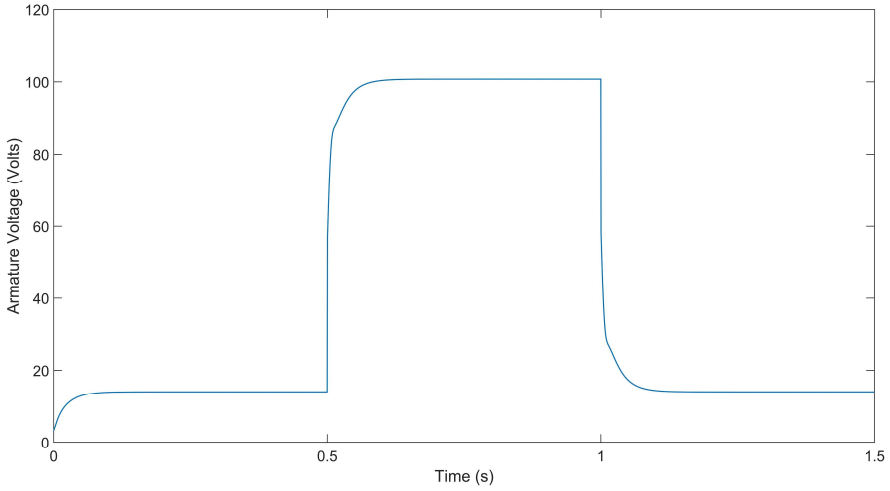

Figure 3.16 Armature control voltage generated by fuzzy logic speed control scheme when reference speed suddenly changes

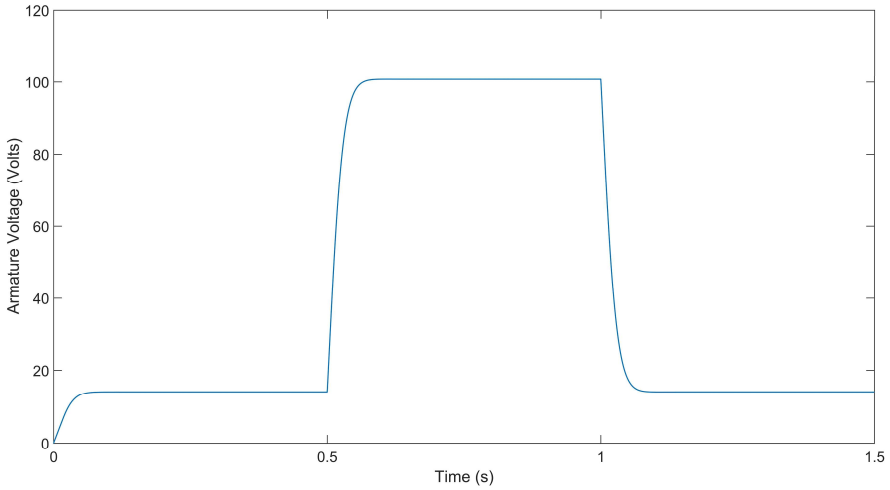

Figure 3.17 Armature control voltage generated by nonlinear time-frequency speed control scheme when reference speed suddenly changes

According to Figure 3.18 - Figure 3.20, the armature current profile of PID speed control scheme, fuzzy logic speed control scheme, and nonlinear time-frequency speed control scheme all experience overshoot when reference speed suddenly changes. Of the three, the motor with PID speed controller has the largest current overshoot (approximately 250 ampere when the reference speed changes from 10% rated speed to 90% rated speed or vice versa). Such large current overshoots are detrimental in practice as it would damage the entire system. In contrast, the motor with nonlinear time-frequency speed control scheme has the smallest current overshoot (only about 110 ampere when the reference speed changes from 10% rated speed to 90% rated speed or vice versa) and hence is preferred in practical applications.

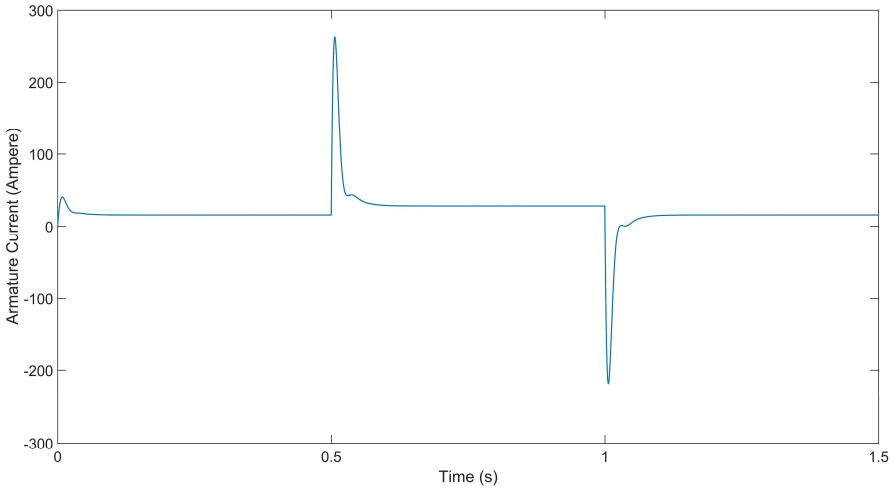

Figure 3.18 Armature current of PID speed control scheme when reference speed suddenly changes

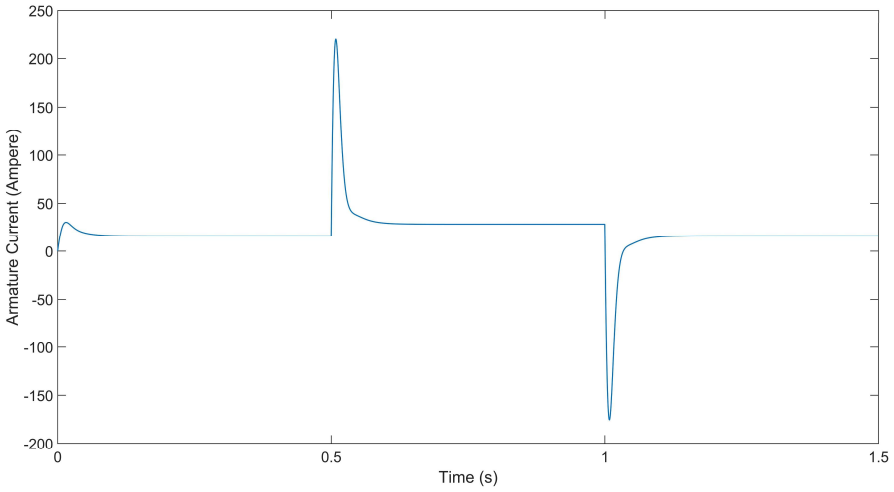

Figure 3.19 Armature current of fuzzy logic speed control scheme when reference speed suddenly changes

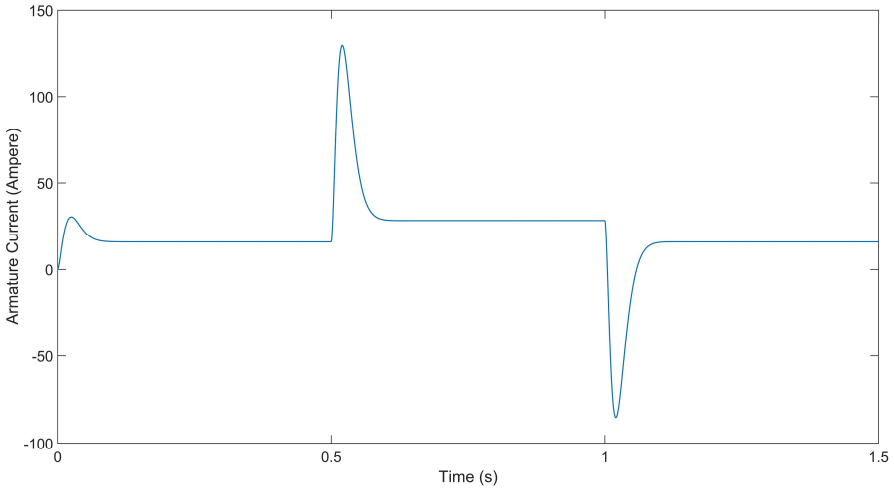

Figure 3.20 Armature current of nonlinear time-frequency speed control scheme when reference speed suddenly changes

Equation (3.10) gives the formula used to calculate the average input power, P_{inavg} , of the motor system.

$$P_{inavg} = \frac{1}{T_s}\frac{1}{M}\sum_{n=1}^{M}\left[\left|V_{a_{PMDC}}[n]\right|\left|i_{a_{PMDC}}[n]\right|T_s\right] \tag{3.10}$$

where M is the total number of discrete samples in the given time period.

Table 3.7 tabulates the corresponding P_{inavg} associated with each of the control scheme. Obviously, when all demonstrate similar speed response, the motor with nonlinear time-frequency speed control scheme is the most energy cost effective one.

Table 3.7 Average input power of the motor system with three speed control schemes when reference speed suddenly changes

Time (sec)	P_{inavg} (KW)		
	PID	FLC	NTFC
0.00 - 1.50	1.350	1.342	1.309

To further evaluate the robustness of the nonlinear time-frequency speed control scheme when reference speed abruptly changes, the impact of sensor noise that is omnipresent in daily control practices is considered next. An external broadband noise S_{PMDC} depicted in Figure 3.21 is introduced to the motor system via $Measured\ Motor\ Speed = \omega_{PMDC}(n) + S_{PMDC}(n)$. Figure 3.22 - Figure 3.24 display the corresponding speed responses of the PID speed control scheme, fuzzy logic speed control scheme, and nonlinear time-frequency speed control scheme, respectively. It is seen that the speed responses of PID speed control scheme and nonlinear time-frequency speed control scheme seem unaffected and are similar to their speed responses in Figure 3.12 and Figure 3.14 where sensor noise was neglected. The speed response of fuzzy logic speed control scheme deteriorates a little bit.

Table 3.8 lists detailed comparisons of the time-domain speed tracking performances of the three control schemes subject to the same sensor noise. Comparing with Table 3.6, it can be seen that the motor with nonlinear time-frequency speed control scheme is the most robust to sensor noise. Not only its rise time and time-to-settle keep the same as in Table 3.6, but it has the smallest increase in overshoot of all the three

schemes when the sensor noise in injected into the system. While the performance of PID speed control scheme is satisfactory, nevertheless, the disadvantage is that it has a slightly larger overshoot than the nonlinear time-frequency speed control scheme. As for the fuzzy logic speed control scheme, since it's time-to-settle increases by a large amount when the reference speed changes from 10% rated to 90% rated with the largest overshoots, it is the most vulnerable to sensor noise of the three control schemes.

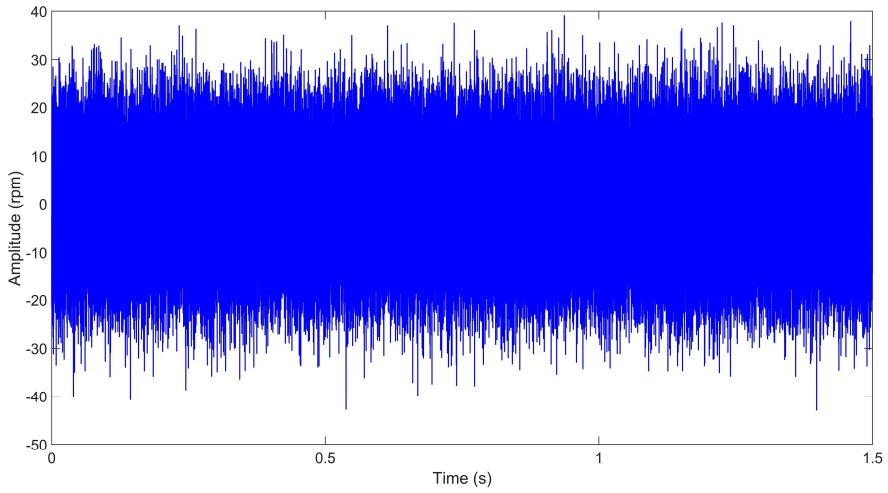

Figure 3.21 Gaussian white noise $S_{PMDC}(n)$

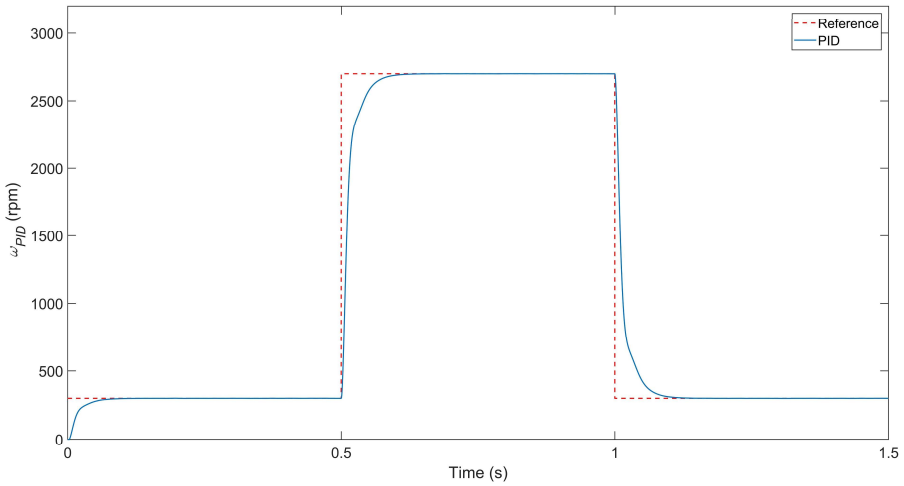

Figure 3.22 Speed tracking response of PID speed control scheme when reference speed suddenly changes and sensor noise is introduced

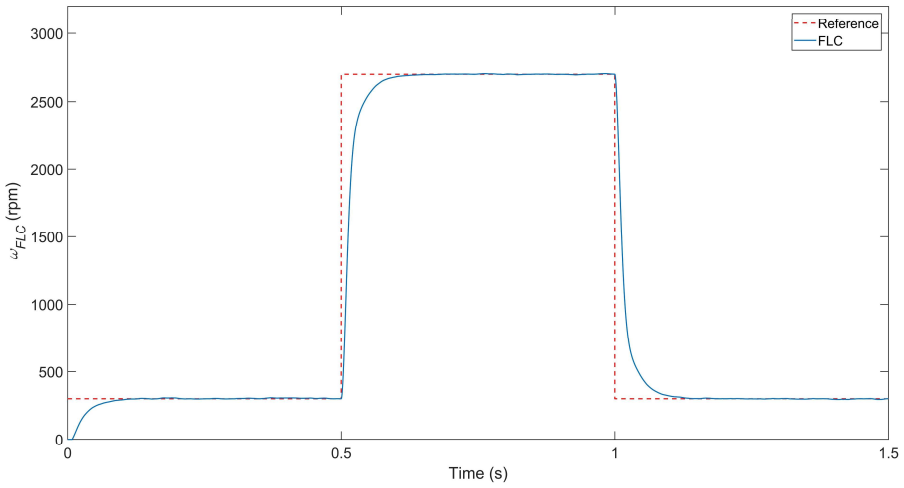

Figure 3.23 Speed tracking response of fuzzy logic speed control scheme when reference speed suddenly changes and sensor noise is introduced

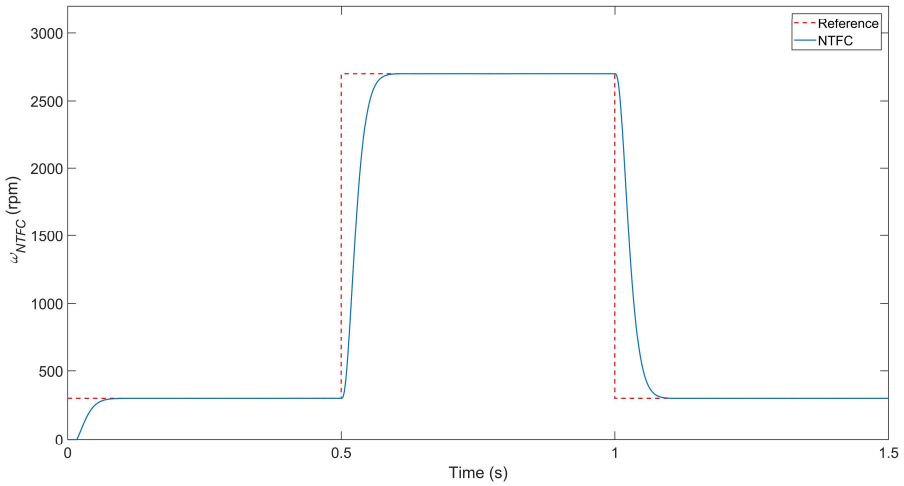

Figure 3.24 Speed tracking response of nonlinear time-frequency speed control scheme when reference speed suddenly changes and sensor noise is introduced

Table 3.8 Comparisons of time-domain performance of the three control schemes when reference speed suddenly changes and sensor noise is introduced

Time (sec)	Rise Time (sec)			Time to Settle (sec)			Overshoot (%)		
	PID	FLC	NTFC	PID	FLC	NTFC	PID	FLC	NTFC
0.00 - 0.50	0.039	0.055	0.036	0.077	0.414	0.075	0.175	2.459	0.121
0.50 - 1.00	0.034	0.033	0.039	0.069	0.076	0.068	0.012	0.170	0.008
1.00 - 1.50	0.034	0.034	0.039	0.069	0.078	0.068	0.000	0.000	0.000

Figure 3.25 - Figure 3.27 display the corresponding armature control voltages generated by the three control schemes in response to the imposed sensor noise. It is evident that the performance of the nonlinear time-frequency speed control scheme is unmatched by both the PID speed control and fuzzy logic speed control whose controlled voltage profiles are laden with apparent high frequency oscillations. Such unstable voltage

profile would place a huge burden on the associated power electronic devices and hence should be avoided in practice. Compared with PID speed control, the armature control voltage generated by the fuzzy logic speed control scheme is seen to be severely deteriorated. This is due to the fact that the output of the fuzzy logic controller extremely relies on the exact values of its inputs. When subjected to noise, information pertaining to the exact system state that is carried by the error input (err_{FLC}) is seriously distorted. This is fine as long as the controlled state is far away from its desired value. However, when the system reaches the reference point, the large error introduced would cause the fuzzy logic controller to constantly switching between different membership functions, thus inducing severe chattering in the output terminal. The situation is even worse for the change-of-error input ($cerr_{FLC}$) since the true state of the motor system is inexorably skewed. In other words, the more a fuzzy logic controller depends on $cerr_{FLC}$ to compute the appropriate controller output, the more susceptible it is to the negative effect of noise.

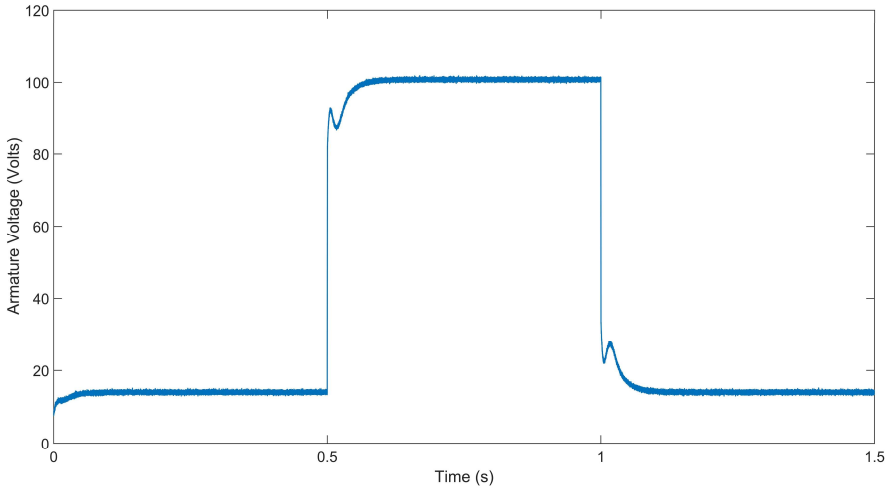

Figure 3.25 Armature control voltage generated by PID speed control scheme when reference speed suddenly changes and sensor noise is introduced

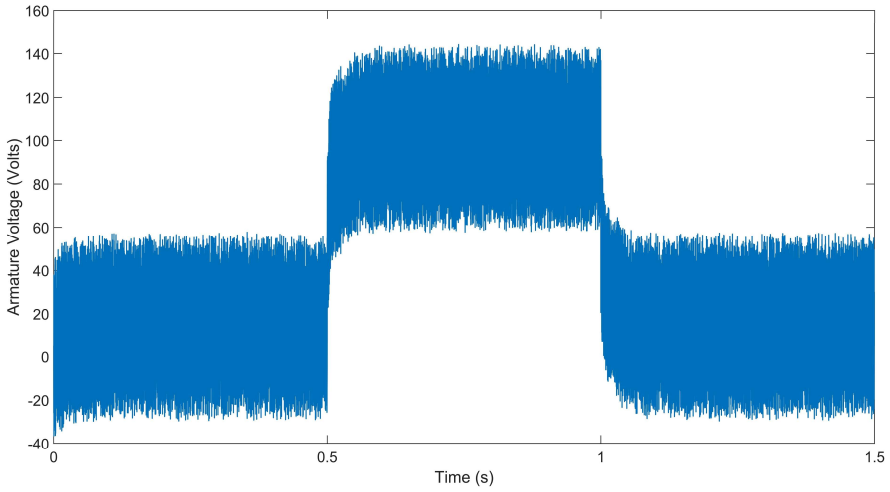

Figure 3.26 Armature control voltage generated by fuzzy logic speed control scheme when reference speed suddenly changes and sensor noise is introduced

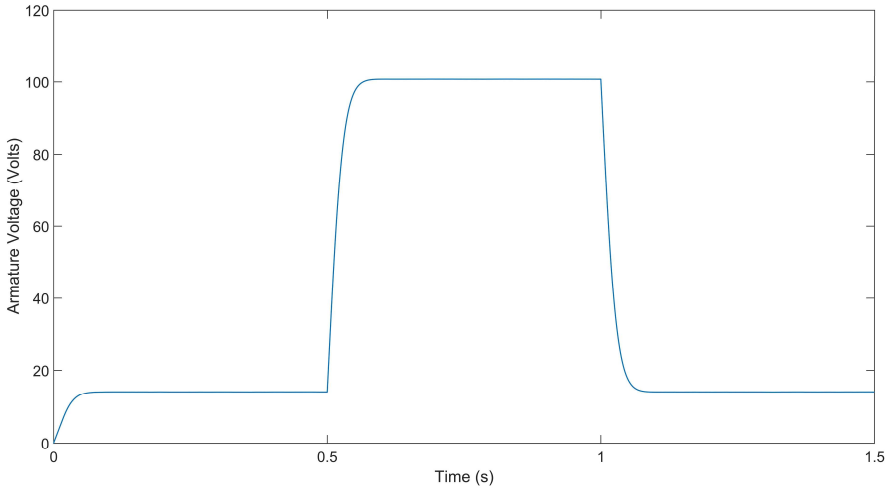

Figure 3.27 Armature control voltage generated by nonlinear time-frequency speed control scheme when reference speed suddenly changes and sensor noise is introduced

Figure 3.28 - Figure 3.30 present the armature currents induced in the PM brushed DC motor. Clearly, fuzzy logic speed control scheme has the worst armature current profile among the three where oscillations are registered. Similar to Figure 3.18 and Figure 3.20 where sensor noise was not considered, the armature current profile of the PID speed control scheme and nonlinear time-frequency speed control scheme seem unaffected. However, based on Figure 3.31 - Figure 3.33, where the frequency spectra of the motor armature current of the PID speed control, fuzzy logic speed control, and nonlinear time-frequency control are displayed, the motor under the nonlinear time-frequency speed control obviously has a much better frequency domain armature current performance than the PID speed control. Specifically, most frequency components appeared in the armature current of the PID scheme due to the introduction of noise are suppressed in the nonlinear time-frequency speed control scheme. In other words, even though PID speed control

scheme seems to function well in the time-domain when the broad band external disturbance is introduced (Table 3.8), it fails to perform well in the frequency-domain. Nonlinear time-frequency control scheme, on the other hand, is able to control the motor's response in both the time and frequency domains.

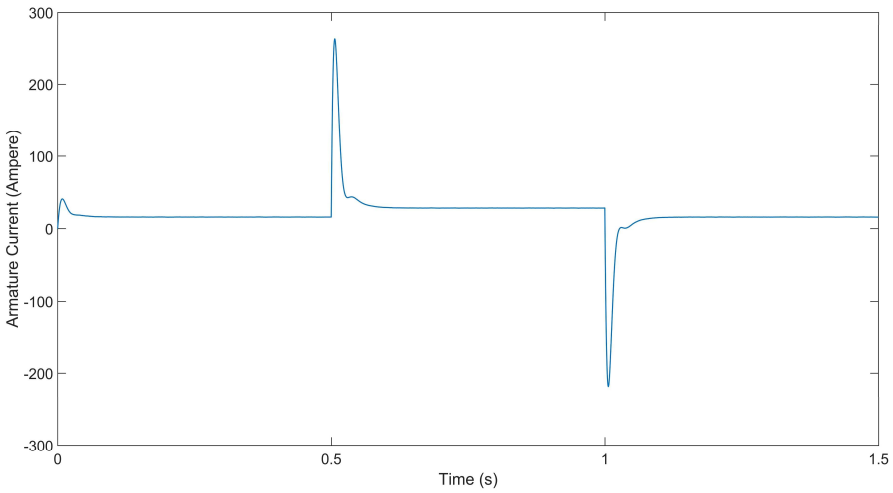

Figure 3.28 Armature current of PID speed control scheme when reference speed suddenly changes and sensor noise is introduced

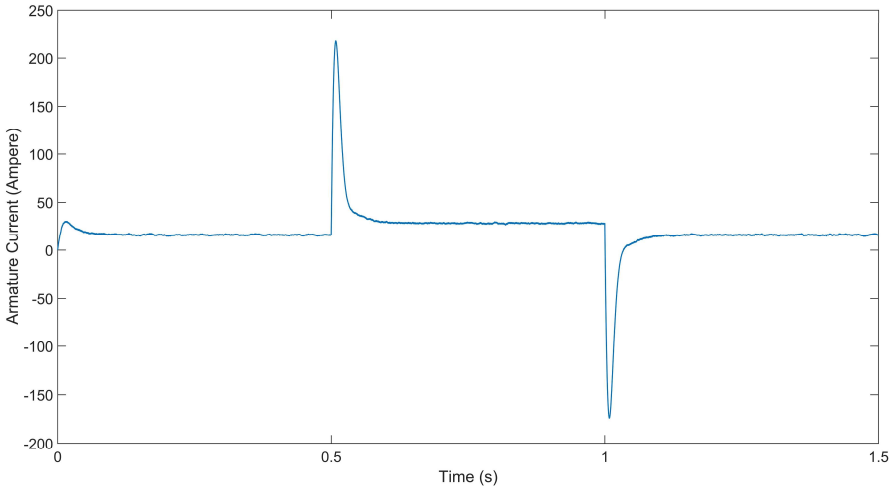

Figure 3.29 Armature current of fuzzy logic speed control scheme when reference speed suddenly changes and sensor noise is introduced

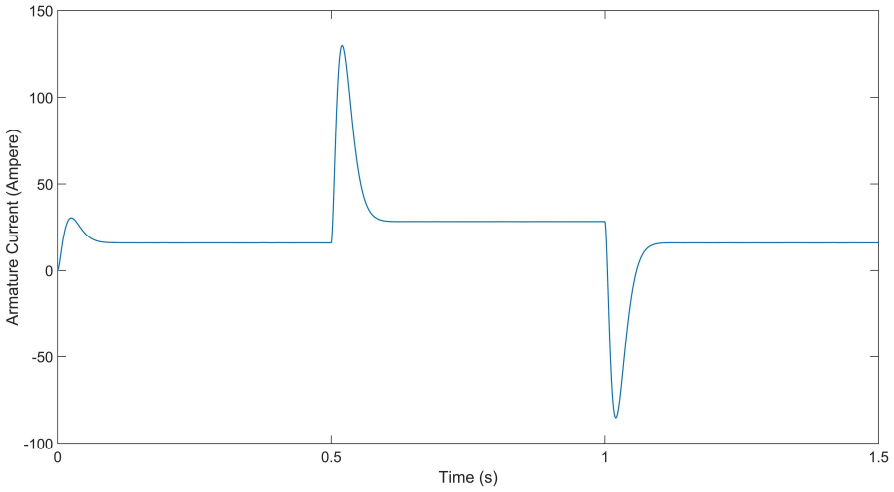

Figure 3.30 Armature current of nonlinear time-frequency speed control scheme when reference speed suddenly changes and sensor noise is introduced

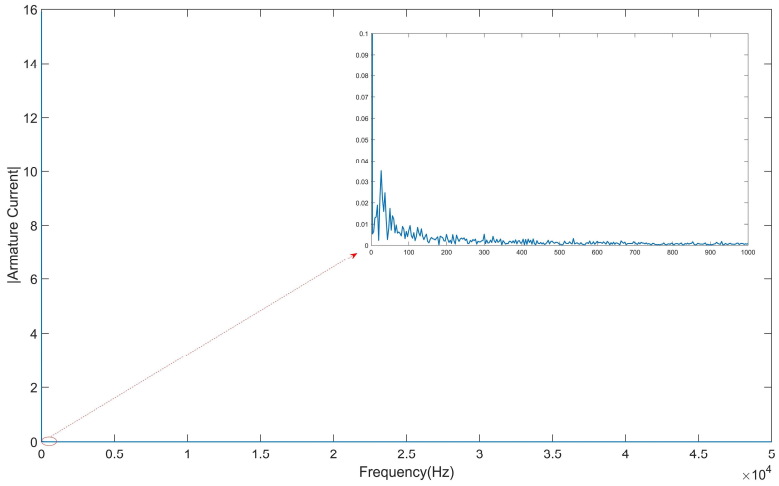

Figure 3.31 Armature current spectrum of PID speed control scheme when reference speed suddenly changes and sensor noise is introduced

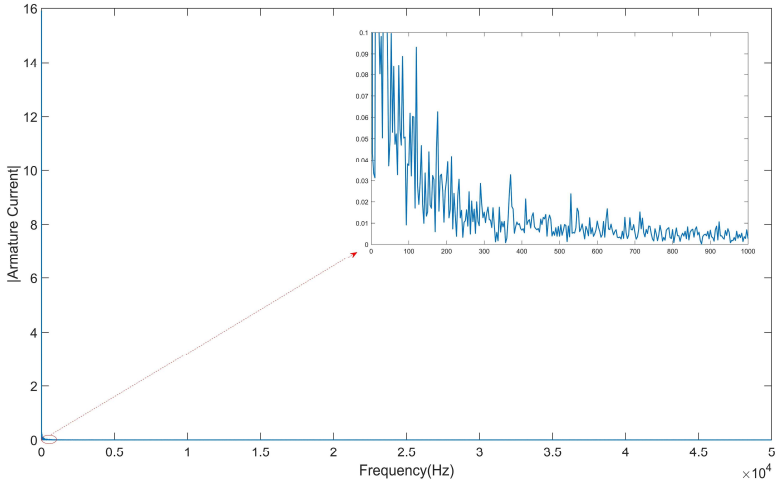

Figure 3.32 Armature current spectrum of fuzzy logic speed control scheme when reference speed suddenly changes and sensor noise is introduced

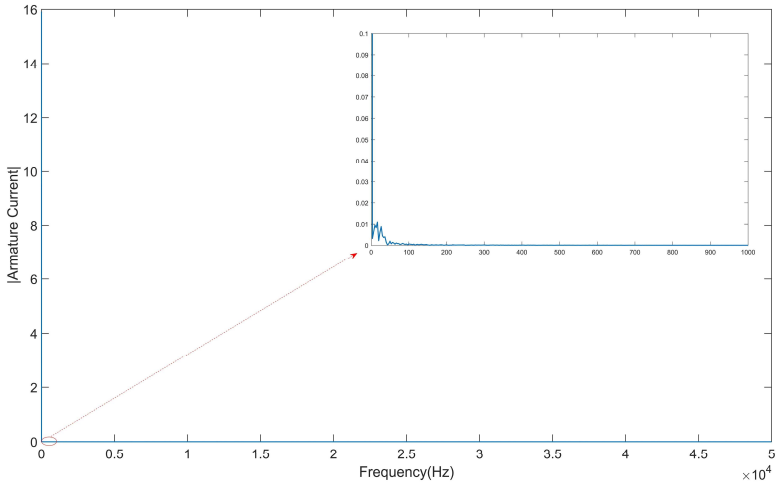

Figure 3.33 Armature current spectrum of nonlinear time-frequency speed control scheme when reference speed suddenly changes and sensor noise is introduced

Table 3.9 lists the corresponding P_{inavg} associated with the PID speed control scheme, fuzzy logic speed control scheme, and nonlinear time-frequency control scheme. According to Table 3.9, it is clear that when subject to the same time-domain performance, the motor with the nonlinear time-frequency speed control is most energy efficient of the three schemes.

Table 3.9 Average input power of the motor system with three speed control schemes when reference speed suddenly changes and sensor noise is introduced

Time (sec)	P_{inavg} (KW)		
	PID	FLC	NTFC
0.00 - 1.50	1.350	1.365	1.309

The next study being considered for the evaluation is described as follows:

$$Reference\,Speed = 90\%\,Rated,\ 0.0 \le t \le 1.5\ ,\ \text{and}\ \ External\ Load = \begin{cases} Rated,\ 0.0 \le t \le 0.5 \\ 0, \qquad 0.0 \le t \le 0.5 \\ Rated,\ 0.0 \le t \le 0.5 \end{cases}.$$

The motor system is operated at 90% rated speed. A constant external torque load with the rated value is applied to the rotor shaft. At t = 0.5 second, this external torque load is abruptly removed. After 0.5 second, it is re-applied to the rotor shaft. This case is designed to test the performance of the three control schemes subject to sudden external torque load changes.

Figure 3.34 - Figure 3.36 are the corresponding speed tracking responses of the three control scheme. Detailed comparisons of their time-domain performances are listed in Table 3.10.

It can be seen in Figure 3.34 - Figure 3.36 that the PID speed control scheme has the lowest overshoots when external torque load suddenly changes, while the nonlinear time-frequency speed control scheme has the largest overshoot. It seems the nonlinear time-frequency speed control scheme is the most vulnerable to external torque load changes. However, according to Table 3.10, it is seen that the nonlinear time-frequency speed control scheme has the shortest time-to-settle of the three schemes. Therefore, it can be stated that all three schemes performs well in terms of speed tracking and each of them has its own benefits in mitigating the negative effects induced by sudden torque load changes.

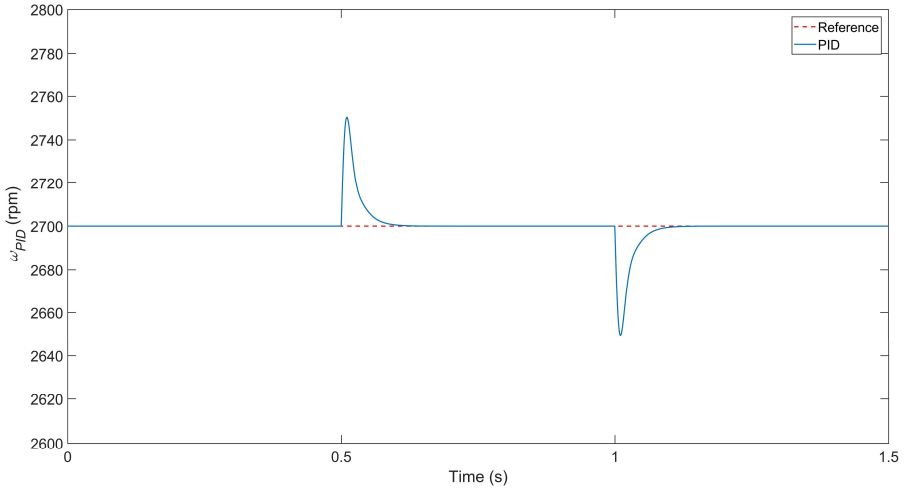

Figure 3.34 Speed tracking response of PID speed control scheme when external torque load suddenly changes

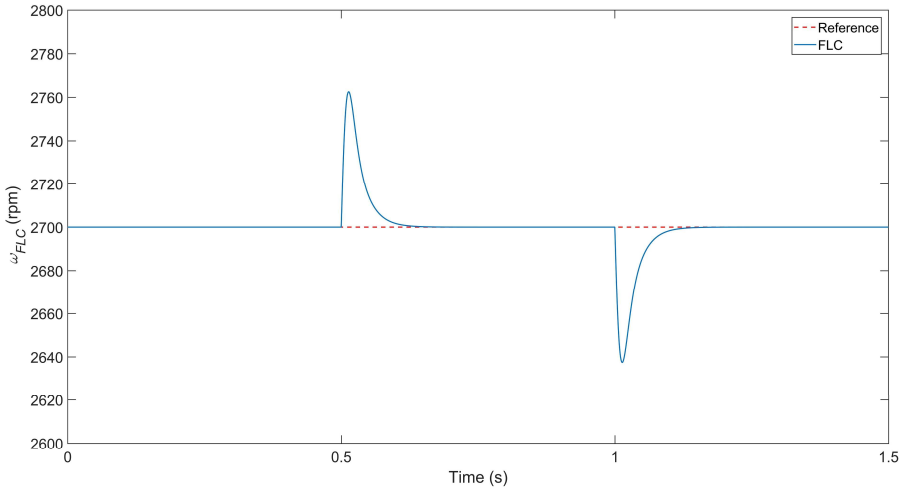

Figure 3.35 Speed tracking response of fuzzy logic speed control scheme when external torque load suddenly changes

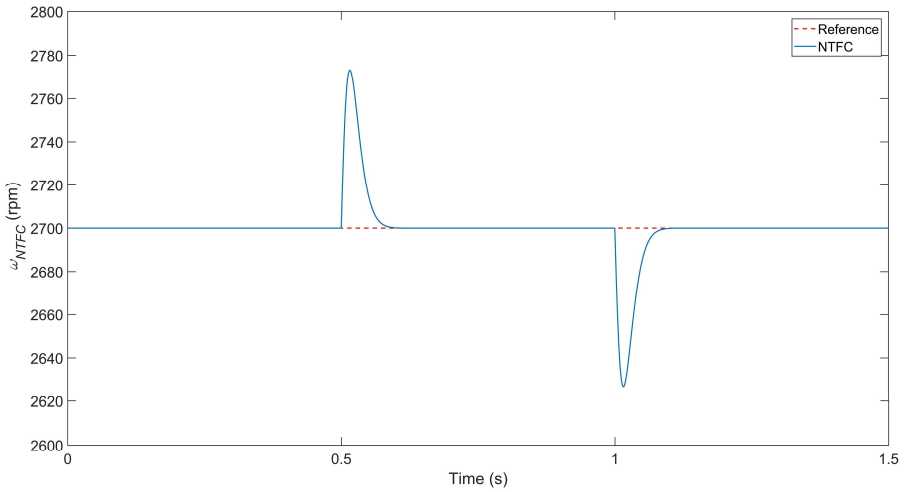

Figure 3.36 Speed tracking response of nonlinear time-frequency speed control scheme when external torque load suddenly changes

Table 3.10 Comparisons of time-domain performance of the three control schemes when external torque load suddenly changes

Time (sec)	Time to Settle (sec)			Overshoot (%)		
	PID	FLC	NTFC	PID	FLC	NTFC
0.50 - 1.00	0.087	0.106	0.077	1.866	2.316	2.712
1.00 - 1.50	0.087	0.106	0.077	1.866	2.316	2.712

Figure 3.37 - Figure 3.39 demonstrate the armature control voltage generated by the three control schemes. It can be seen that they all illustrate similar voltage profiles. The corresponding armature current induced in the PM brushed DC motor is illustrated in Figure 3.40 - Figure 3.42.

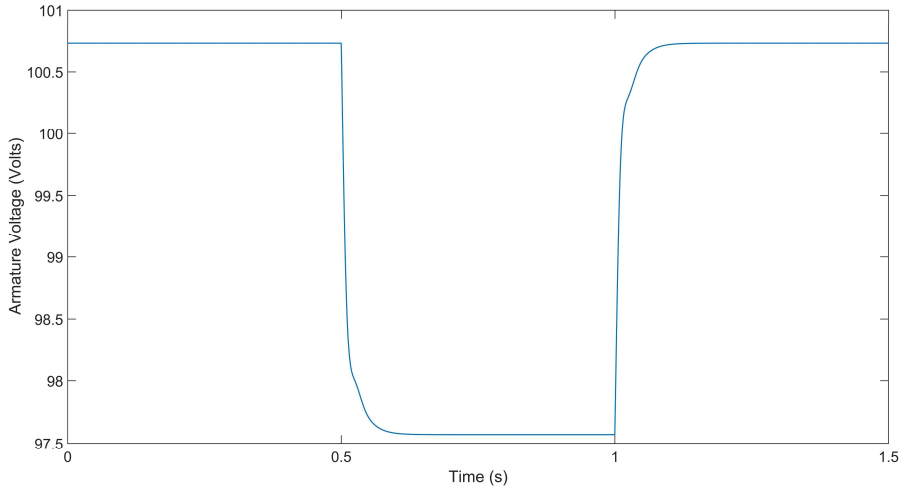

Figure 3.37 Armature control voltage generated by PID speed control scheme when external torque load suddenly changes

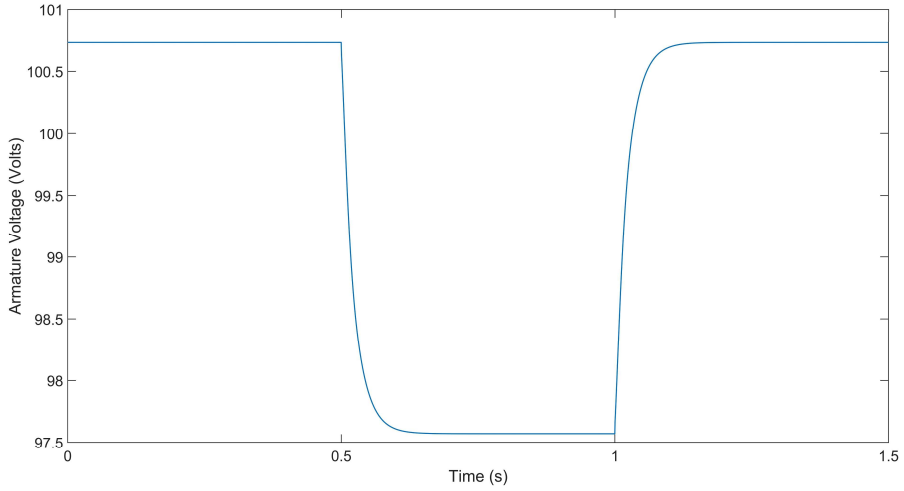

Figure 3.38 Armature control voltage generated by fuzzy logic speed control scheme when external torque load suddenly changes

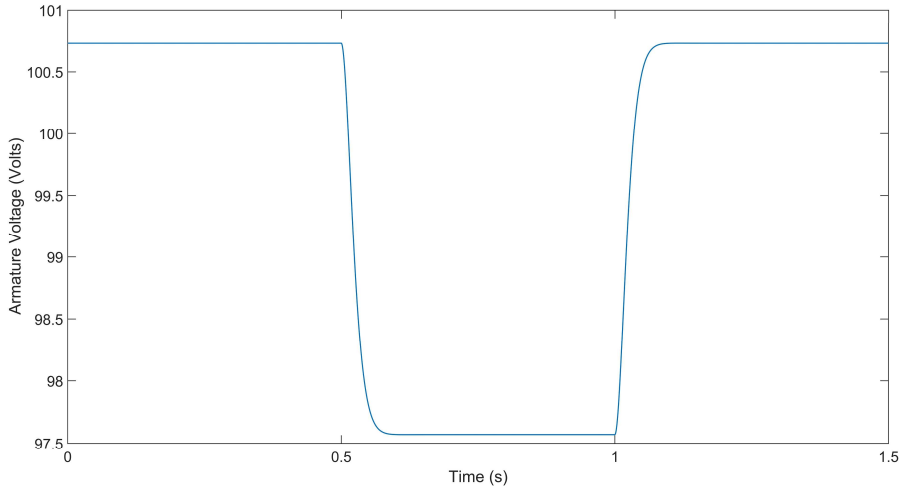

Figure 3.39 Armature control voltage generated by nonlinear time-frequency speed control scheme when external torque load suddenly changes

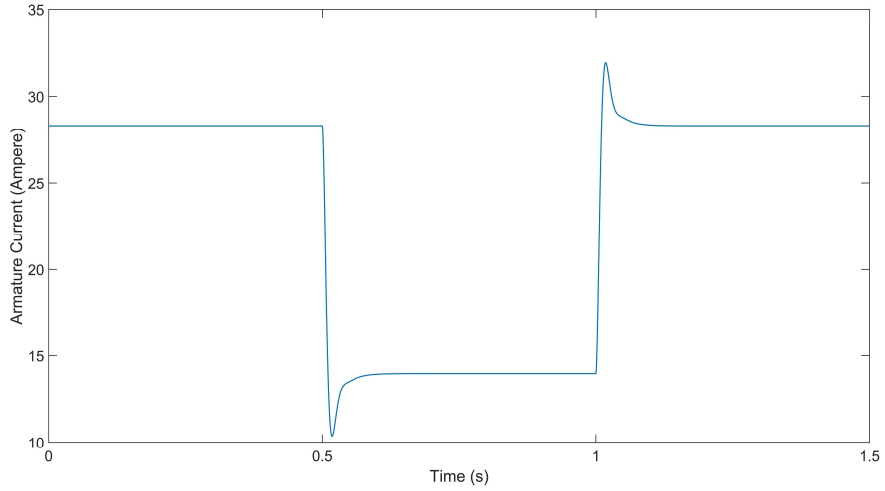

Figure 3.40 Armature current of PID speed control scheme when external torque load suddenly changes

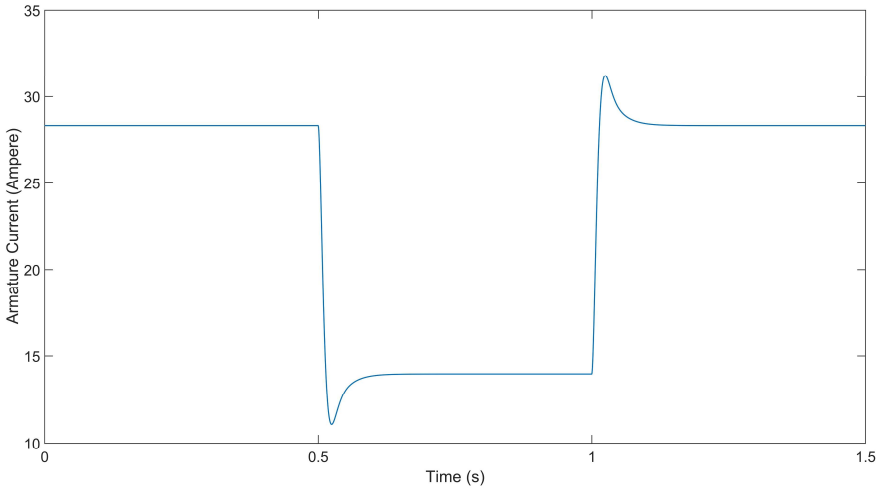

Figure 3.41 Armature current of fuzzy logic speed control scheme when external torque load suddenly changes

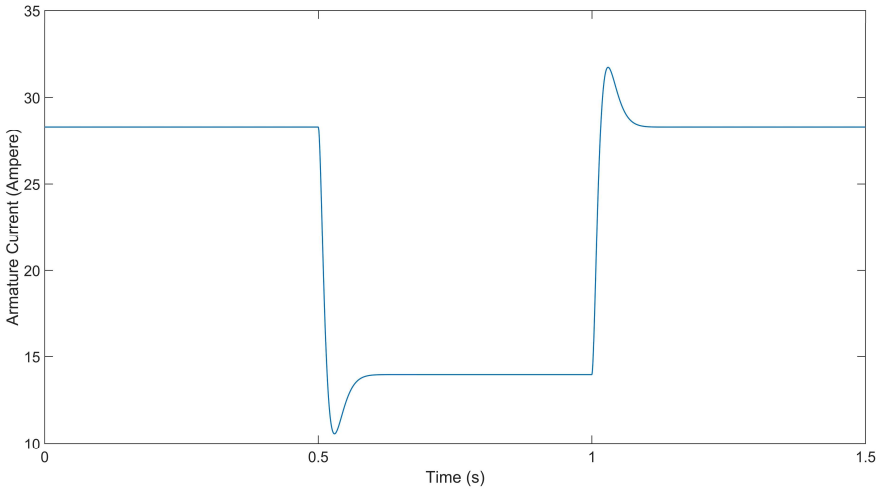

Figure 3.42 Armature current of nonlinear time-frequency speed control scheme when external torque load suddenly changes

According to Figure 3.40 - Figure 3.42, the armature current profile of the PID speed control scheme, fuzzy logic speed control scheme, and nonlinear time-frequency

speed control scheme all experience overshoots when external torque load is suddenly removed or applied. The motor under PID speed control has the largest current overshoot (approximately 18 ampere when external torque load changes from rated to zero or vice versa). The current overshoots in the nonlinear time-frequency speed control and fuzzy logic speed control schemes are slightly lower at 17.75 ampere and 17.26 ampere, respectively.

Table 3.11 lists the corresponding P_{inavg} associated with each control scheme. Clearly, all three schemes have similar power consumption. Overall, the three control schemes all demonstrate satisfactory performances that are fast, accurate, efficient, and robust when external torque load suddenly changes.

Table 3.11 Average input power of the motor system with three speed control schemes when external torque load suddenly changes

Time (sec)	P_{inavg} (KW)		
	PID	FLC	NTFC
0.00 - 1.50	2.356	2.355	2.355

To further evaluate the robustness of the nonlinear time-frequency speed control scheme when external torque load abruptly varies, the sensor noise illustrated in Figure 3.21 is again added to the motor speed measurement. Figure 3.43 - Figure 3.45 demonstrate the corresponding speed responses of the PID speed control scheme, fuzzy logic speed control scheme, and nonlinear time-frequency speed control scheme,

respectively. It is seen that the performances of all three control schemes are influenced by the introduced noise to different degrees. The fuzzy logic speed control scheme is the most seriously influenced. Its tracking accuracy near the reference point deteriorates severely. This is further confirmed by referring to Table 3.12 where the time-domain performances of the three schemes under sudden torque load changes are listed. It can be seen that the fuzzy logic speed control is not able to guarantee a 2% steady-state error when the motor speed reaches the desired reference value. For the PID speed control, based on Figure 3.43, it can be seen that even though there is some obvious fluctuations of the motor speed near the reference point, it is still able to maintain a performance similar to Figure 3.22 (Table 3.12). The injected sensor noise has almost no effect on the performance of the nonlinear time-frequency speed control (see Figure 3.43 and Table 3.12), hence being the most robust of the three schemes.

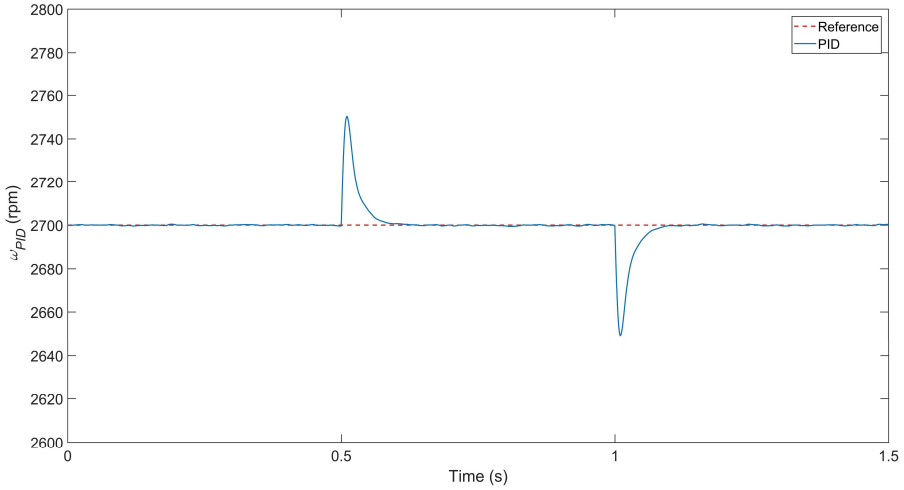

Figure 3.43 Speed tracking response of PID speed control scheme when external torque load suddenly changes and sensor noise is introduced

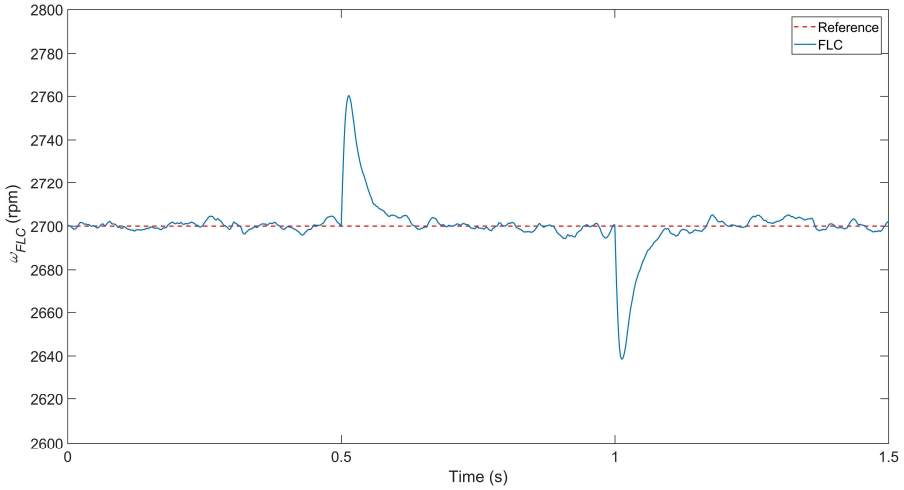

Figure 3.44 Speed tracking response of fuzzy logic speed control scheme when external torque load suddenly changes and sensor noise is introduced

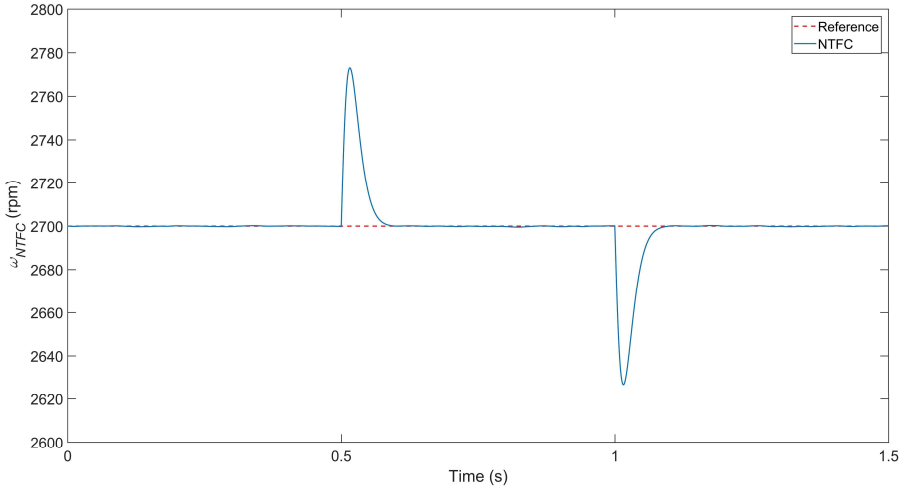

Figure 3.45 Speed tracking response of nonlinear time-frequency speed control scheme when external torque load suddenly changes and sensor noise is introduced

Table 3.12 Comparisons of time-domain performance of the three control schemes when external torque load suddenly changes and sensor noise is introduced

Time (sec)	Time to Settle (sec)			Overshoot (%)		
	PID	FLC	NTFC	PID	FLC	NTFC
0.50 - 1.00	0.084	None	0.077	1.863	2.234	2.705
1.00 - 1.50	0.086	None	0.078	1.872	2.276	2.713

Figure 3.46 - Figure 3.48 display the armature control voltages generated by the three control schemes in response to the imposed sensor noise. The corresponding armature currents induced in the motor are shown in Figure 3.49 - Figure 3.51. It is obvious that the voltage and current profiles of the nonlinear time-frequency speed control are almost identical to Figure 3.37 and Figure 3.40 where the effect of sensor noise was not considered. The voltage and current profiles of the other two schemes, especially the fuzzy logic speed control, are laden with high frequency oscillations. Such unstable profiles would not only put a huge burden on the associated power electronic devices, they would cause more energy losses as well. Figure 3.52 - Figure 3.54 further illustrates the frequency spectra of the motor armature current associated with each control scheme. It can be seen that the nonlinear time-frequency speed control scheme has the best frequency domain performance, while the fuzzy logic speed control scheme has the worst.

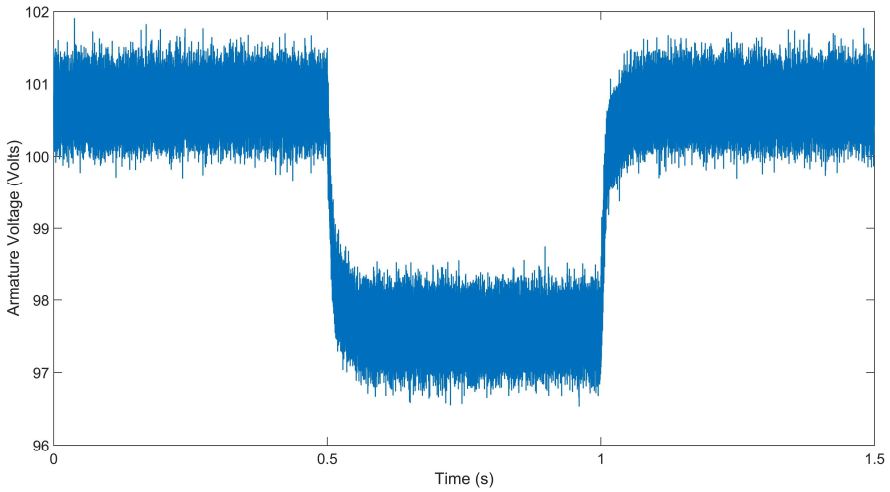

Figure 3.46 Armature control voltage generated by PID speed control scheme when external torque load suddenly changes and sensor noise is introduced

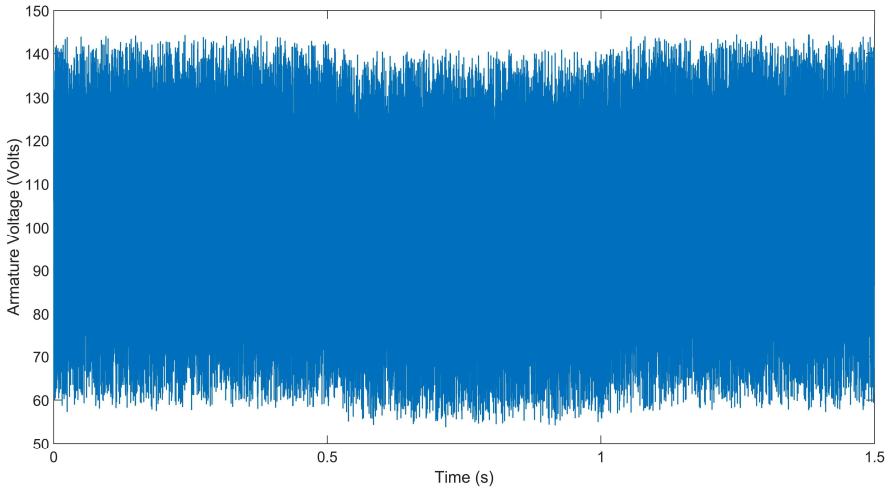

Figure 3.47 Armature control voltage generated by fuzzy logic speed control scheme when external torque load suddenly changes and sensor noise is introduced

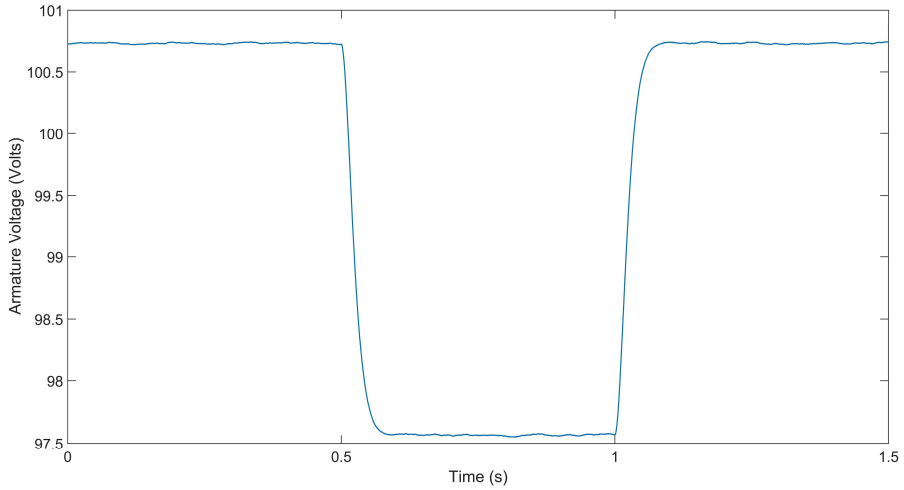

Figure 3.48 Armature control voltage generated by nonlinear time-frequency speed control scheme when external torque load suddenly changes and sensor noise is introduced

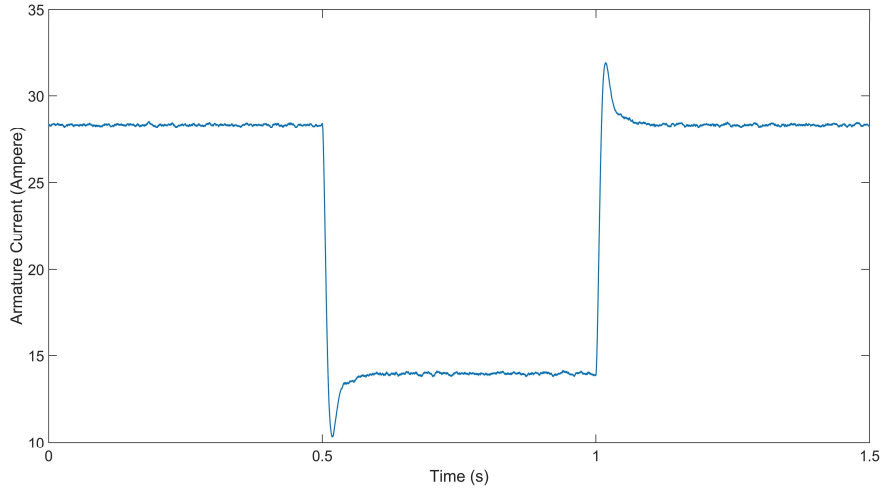

Figure 3.49 Armature current of PID speed control scheme when external torque load suddenly changes and sensor noise is introduced

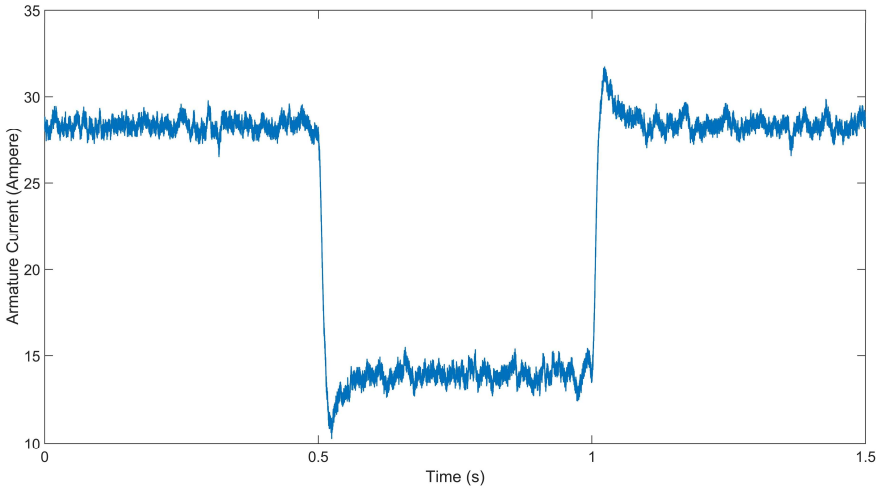

Figure 3.50 Armature current of fuzzy logic speed control scheme when external torque load suddenly changes and sensor noise is introduced

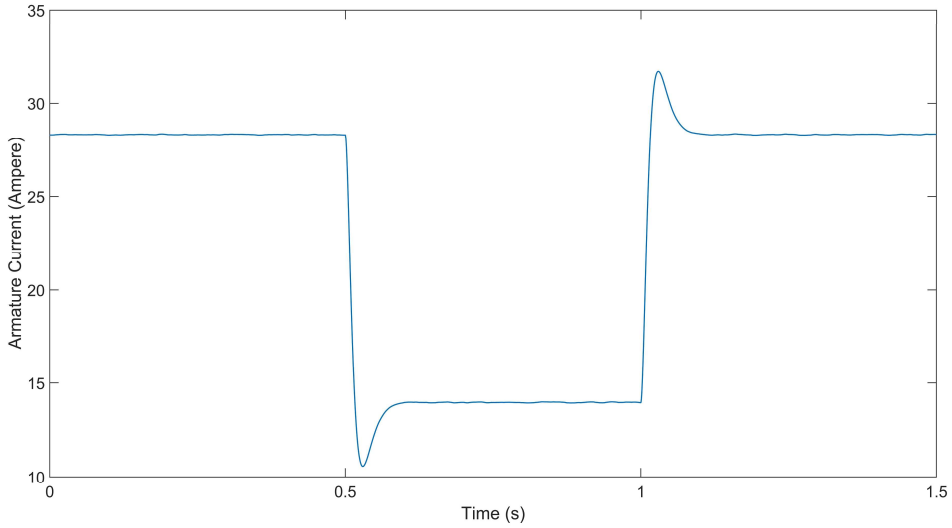

Figure 3.51 Armature current of nonlinear time-frequency speed control scheme when external torque load suddenly changes and sensor noise is introduced

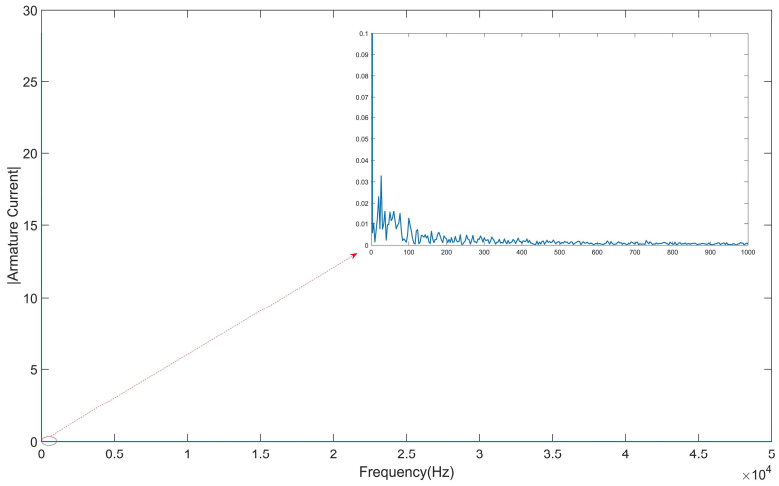

Figure 3.52 Armature current spectrum of PID speed control scheme when external torque load suddenly changes and sensor noise is introduced

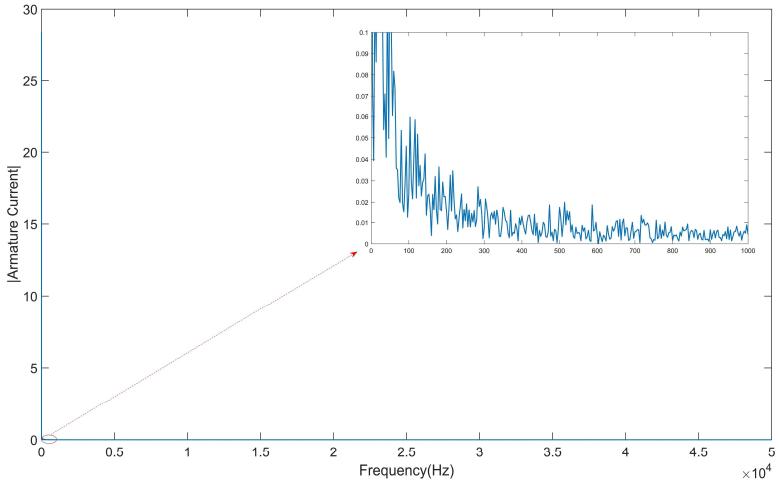

Figure 3.53 Armature current spectrum of fuzzy logic speed control scheme when external torque load suddenly changes and sensor noise is introduced

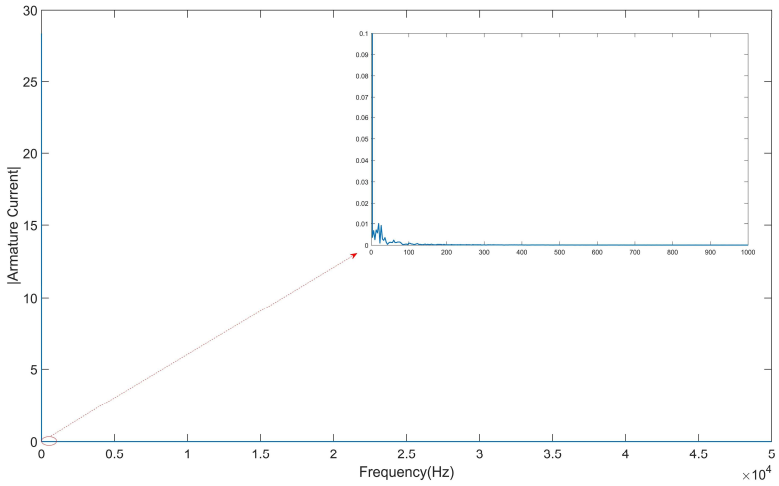

Figure 3.54 Armature current spectrum of nonlinear time-frequency speed control scheme when external torque load suddenly changes and sensor noise is introduced

Table 3.13 lists the P_{inavg} associated with each control scheme when sensor noise is injected into the motor system. It can be seen that the PID speed control is the most energy-costly and the fuzzy logic speed control is the least. The reason that fuzzy logic speed control scheme shows the lowest average input power with its terrible voltage and current profiles is due to the fact that its time-domain speed tracking performance is not in line with the PID speed control and nonlinear time-frequency speed control schemes. Specifically, when sensor noise is introduced into the motor system, both the PID and nonlinear time-frequency speed control schemes are able to maintain their speed tracking performance and the motor is still able to work at its reference speed. While for the fuzzy logic speed control scheme, its speed tracking performance is seriously deteriorated by the noise and the motor speed fluctuates about the reference value. Therefore, even though its voltage and current profiles are laden with high frequency oscillations of alarming

amplitude, its average input power is still small since its average operating speed is lower than the PID and nonlinear time-frequency speed control schemes.

Table 3.13 Average input power of the motor system with three speed control schemes when external torque load suddenly changes and sensor noise is introduced

Time (sec)	P_{inavg} (KW)		
	PID	FLC	NTFC
0.00 - 1.50	2.356	2.355	2.355

In summary, the introduced nonlinear time-frequency speed control scheme is shown to have satisfactory performance in the speed control of the PM brushed DC motor. It is preferred over the other two schemes under harsh working conditions where system stability, operation reliability, high control precision, fast response, and robustness are demanded.

3.4 Nonlinear Time-Frequency Position Control of PM Brushed DC Motors

3.4.1 Nonlinear Time-Frequency Position Control Scheme for PM Brushed DC Motors

The novel nonlinear time-frequency speed control scheme presented in Figure 3.2 can also be applied to the precise position tracking of PM brushed DC motors. However, to control motor angular position, the time-delay inherent of the on-line identification process has to be compensated. This is achieved by introducing a simple proportional controller into the speed control scheme without intruding upon the basic configuration. Figure 3.55 illustrates the nonlinear time-frequency position control scheme for the PM

brushed DC motor model presented in Equation (3.8) where both the rotor angular velocity ω_{PMDC} and rotor angular position θ_{PMDC} are selected as the system variables to be controlled. In Figure 3.55, θ_{NTFC} is the actual angular position of the motor rotor, θ^*_{NTFC} is the desired angular position of the rotor, and E_{NTFC} is the difference between θ^*_{NTFC} and θ_{NTFC}. Note that the ω^*_{NTFC} in Figure 3.2 for speed control was the desired reference speed, while the ω^*_{NTFC} in Figure 3.55 for position tracking is a time-varying reference speed generated from the simple proportional controller **P**. The proportional controller **P** is assigned a small gain of 0.2 to generate the desired angular velocity ω^*_{NTFC} of the rotor. The controller architecture along with the underlying control logic is identical to the one seen in Figure 3.2.

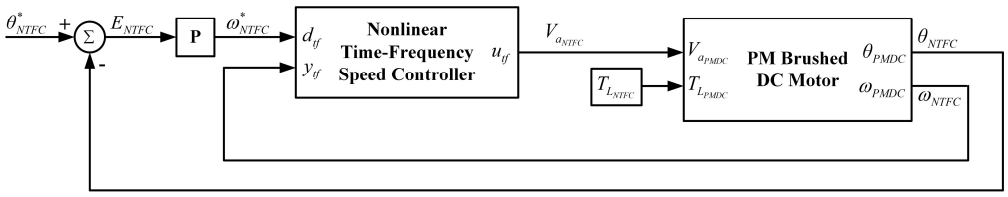

Figure 3.55 Illustration of the nonlinear time-frequency position control scheme for PM brushed DC motors

To demonstrate the quality of the above nonlinear time-frequency position control scheme, its performance in negating system disturbances during position tracking is

evaluated against the popular PID position control scheme and fuzzy logic position control scheme using the same PM brushed DC motor specs found in Table 3.2.

3.4.2 PID Position Control Scheme for PM Brushed DC Motors

The PID position control scheme employed for the position tracking of PM brushed DC motors is illustrated in Figure 3.56.

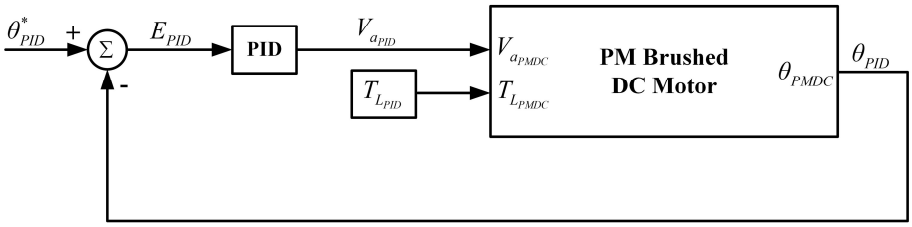

Figure 3.56 Illustration of the PID position control scheme for PM brushed DC motors

where E_{PID} is the error between the desired rotor position θ^*_{PID} and the actual rotor position θ_{PID}; the algorithm of the PID controller is illustrated by Equation (3.11). Its gain values are listed in Table 3.14.

$$V_{a_{PID}}(n) = k_p E_{PID}(n) + k_i [V_{a_{PID}}(n-1) + \frac{E_{PID}(n) + E_{PID}(n-1)}{2} T_s] + k_d \frac{E_{PID}(n) - E_{PID}(n-1)}{T_s} \tag{3.11}$$

Table 3.14 Parameters of the PID position control scheme for PM brushed DC motors

PID Parameters	Value
k_p	0.1101
k_i	0.0210
k_d	0.0019

3.4.3 Fuzzy Logic Position Control Scheme for PM Brushed DC Motors

The fuzzy logic position control scheme employed for the position tracking of the target PM brushed DC motor is illustrated in Figure 3.57.

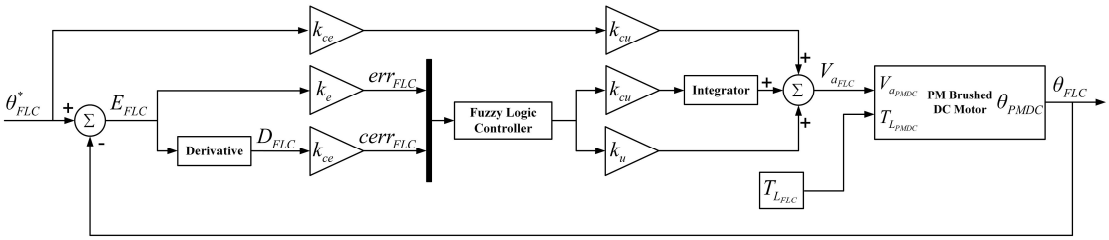

Figure 3.57 Illustration of the fuzzy logic position control scheme for PM brushed DC motors

where E_{FLC} is the error between the reference rotor position θ^*_{FLC} and the actual rotor position θ_{FLC}. The corresponding membership functions and fuzzy rules are indicated in Figure 3.58 - Figure 3.60 and Table 3.15.

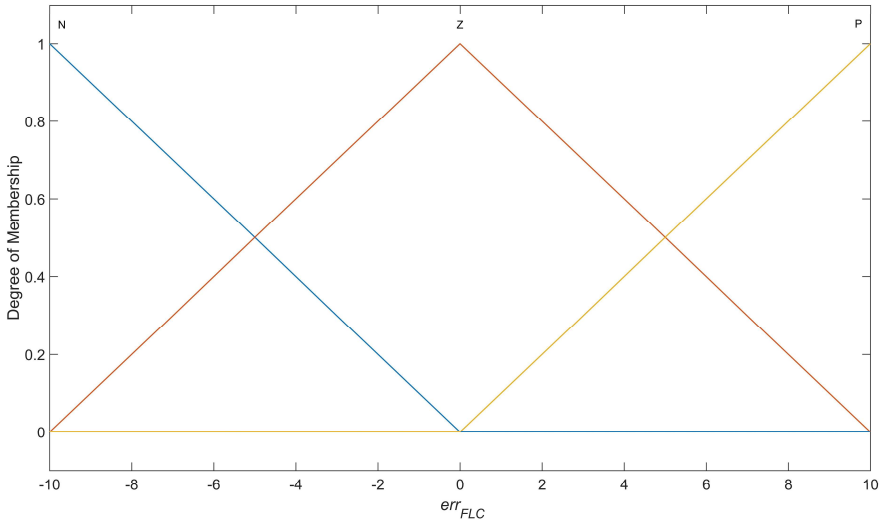

Figure 3.58 Input membership function of err_{FLC} for fuzzy logic position control scheme

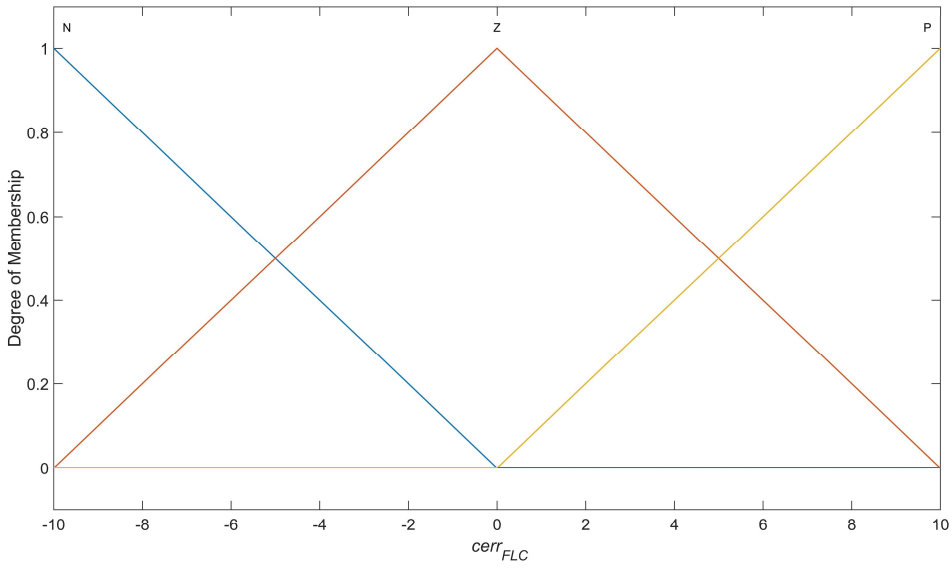

Figure 3.59 Input membership function of $cerr_{FLC}$ for fuzzy logic position control scheme

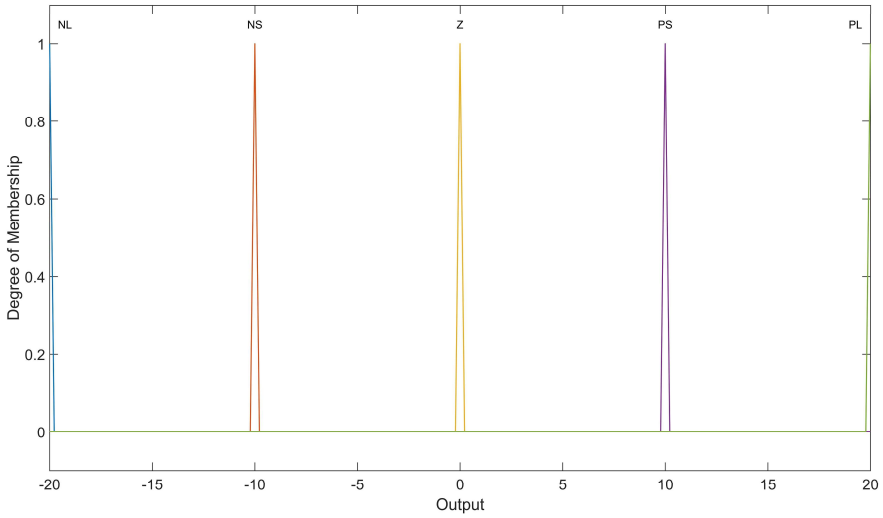

Figure 3.60 Output membership function for fuzzy logic position control scheme

Table 3.15 Fuzzy Rules for fuzzy logic position control scheme

Rule 1	If err_{FLC} is N and $cerr_{FLC}$ is N, then Output is NL
Rule 2	If err_{FLC} is N and $cerr_{FLC}$ is Z, then Output is NS
Rule 3	If err_{FLC} is N and $cerr_{FLC}$ is P, then Output is Z
Rule 4	If err_{FLC} is Z and $cerr_{FLC}$ is N, then Output is NS
Rule 5	If err_{FLC} is Z and $cerr_{FLC}$ is Z, then Output is Z
Rule 6	If err_{FLC} is Z and $cerr_{FLC}$ is P, then Output is PS
Rule 7	If err_{FLC} is P and $cerr_{FLC}$ is N, then Output is Z
Rule 8	If err_{FLC} is P and $cerr_{FLC}$ is Z, then Output is PS
Rule 9	If err_{FLC} is P and $cerr_{FLC}$ is P, then Output is PL

3.4.4 Evaluation of the Position Tracking Performance

The developed nonlinear time-frequency position control scheme is equally robust in tracking the angular position of the motor with desired precision. To demonstrate this, its performance is evaluated against the PID position control and fuzzy logic position control schemes.

Same as in section 3.3, to guarantee a reasonable comparison, all three position control schemes are tuned to behave similarly to a step response under zero torque load. Figure 3.61 - Figure 3.63 display the step responses of the target PM brushed DC motor with PID position control scheme, fuzzy logic position control scheme, and nonlinear time-frequency position control scheme under zero torque load, respectively. Detailed comparisons of their time-domain performance are listed in Table 3.16.

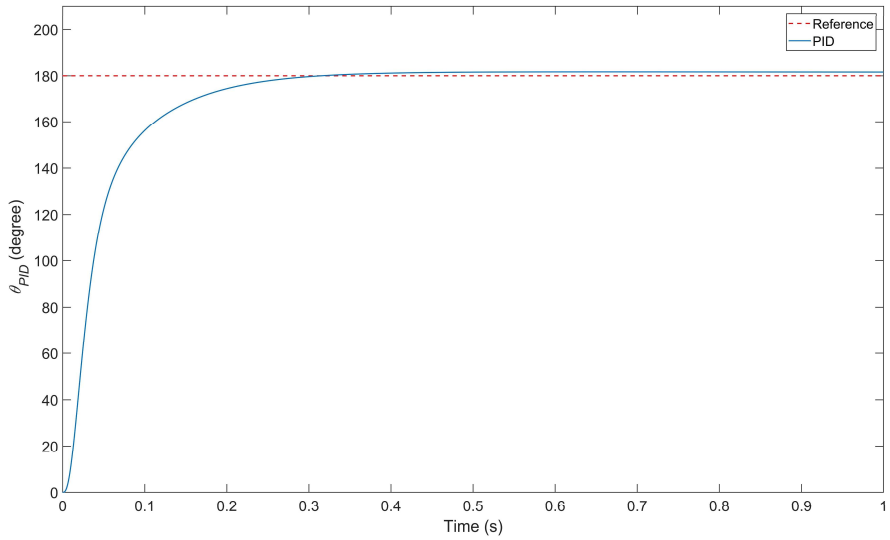

Figure 3.61 Step response of PID position control scheme under zero torque load

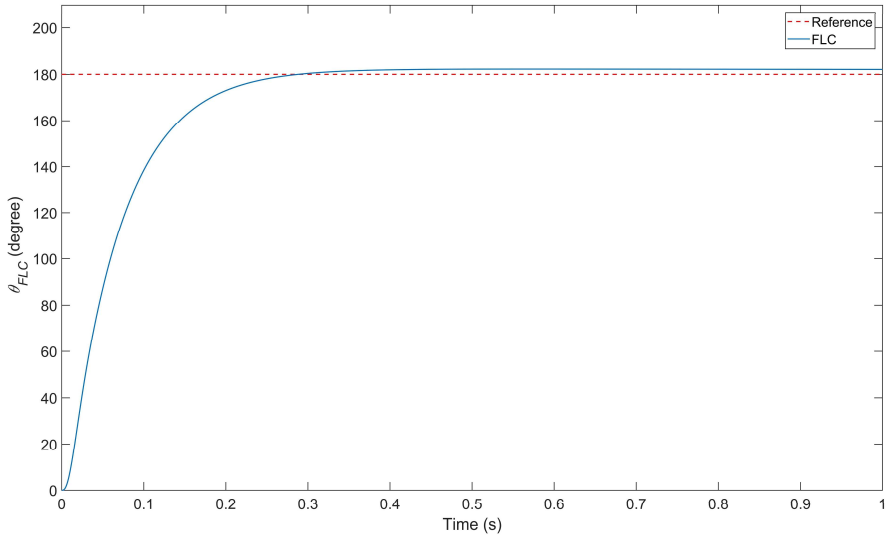

Figure 3.62 Step response of fuzzy logic position control scheme under zero torque load

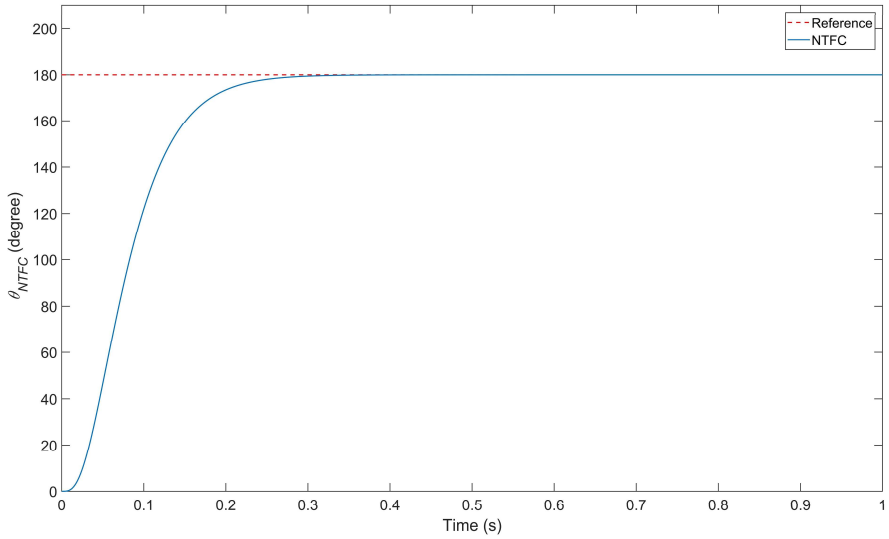

Figure 3.63 Step response of nonlinear time-frequency position control scheme under zero torque load

Table 3.16 Position step response comparisons of the three position control schemes

Performance	PID	FLC	NTFC
Rise Time	0.108 s	0.135 s	0.124 s
Settling Time	0.225 s	0.229 s	0.225 s
Overshoot	0.940 %	1.260 %	0.000 %

Based on Table 3.16, it can be seen that the three control schemes have very similar transient behaviors when there is a step change of the reference from 0^{o} to 180^{o} at $t = 0$ s. However, from Figure 3.61 - Figure 3.63, it can be clearly observed that even though the PID position control scheme and fuzzy logic position control scheme are able to control the rotor position to reach 180^{o} with a steady state error less than 2% and guarantee a similar rise time and settling time as the nonlinear time-frequency position control scheme, they are not able to achieve precise control. The steady state error in the PID position control scheme and fuzzy logic position control scheme are clearly much larger than the nonlinear time-frequency position control scheme. In addition, the step responses of both the PID position control scheme and fuzzy logic positon control scheme have overshoots, while the step response of the nonlinear time-frequency control does not.

To illustrate the superiority of the nonlinear time-frequency position control scheme, a series of studies are performed. The first study being considered for the evaluation is defined as follows:

$$Reference\ Positoin = \begin{cases} 1^o, & 0.0 \le t \le 1.0 \\ 180^o, & 1.0 \le t \le 2.0 \\ 1^o, & 2.0 \le t \le 3.0 \end{cases}, \text{ and } External\ Load = Rated\ .$$

The motor system is activated from being stationary and set to a small initial angular position of 1^o. It then subsequently switches to a large angular position at t = 1.0 second and changes back to 1^o at t = 2.0 second. During the whole process, a constant torque load with the rated value is applied to the shaft. This case is designed to test the performance of the nonlinear time-frequency position control scheme when reference position suddenly changes.

Figure 3.64 - Figure 3.66 display, respectively, the corresponding position tracking response of the PID position control scheme, fuzzy logic position control scheme, and nonlinear time-frequency position control scheme. Detailed time-domain performance comparisons of them are listed in Table 3.17.

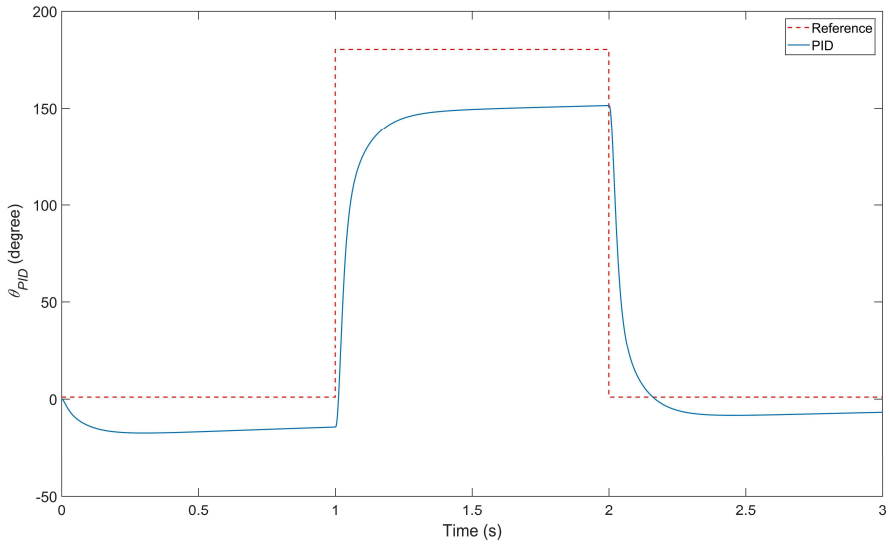

Figure 3.64 Position tracking response of PID position control scheme when reference position suddenly changes

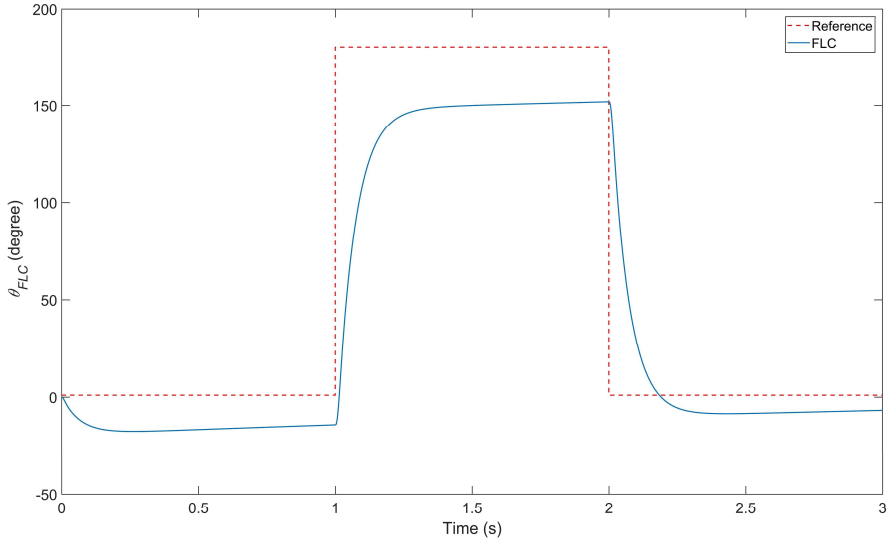

Figure 3.65 Position tracking response of fuzzy logic position control scheme when reference position suddenly changes

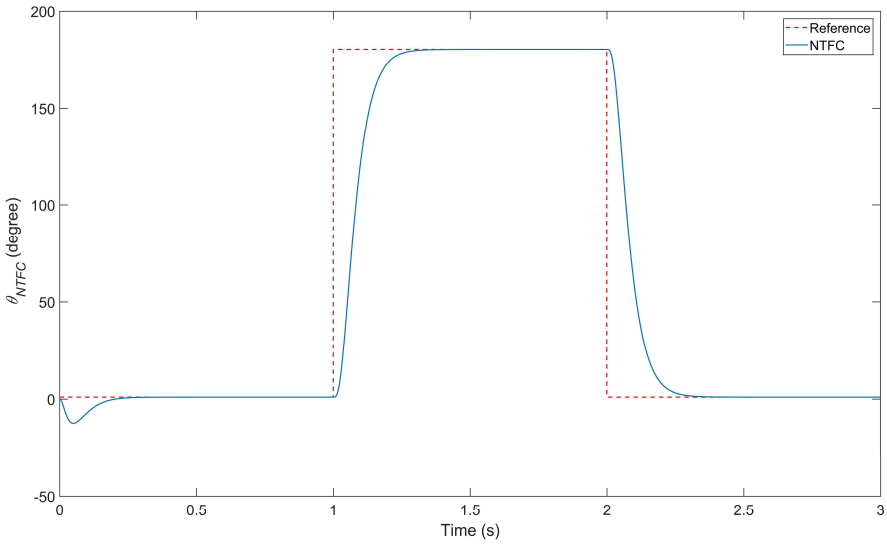

Figure 3.66 Position tracking response of nonlinear time-frequency position control scheme when reference position suddenly changes

Table 3.17 Comparisons of time-domain performance of the three control schemes when reference position suddenly changes

Time (sec)	Rise Time (sec)			Time to Settle (sec)			Overshoot (%)		
	PID	FLC	NTFC	PID	FLC	NTFC	PID	FLC	NTFC
0.00 - 1.00	None	None	0.092	None	None	0.259	0.000	0.000	0.000
1.00 - 2.00	None	None	0.124	None	None	0.227	0.000	0.000	0.000
2.00 - 3.00	0.079	0.112	0.125	None	None	0.229	0.034	0.075	0.000

It is seen from Figure 3.64 - Figure 3.66 and Table 3.17 that the nonlinear time-frequency position control scheme performs significantly better than the PID position control and fuzzy logic position control scheme when the reference position is suddenly changed. Both the PID position control and fuzzy logic position control scheme fail to

reach the reference position with the desired speed and precision. It can also be observed that the applied external torque load has a severe negative impact on the tracking performance of the two position control schemes. Specifically, it takes an extremely long rise time and time-to-settle for the two control position schemes to bring the rotor from the negative position caused by the applied external torque load to the new reference position. As for the nonlinear time-frequency position control scheme, not only the corresponding rise time and time-to-settle are shorter, it has no overshoots regardless of how the reference positon is changed. In addition, compared with the other two position control schemes which fails to generate enough torque to overcome the large external torque load initially applied on the rotor, the nonlinear time-frequency position control scheme only takes about 0.2 second to restore the rotor back to 0^{o} .

Figure 3.67 - Figure 3.69 illustrate the armature control voltage generated by the PID position control scheme, fuzzy logic speed position control scheme, and nonlinear time-frequency position control scheme, respectively. The corresponding armature current are displayed in Figure 3.70 - Figure 3.72. It can be seen that the overshoots caused by the sudden reference position changes in both the armature voltage and current in the nonlinear time-frequency position control are much smaller than the other two schemes.

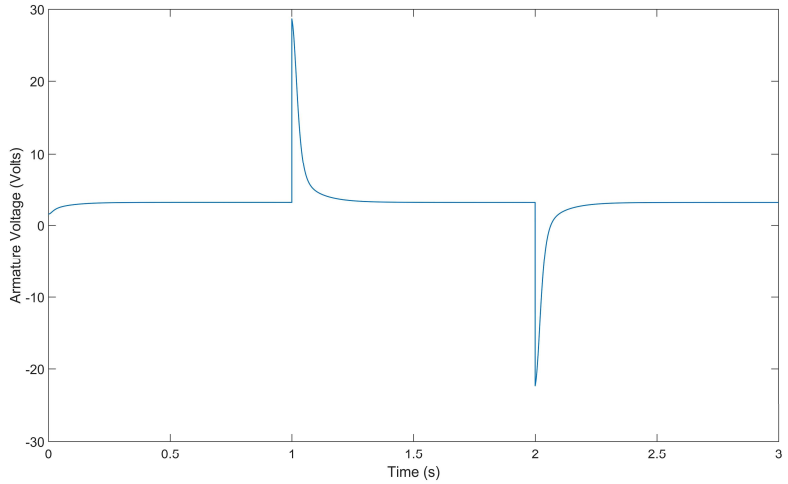

Figure 3.67 Armature control voltage generated by PID position control scheme when reference position suddenly changes

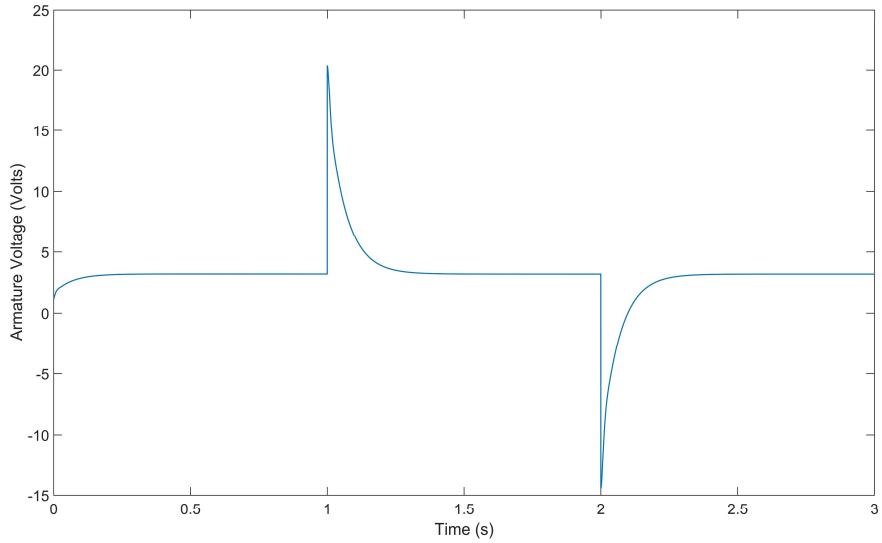

Figure 3.68 Armature control voltage generated by fuzzy logic position control scheme when reference position suddenly changes

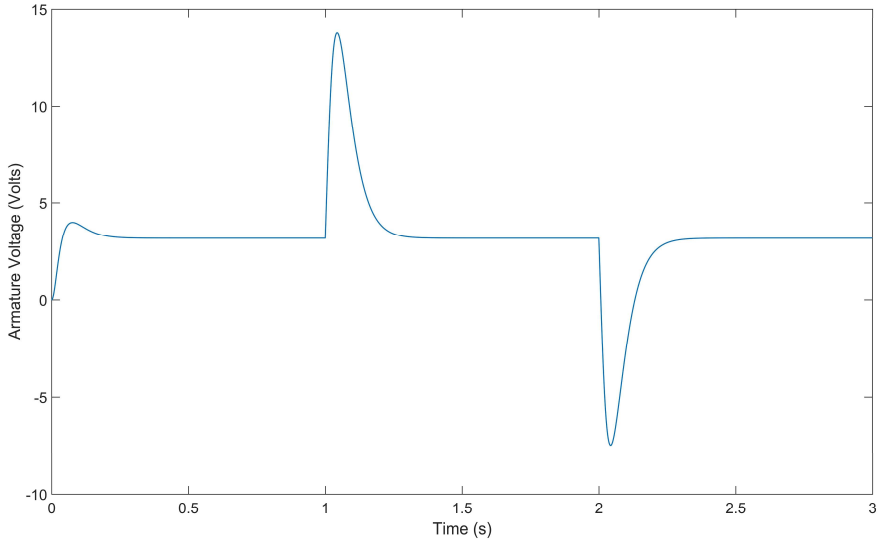

Figure 3.69 Armature control voltage generated by nonlinear time-frequency position control scheme when reference position suddenly changes

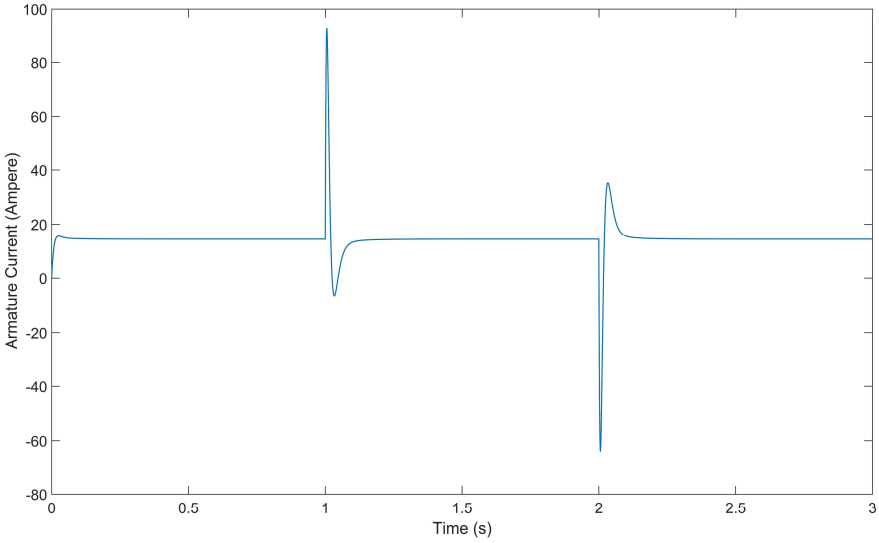

Figure 3.70 Armature current of PID position control scheme when reference position suddenly changes

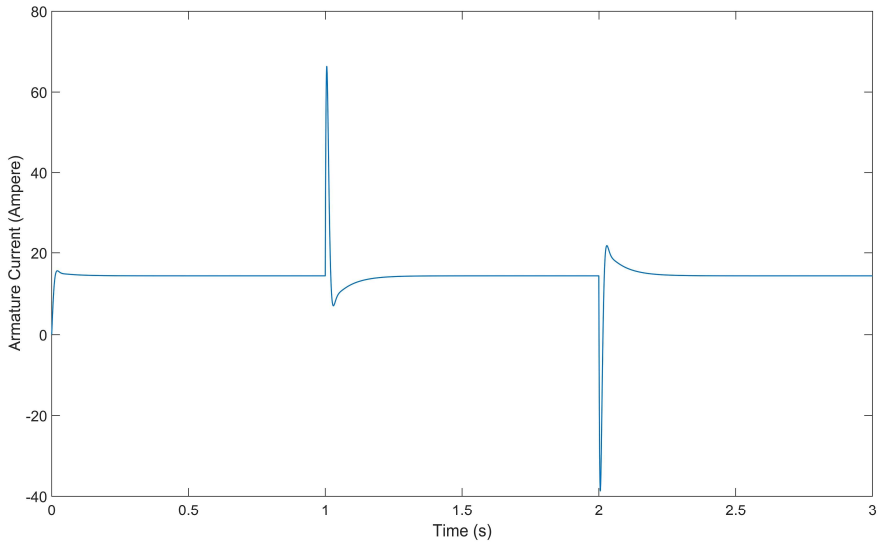

Figure 3.71 Armature current of fuzzy logic position control scheme when reference position suddenly changes

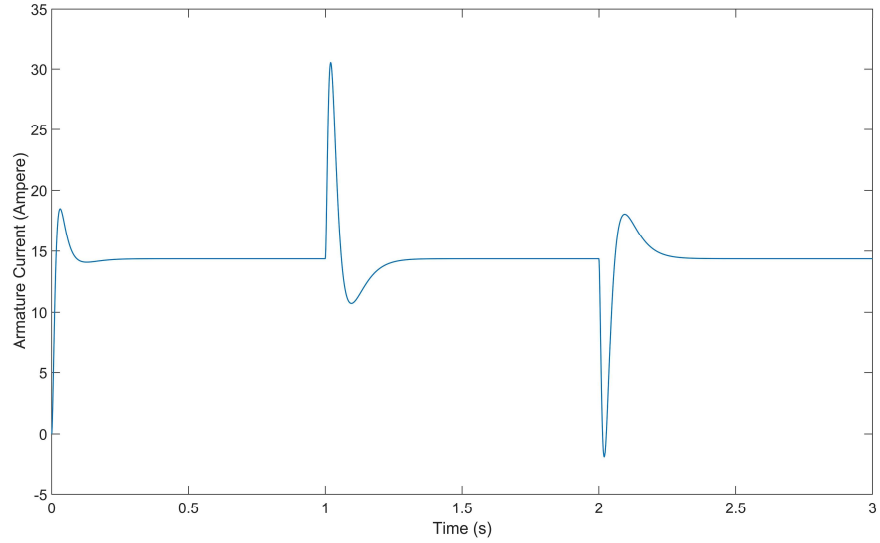

Figure 3.72 Armature current of nonlinear time-frequency position control scheme when reference position suddenly changes

Table 3.19 tabulates the corresponding P_{inavg} associated with each of the control scheme. It can be seen that compared with the nonlinear time-frequency position control, the PID position control and fuzzy logic position control scheme fail to achieve a satisfactory position tracking. In addition, they both consume more power.

Table 3.18 Average input power of the motor system with three position control schemes when reference position suddenly changes

Time (sec)	P_{inavg} (W)		
	PID	FLC	NTFC
0.00 - 1.50	60.471	52.803	51.099

Clearly, the position tracking performance of the nonlinear time-frequency position control scheme is unmatched by both PID and fuzzy logic position controls. To further demonstrate its robustness, the impact of sensor noise is once again considered. In addition to the broad band Gaussian white noise found in Figure 3.21, the sensor noise $s_{PMDC}(n)$ depicted in Figure 3.73 is also introduced to the motor system via $\theta_{NTFC} = \theta_{PMDC} + s_{PMDC}$. Figure 3.74 shows the position tracking response of the nonlinear time-frequency position control scheme. It is noted that its counterpart found in Figure 3.66 is position response not afflicted by noise. Clearly, the PM brushed DC motor with nonlinear time-frequency position control is insensitive to sensor noise and robust to sudden reference position changes.

Table 3.19 lists the time-domain position tracking performance of the nonlinear time-frequency position control scheme when sensor noise is introduced. The tolerance of the steady-state error between 0.00 - 1.00 seconds in Table 3.19 is increased from 2% to 10% to avoid underestimating the performance of the nonlinear time-frequency position control scheme. Compared with Figure 3.66, it can be seen that except for a minor decrease in tracking accuracy (where the steady-state error has only increased from less than 0.02^{o} to less than 0.1^{o}) and a slight increase in overshot between 0.00 - 0.10 seconds when the reference position is of a low value, the performance of the nonlinear time-frequency position control scheme is almost unaffected by the introduced sensor noise.

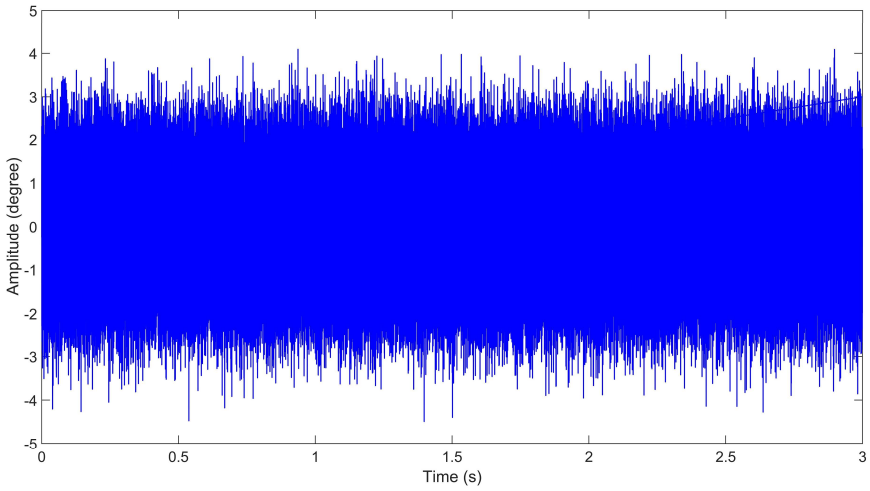

Figure 3.73 Gaussian white noise $s_{PMDC}(n)$

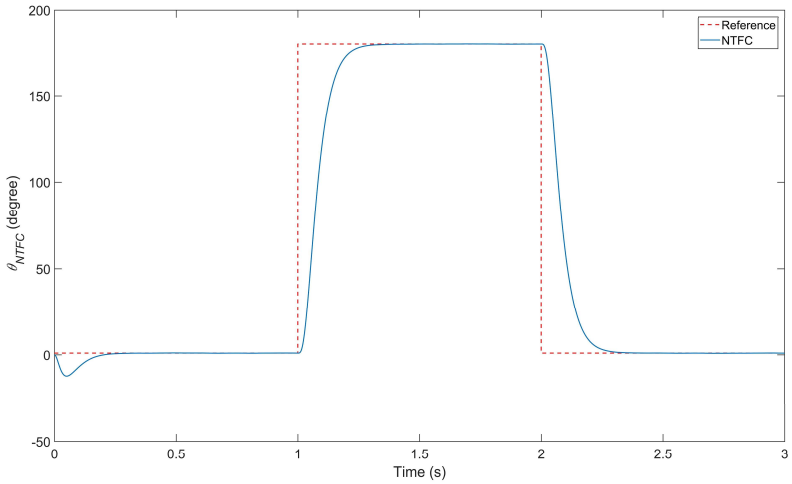

Figure 3.74 Position tracking response of nonlinear time-frequency position control scheme when reference position suddenly changes and sensor noise is introduced

Table 3.19 Time-domain performance of the nonlinear time-frequency position control scheme when reference position suddenly changes and sensor noise is introduced

Time (sec)	Rise Time (sec)	Time to Settle (sec)	Overshoot (%)
0.00 - 1.00	0.100	0.191	10.587
1.00 - 2.00	0.124	0.228	0.030
2.00 - 3.00	0.124	0.228	0.000

Figure 3.75 and Figure 3.76 show the corresponding armature control voltage and current of the PM brushed DC motor under control. The frequency spectrum of the armature current is also displayed in Figure 3.77. It is evident that the voltage and current profiles of the motor are relatively unaffected by the injected noise. This is further confirmed by reviewing Figure 3.77, where most frequency components of the motor

current are seen suppressed. Table 3.20 tabulates the average input power of the motor system using the nonlinear time-frequency position control scheme with and without sensor noise. It can be seen that when sensor noise is introduced, the average input power of the system only increases by approximately 0.004 W, thus further explaining the intact of the voltage and current profiles of the system subject to the noise. Therefore, the nonlinear time-frequency position control scheme is fast, accurate, efficient, robust to sudden reference changes and noise, and most importantly, capable of controlling motor response in both the time and frequency domains.

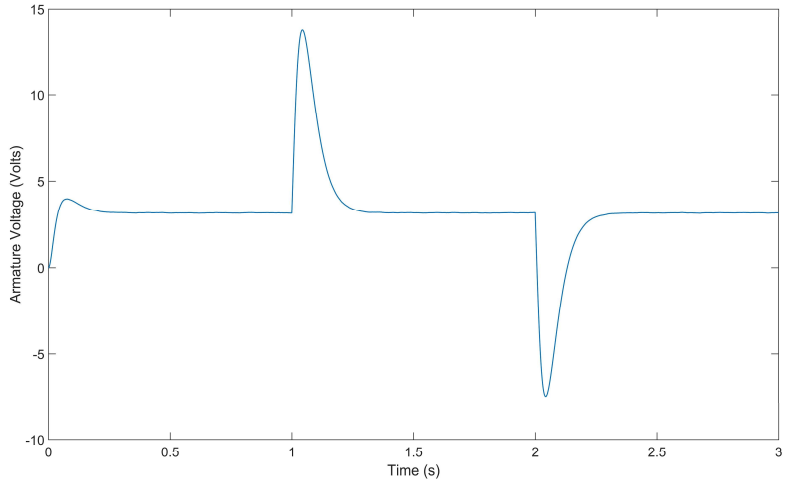

Figure 3.75 Armature control voltage generated by nonlinear time-frequency position control scheme when reference position suddenly changes and sensor noise is introduced

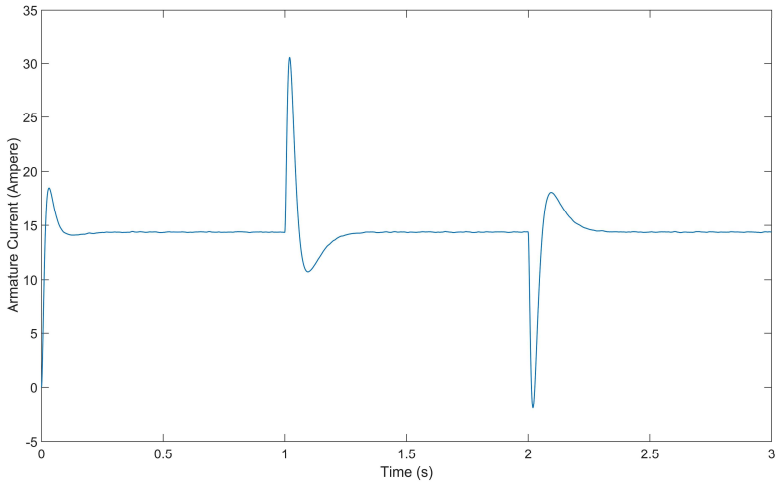

Figure 3.76 Armature current of nonlinear time-frequency position control scheme when reference position suddenly changes and sensor noise is introduced

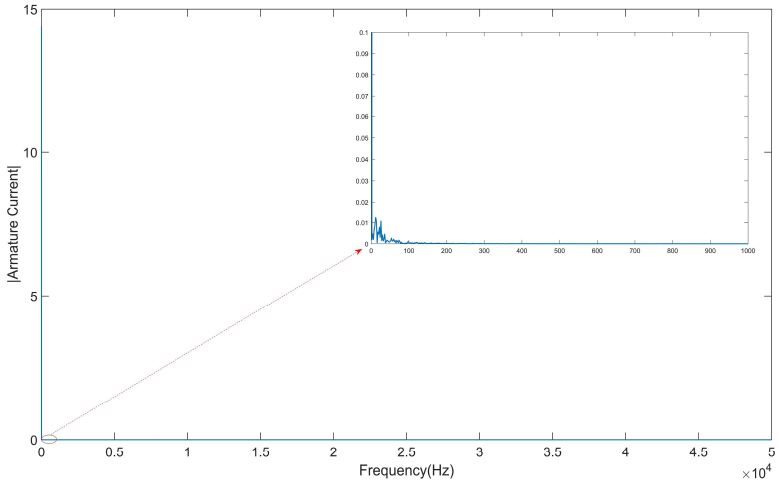

Figure 3.77 Armature current spectrum of nonlinear time-frequency position control scheme when reference position suddenly changes and sensor noise is introduced

Table 3.20 Comparison of the average input power of the motor system with nonlinear time-frequency position control scheme when reference position suddenly changes

Time (sec)	P_{inavg} (W)	
	Without sensor noise	With sensor noise
0.00 - 3.00	51.099	51.103

The next study being considered for the evaluation is described as follows:

$$Reference\ Position = 180^{o},\ 1.0 \le t \le 3.0\text{, and } External\ Load = \begin{cases} 0, & 0.0 \le t \le 1.0 \\ Rated, & 1.0 \le t \le 2.0 \\ 0, & 2.0 \le t \le 3.0 \end{cases}.$$

The rotor of the PM brushed DC motor is initially maintained at 180^{o} with no torque load applied. At t = 1.0s, a constant torque load with the rated value is suddenly applied to the rotor shaft. After 1.0 seconds, it is abruptly removed. This study is designed to test the performance of the PID position control scheme, fuzzy logic position control scheme, and nonlinear time-frequency position control scheme when external torque load varies.

Figure 3.78 - Figure 3.80 show the position tracking responses of the PID position control scheme, fuzzy logic position control scheme, and nonlinear time-frequency position control scheme when external torque load varies. Detailed time-domain performance of them are listed in Table 3.21. According to Figure 3.78 - Figure 3.80 and Table 3.21, the position tracking response of the nonlinear time-frequency position control scheme is unmatched by both the PID position control and fuzzy logic position control schemes when external torque load varies. From 0 to 1 seconds, when the external torque

load is zero, the PID position control and fuzzy logic position control keep the rotor position close to the reference value without a large steady state error. However, when the external torque load is suddenly applied to the rotor (1-2 seconds), they both fail to maintain the same performance. The rotor position drops by a large amount and returns to the reference position at an extremely slow speed. Removing the external torque load does not help in recovering their position tracking ability. Based on Figure 3.78 and Figure 3.79, it can be seen that after the external torque load is removed (2-3 seconds), the rotor positions controlled by both the PID position control and fuzzy logic position control jump to a much larger value compared with their rotor positions during 0 to 1 seconds, followed by a slow moving toward the reference position. In contrast, the nonlinear time-frequency position control sees the overshoots caused by suddenly applying or removing the external torque load at a minor 12^{o}, followed by a quick settle-down to the reference position.

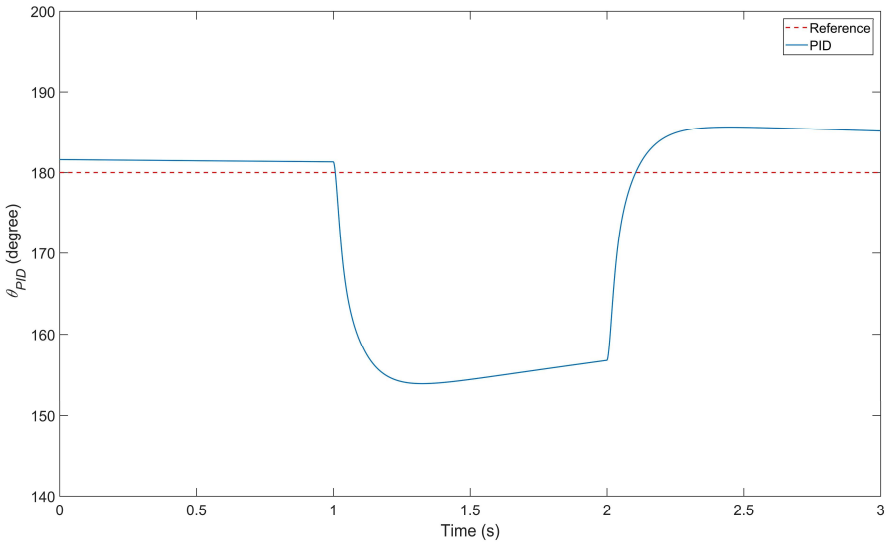

Figure 3.78 Position tracking response of PID position control scheme when external torque load suddenly changes

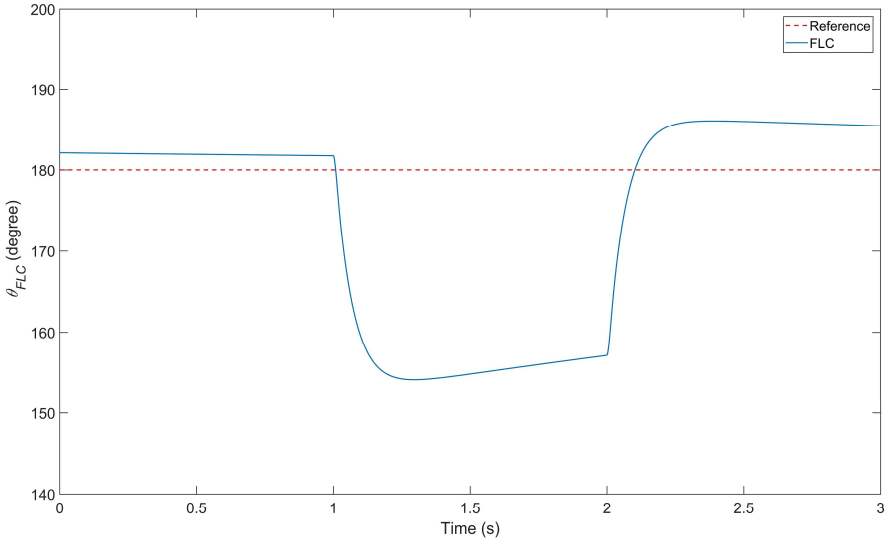

Figure 3.79 Position tracking response of fuzzy logic position control scheme when external torque load suddenly changes

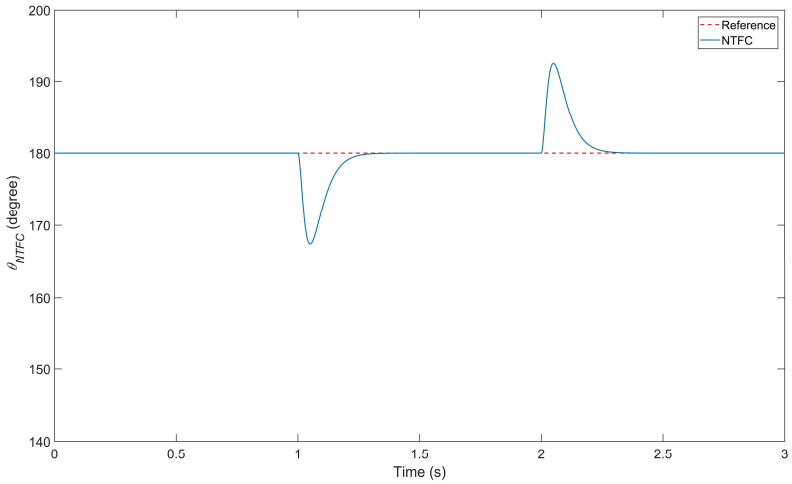

Figure 3.80 Position tracking response of nonlinear time-frequency position control scheme when external torque load suddenly changes

Table 3.21 Comparisons of time-domain performance of the three position control schemes when external torque load suddenly changes

Time (sec)	Time to Settle (sec)			Overshoot (%)		
	PID	FLC	NTFC	PID	FLC	NTFC
1.00 - 2.00	None	None	0.261	14.457	14.371	6.997
2.00 - 3.00	None	None	0.262	3.144	3.367	6.953

Figure 3.81 - Figure 3.83 display the armature control voltage generated by the PID position control scheme, fuzzy logic position control scheme, and nonlinear time-frequency position control scheme, respectively. The corresponding armature currents are demonstrated in Figure 3.84 - Figure 3.86. It can be seen that despite their position tracking responses, the armature voltage and current profiles of the PID position control scheme

and fuzzy logic positon control scheme are better than the nonlinear time-frequency position control scheme. Their armature voltage profiles do not have overshoots and the overshoots in their armature current profiles are also small.

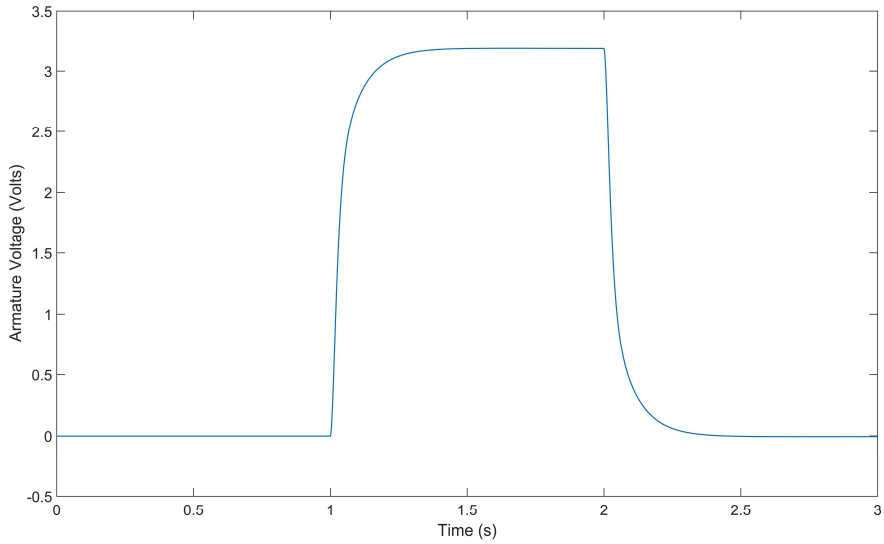

Figure 3.81 Armature control voltage generated by PID position control scheme when external torque load suddenly changes

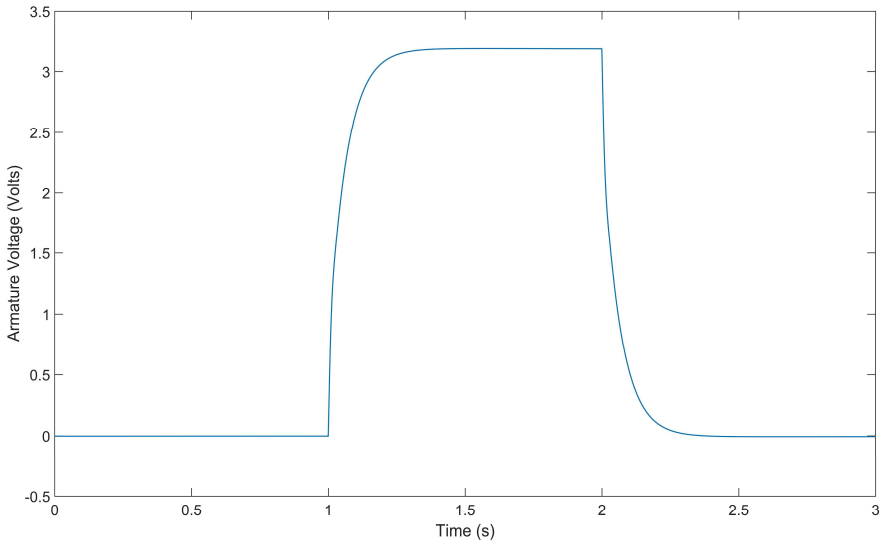

Figure 3.82 Armature control voltage generated by fuzzy logic position control scheme when external torque load suddenly changes

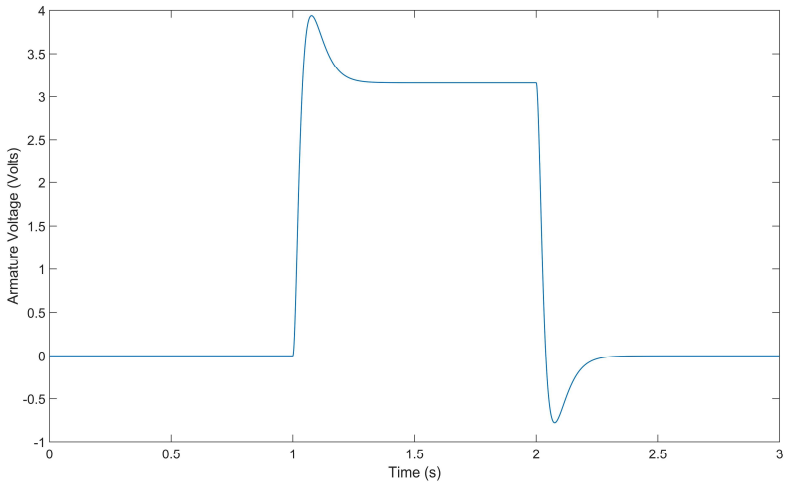

Figure 3.83 Armature control voltage generated by nonlinear time-frequency position control scheme when external torque load suddenly changes

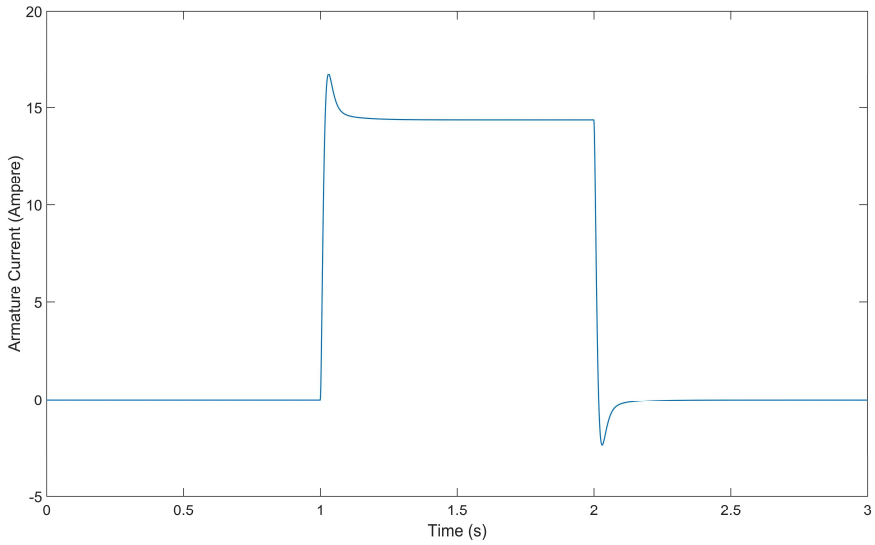

Figure 3.84 Armature current of PID position control scheme when external torque load suddenly changes

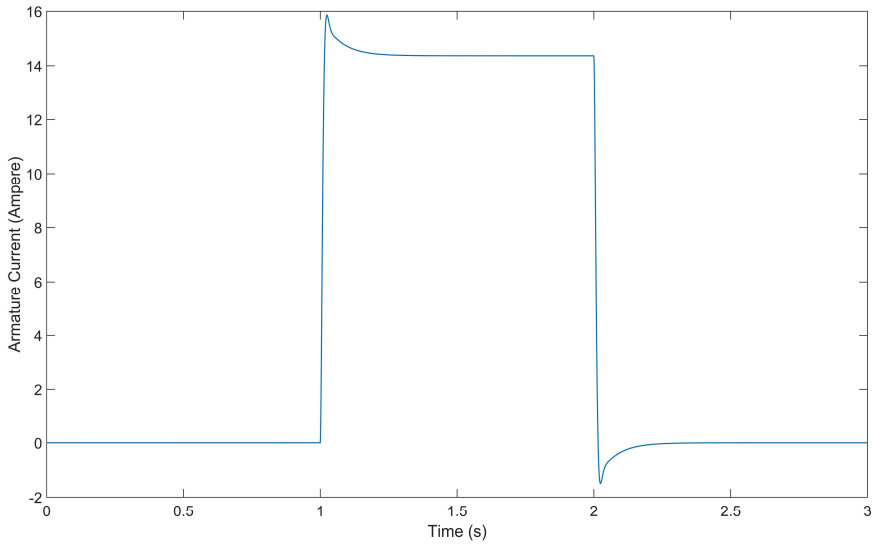

Figure 3.85 Armature current of fuzzy logic position control scheme when external torque load suddenly changes

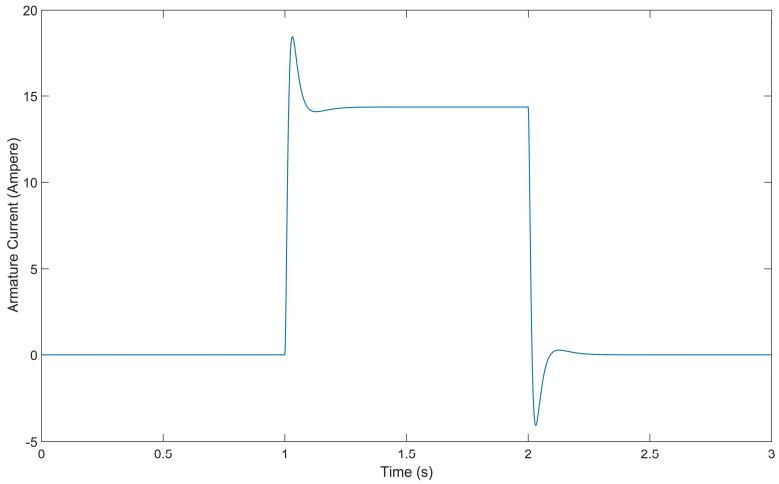

Figure 3.86 Armature current of nonlinear time-frequency position control scheme when external torque load suddenly changes

Table 3.22 Average input power of the motor system with three position control schemes when external torque load suddenly changes

Time (sec)	P_{inavg} (W)		
	PID	FLC	NTFC
0.00 - 1.50	14.702	14.641	15.434

Table 3.22 lists the corresponding P_{inavg} associated with each of the control scheme. Even though the PID position control and fuzzy logic position control both have a lower power consumption than the nonlinear time-frequency position control. They fail to achieve the desired position tracking.

Overall, compared with the PID position control and fuzzy logic position control, the nonlinear time-frequency position control is faster, more accurate, and robust when external torque load suddenly changes.

To further assess the robustness of the nonlinear time-frequency position control scheme when external torque load varies, the two sensor noises depicted in Figure 3.21 and Figure 3.73 are once again considered. Figure 3.87 and Table 3.23 show the position tracking response and time domain performance of the nonlinear time-frequency position control scheme under sudden torque load changes and noise. Comparing them with Figure 3.80 and Table 3.21 where the effect of sensor noise is omitted, the performance of the nonlinear time-frequency position control scheme is nearly unaffected, hence indicating robustness to noise.

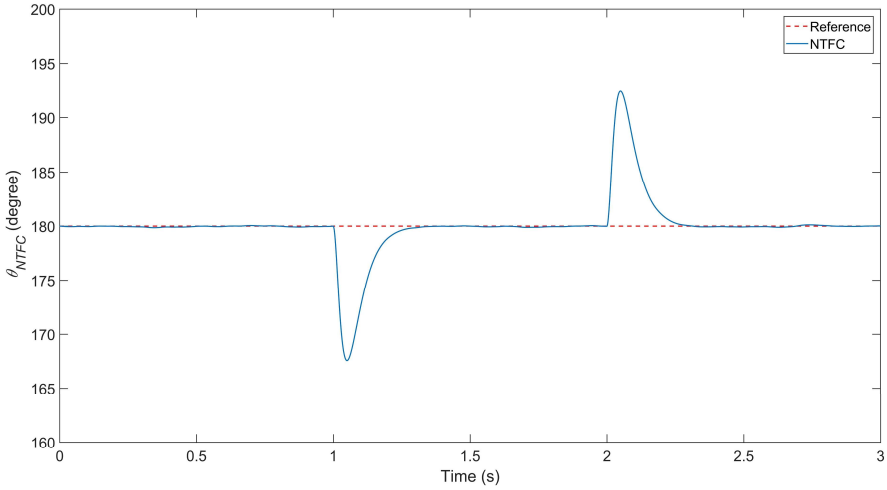

Figure 3.87 Position tracking response of nonlinear time-frequency position control scheme when external torque load suddenly changes and sensor noise is introduced

Table 3.23 Time-domain performance of the nonlinear time-frequency position control scheme when external torque load suddenly changes and sensor noise is introduced.

Time (sec)	Time to Settle (sec)	Overshoot (%)
1.00 - 2.00	0.270	6.905
2.00 - 3.00	0.254	6.894

Figure 3.88 and Figure 3.89 show the corresponding armature control voltage and armature current of the motor system. The frequency spectrum of the armature current and comparison of the average input power of the motor system without and with sensor noises are also displayed in Figure 3.90 and Table 3.24. Clearly, as in the evaluation of the nonlinear time-frequency position control scheme when reference position changes and sensor noises were introduced, the nonlinear time-frequency positon control scheme is fast, accurate, robust to sudden external torque load changes and noise. Most importantly, it is able to control motor response in both the time and frequency domains.

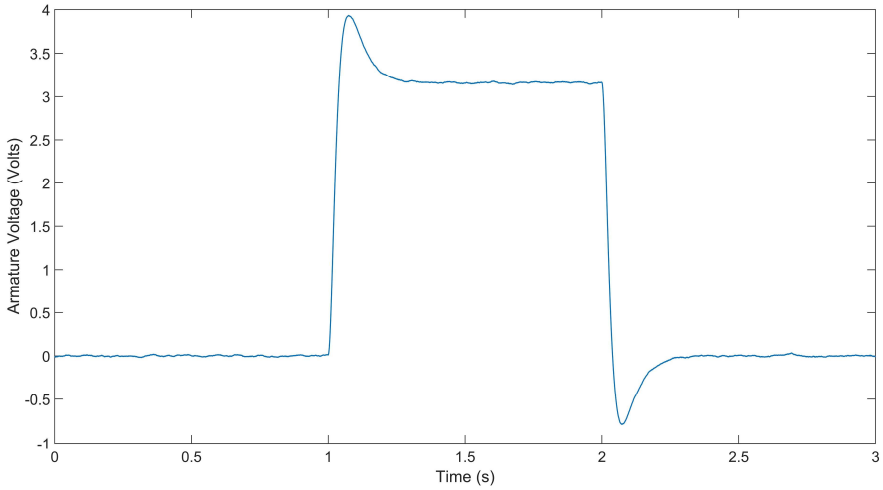

Figure 3.88 Armature control voltage generated by nonlinear time-frequency position control scheme when external torque load suddenly changes and sensor noise is introduced

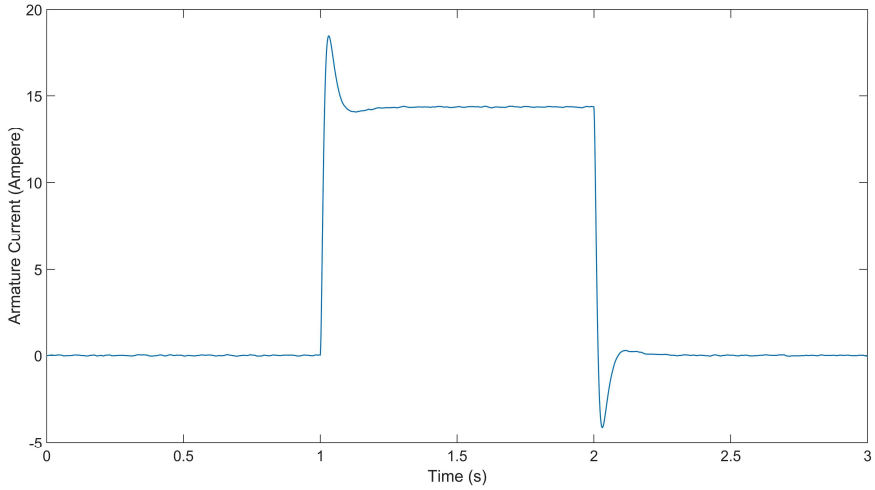

Figure 3.89 Armature current of nonlinear time-frequency position control scheme when external torque load suddenly changes and sensor noise is introduced

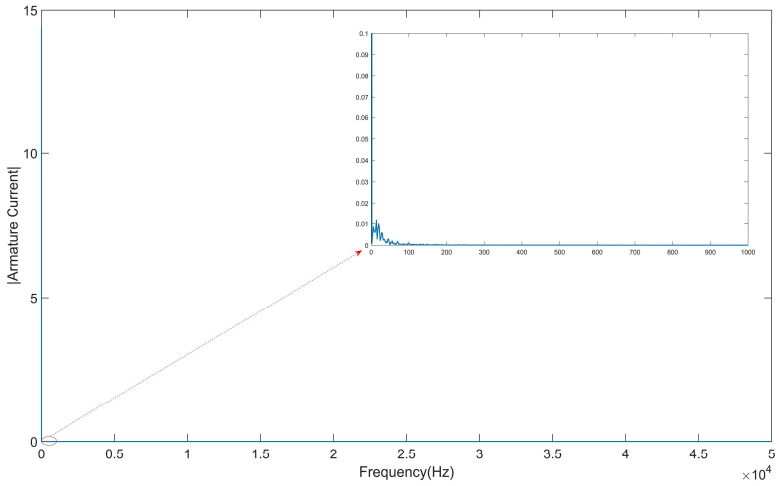

Figure 3.90 Armature current spectrum of nonlinear time-frequency position control scheme when external torque load suddenly changes and sensor noise is introduced

Table 3.24 Comparison of the average input power of the motor system with nonlinear time-frequency position control scheme when external torque load suddenly changes

Time (sec)	P_{inavg} (W)	
	Without noise	With noise
0.00 - 3.00	15.434	15.432

3.5 Summary

In this section, a novel nonlinear time-frequency speed control scheme feasible for the precise and robust speed control of PM brushed DC motors was presented. Its tracking performance was evaluated against the popular PID speed control scheme and fuzzy logic speed control scheme. The results showed that the designed nonlinear time-frequency speed control scheme had several distinctive qualities including high control precision,

fast response, robust to broad bandwidth system uncertainty and non-stationary disturbance, low switching burden for the associated power electronics, energy efficient, and most importantly, capable of mitigating the deterioration of system response in both the time and frequency domains.

Through incorporating a simple proportional controller and an extra position sensor, the nonlinear time-frequency speed control scheme was transformed into a nonlinear time-frequency position control scheme without resetting any parameter of the speed control scheme. Simulation results demonstrated that this nonlinear time-frequency position control scheme possessed the same advantages as the nonlinear time-frequency speed control scheme by comparing its performance with the PID position control and fuzzy logic position control. This necessarily implies that precision speed and position tracking of PM brushed DC motors can be concurrently realized using the nonlinear time-frequency control scheme.

4. NONLINEAR TIME-FREQUENCY CONTROL OF PM SYNCHRONOUS MOTORS*

4.1 Introduction

PM synchronous motors, named after the permanent magnets rather than the electromagnets mounted on the rotor shaft, are popular AC synchronous machines. Differing from AC asynchronous machines where rotor's magnetic field always lags behind the varying magnetic field of the stator windings due to armature reaction, the electromagnetic torque generated in PM synchronous motors by the stator's magnetic field imposes directly on the static magnetic field induced by the rotor magnets, thus causing the rotor to spin synchronously with the varying stator magnetic field. This distinguished feature renders PM synchronous motors many advantages including low inertia, compact size, strong air-gap flux, and high efficiency.

Nowadays, with the rapid development of modern power electronics and the appearance of high intensity permanent magnet materials, PM synchronous motors become increasingly popular in industrial applications. PM synchronous motor is intrinsically a nonlinear, multivariable, and highly coupled system. In order for it to achieve satisfactory dynamic performance, proper control algorithms are essential.

*Part of this section is reprinted with permission from "Time-frequency based field oriented control of permanent magnet synchronous motors" by Wang X, Suh CS, 2017, Int J Dyn Control, doi: 10.1007/s40435-017-0327-5, Copyright 2017 by Springer

Numerous methods have been devised for the control of PM synchronous motors, with the most widely accepted one being the FOC scheme. In this scheme, the stator phase winding parameters are transformed from a three-phase static reference frame into a two-axis rotating reference frame which rotates synchronously with the rotor. Such a coordinate transformation not only eliminates the sinusoidal changing property of stator parameters, but also expresses the motor model in a mutually decoupled two-axis reference frame (*d*-*q* reference frame). By controlling the stator current components along each axis individually, proper control of PM synchronous motors can be achieved. The basic concept of FOC is based on three PI controllers that controls the *d*-axis current, rotor speed, and *q*-axis current, respectively. The two PI controllers controlling the rotor speed and *q*-axis current are cascaded. Since the electrical inertia of the two current loops are much smaller than the mechanical inertia of the speed loop, the two current loops in FOC runs much faster than the speed loop [20].

Being both simplistic and reliable are the noted benefits of PI control based FOC. However, the scheme is also considered unfavorable as being difficult to fine-tune and hard to optimize the overall performance [23]. Revisions of FOC have since been considered to address these issues as reviewed in section 1.1.

In this section, a nonlinear time-frequency control concept based FOC scheme is developed for the fast, precise, and robust control of PM synchronous motors. The major advantage of nonlinear time-frequency control is its ability in applying control effort using both the time and frequency information, thus rendering it feasible for complex nonlinear systems.

The new field oriented speed control scheme presented in the followings consists of one PI controller and one nonlinear time-frequency controller. The PI controller is used for *d*-axis current control in a way not unlike the basic FOC notion. The nonlinear time-frequency controller illustrated in section 2.4 is introduced to replace the two PI controllers used for speed and *q*-axis current control in classical FOC. This elimination of the cascaded controller structure not only facilitates controller tuning, but increases system stability as well.

4.2 Mathematical Model of Three-Phase PM Synchronous Motors

The mathematical model of a three-phase PM synchronous motor is developed in the stationary *abc* reference frame based on the following assumptions:

1. There is no damper winding in the rotor core.
2. The induced back EMF in stator phase windings is sinusoidal.
3. Eddy currents, hysteresis losses, and air-gap space harmonics are negligible.
4. The motor is operated on balanced mode.
5. The motor system is electrically linear.
6. The phase sequence is $a \rightarrow b \rightarrow c$ counterclockwise.

Figure 4.1 illustrates a cross-sectional schematic of an elementary two-pole, three-phase, wye-connected PM synchronous motor in the classical *abc* reference frame [19].

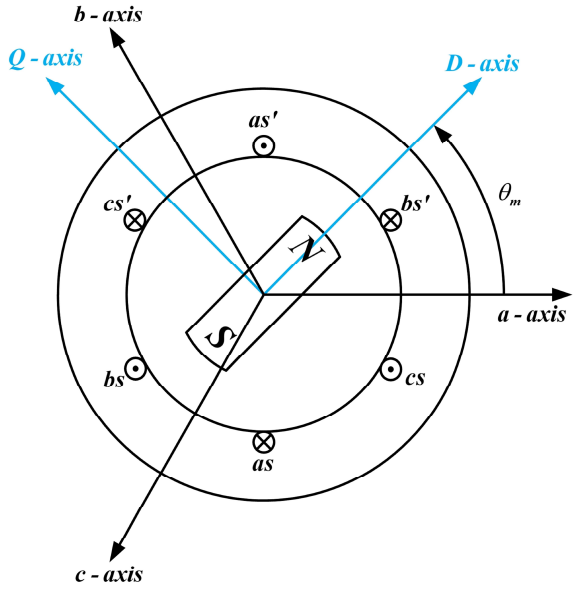

Figure 4.1 Cross-sectional schematic of a two-pole, three-phase PM synchronous motor

The stator phase windings (*as*-*as*', *bs*-*bs*', and *cs*-*cs*') of the motor are embedded in the slots around the inside circumference of the stator. Each phase winding is displaced by 120 degrees with respect to each other. The stationary *a*-axis, *b*-axis, and *c*-axis represent the positive direction of the magnetic flux produced by the stator *a*-phase winding, *b*-phase winding, and *c*-phase winding, respectively. The rotating *D*-axis and *Q*-axis denote the positive direction of the direct component (north pole) and quadrature component of the rotor magnetic flux. The angle of the *D*-axis with respect to the *a*-axis is defined as θ_m - the mechanical position of the rotor shaft (generally obtained from encoders or position sensors mounted on the rotor shaft). When the rotor shaft rotates 360 mechanical degrees, the rotor returns to the same location as where it started. Figure 4.2 shows the schematic of the stator phase windings of the PM synchronous motor displayed

in Figure 4.1 where N_{as}, N_{bs}, and N_{cs} are the number of turns of each stator phase winding; R_{as}, R_{bs}, and R_{cs} are the equivalent stator phase winding resistance; and i_{as}, i_{bs}, and i_{cs} are the instantaneous current flow through each stator phase winding.

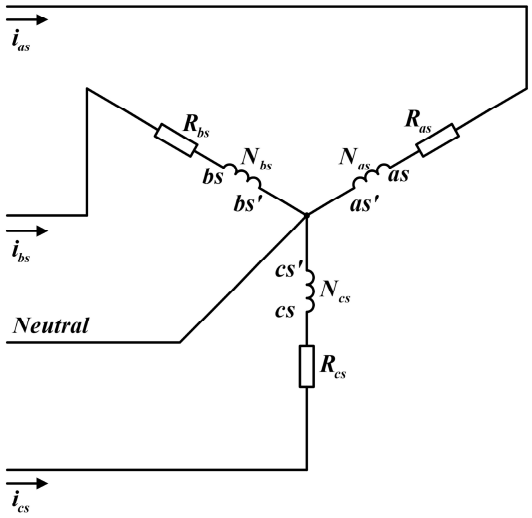

Figure 4.2 Schematic of the stator phase windings of a two-pole, three-phase PM synchronous motor

To derive the electrical governing equations of the stator, a circuit model [59] of the stator phase windings is considered in Figure 4.3.

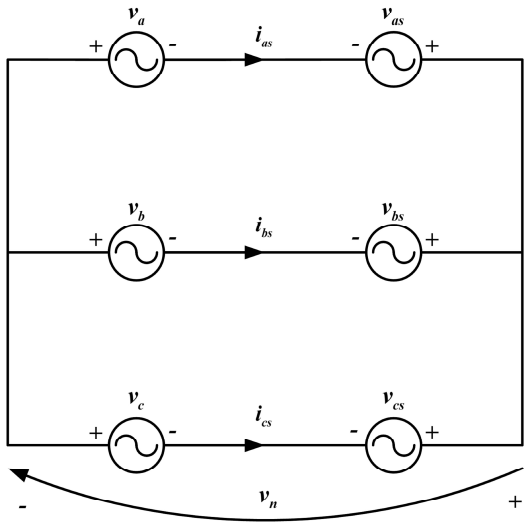

Figure 4.3 Circuit representation of the stator phase windings of a two-pole, three-phase PM synchronous motor

The voltage equations that govern the circuit model are

$$\begin{cases} v_{as} = v_n + v_a \\ v_{bs} = v_n + v_b \\ v_{cs} = v_n + v_c \end{cases} \tag{4.1}$$

where v_a, v_b, and v_c are the input voltages that supply each stator phase winding; v_{as}, v_{bs}, and v_{cs} are the voltages across each stator phase winding, and v_n is the voltage at the neutral point.

For a motor operating in balanced mode, all phase windings have the same resistance (i.e., $R_{as} = R_{bs} = R_{cs} = R_s$) and the same number of turns (i.e., $N_{as} = N_{bs} = N_{cs} = N_s$). Consequently, there are no net current flowing in the neutral point and hence $v_n = 0$.

The electrical dynamic equations of v_{as}, v_{bs}, and v_{cs} are

$$\begin{bmatrix} v_{as} \\ v_{bs} \\ v_{cs} \end{bmatrix} = \begin{bmatrix} R_s & 0 & 0 \\ 0 & R_s & 0 \\ 0 & 0 & R_s \end{bmatrix} \begin{bmatrix} i_{as} \\ i_{bs} \\ i_{cs} \end{bmatrix} + \frac{d}{dt} \begin{bmatrix} \lambda_{as} \\ \lambda_{bs} \\ \lambda_{cs} \end{bmatrix} \tag{4.2}$$

where λ_{as}, λ_{bs}, and λ_{cs} are the flux linkages of each stator phase winding as follows

$$\begin{bmatrix} \lambda_{as} \\ \lambda_{bs} \\ \lambda_{cs} \end{bmatrix} = \begin{bmatrix} L_{asas} & L_{asbs} & L_{ascs} \\ L_{bsas} & L_{bsbs} & L_{bscs} \\ L_{csas} & L_{csbs} & L_{cscs} \end{bmatrix} \begin{bmatrix} i_{as} \\ i_{bs} \\ i_{cs} \end{bmatrix} + \begin{bmatrix} \lambda_{asmr} \\ \lambda_{bsmr} \\ \lambda_{csmr} \end{bmatrix} \tag{4.3}$$

with L_{asas}, L_{bsbs}, and L_{cscs} being the self-inductances of the stator *a*-phase winding, *b*-phase winding, and *c*-phase winding, respectively; $L_{asbs} = L_{bsas}$, $L_{bscs} = L_{csbs}$, and $L_{csas} = L_{ascs}$ being the mutual-inductances between stator *a*- and *b*-phase windings, *b*- and *c*-phase windings, and *c*- and *a*-phase windings, respectively; and λ_{asmr}, λ_{bsmr}, and λ_{csmr} being the flux linkages established by the permanent magnets mounted on the rotor as viewed by the stator *a*-phase winding, *b*-phase winding, and *c*-phase winding, respectively.

For an electrically linear motor system, stator winding inductances are functions of rotor position only. Their mathematical representations are

$$\begin{cases} L_{asas} = L_{os} + L_{ls} - L_{xs}cos2\theta_m \\ L_{bsbs} = L_{os} + L_{ls} - L_{xs}cos2\left(\theta_m - \dfrac{2\pi}{3}\right) \\ L_{cscs} = L_{os} + L_{ls} - L_{xs}cos2\left(\theta_m + \dfrac{2\pi}{3}\right) \\ L_{asbs} = L_{bsas} = -\dfrac{1}{2}L_{os} - L_{xs}cos2\left(\theta_m - \dfrac{\pi}{3}\right) \\ L_{bscs} = L_{csbs} = -\dfrac{1}{2}L_{os} - L_{xs}cos2\theta_m \\ L_{csas} = L_{ascs} = -\dfrac{1}{2}L_{os} - L_{xs}cos2\left(\theta_m + \dfrac{\pi}{3}\right) \end{cases} \tag{4.4}$$

where L_{os} is the inductance due to air gap flux; L_{ls} is the leakage inductance; and L_{xs} is the inductance fluctuation due to motor saliency.

With regard to λ_{asmr}, λ_{bsmr}, and λ_{csmr}, these three variables would successively reach their maximum values when the rotor *D*-axis is aligned with the *a*-axis, *b*-axis, and *c*-axis, respectively. This relationship can be represented as

$$\begin{bmatrix} \lambda_{asmr} \\ \lambda_{bsmr} \\ \lambda_{csmr} \end{bmatrix} = K_E \begin{bmatrix} cos(\theta_m) \\ cos(\theta_m - \dfrac{2\pi}{3}) \\ cos(\theta_m + \dfrac{2\pi}{3}) \end{bmatrix} \tag{4.5}$$

Their time derivatives, the open-circuit voltages (back EMF) induced in the corresponding stator phase windings when the rotor rotates, are given by

$$\begin{bmatrix} \frac{d\lambda_{asmr}}{dt} \\ \frac{d\lambda_{bsmr}}{dt} \\ \frac{d\lambda_{csmr}}{dt} \end{bmatrix} = \begin{bmatrix} e_{as} \\ e_{bs} \\ e_{cs} \end{bmatrix} = -K_E \begin{bmatrix} sin(\theta_m) \\ sin(\theta_m - \frac{2}{3}\pi) \\ sin(\theta_m + \frac{2}{3}\pi) \end{bmatrix} \frac{d\theta_m}{dt} \tag{4.6}$$

where e_{as}, e_{bs}, and e_{cs} represent the back EMF of the stator *a*-phase, *b*-phase and *c*-phase winding coil, respectively; K_E is the peak amplitude of $\lambda_{asmr} / \lambda_{bsmr} / \lambda_{csmr}$ and is often referred to as the back EMF constant. It is noted that although derived for a two-pole, three-phase PM synchronous motor, Equations (4.1) to (4.6) are equally applicable to three-phase PM synchronous motors with multiple poles.

Figure 4.4 shows the schematic of a four-pole, three-phase, wye-connected PM synchronous motor in the *abc* reference frame where each stator phase winding now consists of two series connected windings ($as_1 - as'_1 - as_2 - as'_2$, $bs_1 - bs'_1 - bs_2 - bs'_2$, and $cs_1 - cs'_1 - cs_2 - cs'_2$). Each series has the same number of turns and is displaced by 60 mechanical degrees from each other. One of the north poles of the rotor is defined as the *D*-axis and the *Q*-axis is leading the *D*-axis by 45 mechanical degrees.

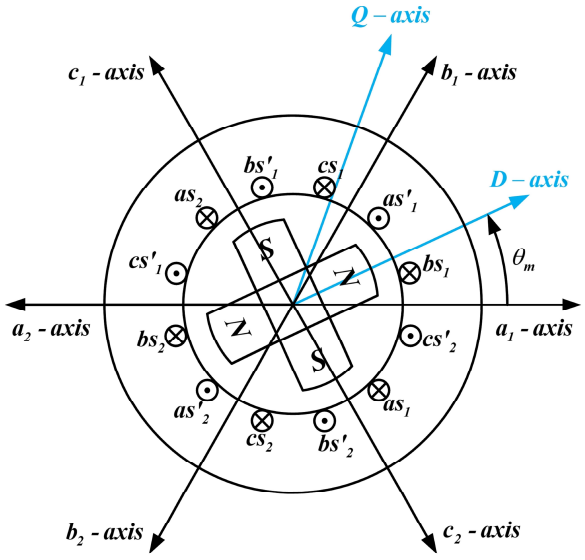

Figure 4.4 Schematic of a four-pole, three-phase PM synchronous motor

The corresponding schematic of stator phase windings of this four-pole motor is given in Figure 4.5. It is evident that Equations (4.1) to (4.3) are still valid for this four-pole, three-phase motor. Indeed they are valid for three-phase PM synchronous motors with any number of poles.

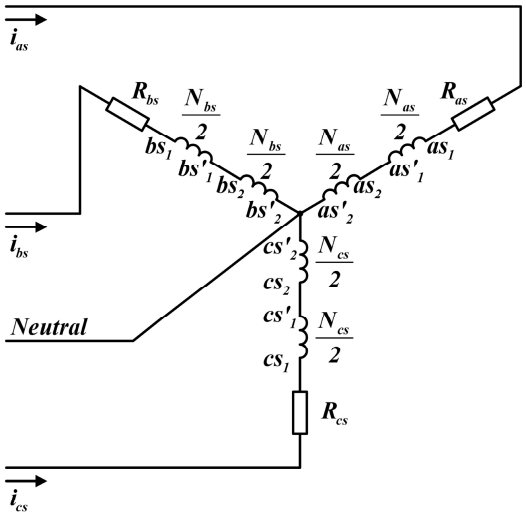

Figure 4.5 Schematic of stator phase windings of a four-pole, three-phase PM synchronous motor

Equations (4.4) to (4.6), however, are no longer applicable to this particular four-pole machine. For the stator phase winding arrangement in Figure 4.4, the rotor shaft now only needs to move 180 mechanical degrees to obtain an identical magnetic configuration as when it started. Whereas in a two-pole PM synchronous motor, this takes 360 mechanical degrees. Specifically, when the rotor shaft of the four-pole motor rotates counterclockwise from $\theta_m = 0°$ to $\theta_m = 180°$, λ_{asmr}, λ_{bsmr}, and λ_{csmr} would successively reach their maximum values when the rotor *D*-axis is aligned with the a_1- axis, b_1- axis, and c_1 - axis, respectively. And, if the rotor shaft keeps on rotating from $\theta_m = 180°$ to $\theta_m = 360°$, these three variables would demonstrate exactly the same waveforms and successively reach their maximum values again when the rotor *D*-axis is aligned with a_2-

axis, b_2 - axis, and c_2 - axis, respectively. That is, the period of λ_{asmr}, λ_{bsmr}, and λ_{csmr} has changed from 360 mechanical degrees in a two-pole PM synchronous motor to 180 mechanical degrees in a four-pole PM synchronous motor. Motor inductance and back EMFs require similar modifications. Therefore, specific accommodation is needed to apply Equations (4.4) to (4.6) to a *P*-pole machine.

In PM synchronous motors, the stator phase windings are so arranged that with balanced steady-state currents flowing in the windings, a magnetic flux is generated which rotates about the air gap as a set of magnetic poles at an angular velocity corresponding to the frequency of the stator voltages/currents and number of poles. This relationship can be represented as

$$\omega_e = \frac{P}{2}\omega_m \tag{4.7}$$

where

$$\omega_e = \frac{d\theta_e}{dt} \tag{4.8}$$

is the frequency (electrical speed) of the stator voltages/currents across the stator phase windings; θ_e is the electrical position of the rotor; P is the number of poles; and

$$\omega_m = \frac{d\theta_m}{dt} \tag{4.9}$$

is the angular speed of the rotor shaft. Equation (4.7) is equivalent to

$$\theta_e = \frac{P}{2}\theta_m \tag{4.10}$$

which defines the relationship between the mechanical position and electrical position of the rotor shaft. Equation (4.10) dictates that, for any *P*-pole, three-phase PM synchronous motor, each stator phase winding series is always separated by 120 electrical degrees and the rotor *Q*-axis always leads the *D*-axis by 90 electrical degrees, regardless of how they are physically separated in space.

When all the stator phase winding inductances and flux linkages due to permanent magnets on the rotor of a *P*-pole, three-phase PM synchronous motor are evaluated, it can be shown that Equations (4.4) to (4.6) of a two-pole, three-phase machine is applicable to a *P*-pole, three-phase motor as long as θ_m in these equations is replaced with θ_e as defined in Equation (4.10). In other words, any *P*-pole, three-phase motor can be treated as a two-pole, three-phase motor if the aforementioned substitution is made.

The power carried by the coupling field of a *P*-pole, three-phase motor can be expressed as

$$P_c = P_e + P_L \tag{4.11}$$

where

$$P_e = \begin{bmatrix} e_{as} & e_{bs} & e_{cs} \end{bmatrix} \begin{bmatrix} i_{as} \\ i_{bs} \\ i_{cs} \end{bmatrix} \tag{4.12}$$

is the power due to the induced back-EMF;

$$P_L = \frac{1}{2}\frac{d}{dt}\left(\begin{bmatrix} i_{as} & i_{bs} & i_{cs} \end{bmatrix} \begin{bmatrix} L'_{asas} & L_{asbs} & L_{csas} \\ L_{asbs} & L'_{bsbs} & L_{bscs} \\ L_{csas} & L_{bscs} & L'_{cscs} \end{bmatrix} \begin{bmatrix} i_{as} \\ i_{bs} \\ i_{cs} \end{bmatrix} \right) \tag{4.13}$$

is the power of the stator phase winding coils due to coil inductances; and

$$\begin{bmatrix} L'_{asas} \\ L'_{bsbs} \\ L'_{cscs} \end{bmatrix} = L_{os} \begin{bmatrix} 1 \\ 1 \\ 1 \end{bmatrix} - L_{xs} \begin{bmatrix} \cos 2\theta_e \\ \cos 2(\theta_e - \frac{2\pi}{3}) \\ \cos 2(\theta_e + \frac{2\pi}{3}) \end{bmatrix} \tag{4.14}$$

are, respectively, the self-inductances of the stator *a*-phase winding, *b*-phase winding, and *c*-phase winding without leakage inductance.

Consider $\begin{bmatrix} i_{as} & i_{bs} & i_{cs} \end{bmatrix}^T$ and θ_m as independent variables, the electromagnetic torque (T_{out}) generated by the PM synchronous motor is

$$\begin{aligned} T_{out} &= \frac{\partial}{\partial \theta_m} \left\{ \int P_c dt \right\} \\ &= \frac{\partial}{\partial \theta_m} \left\{ \frac{1}{2} \left[\boldsymbol{I_s} \right]^T \left[\boldsymbol{L'_{ss}} \right] \left[\boldsymbol{I_s} \right] + \left[\boldsymbol{\Lambda_{smr}} \right]^T \left[\boldsymbol{I_s} \right] \right\} \\ &= \frac{P}{2} \{ L_{xs} (i_{as}^2 - 0.5 i_{bs}^2 - 0.5 i_{cs}^2 - i_{as} i_{bs} + 2 i_{bs} i_{cs} - i_{cs} i_{as}) sin(2\theta_e) \\ &\qquad + \frac{\sqrt{3}}{2} L_{xs} (i_{bs}^2 - i_{cs}^2 - 2 i_{as} i_{bs} + 2 i_{cs} i_{as}) cos(2\theta_e) \\ &\qquad - K_E [sin(\theta_e) i_{as} + sin(\theta_e - \frac{2\pi}{3}) i_{bs} + sin(\theta_e + \frac{2\pi}{3}) i_{cs}] \} \end{aligned} \tag{4.15}$$

where $\left[\boldsymbol{I_s} \right]$ represents $\begin{bmatrix} i_{as} & i_{bs} & i_{cs} \end{bmatrix}^T$; $\left[\boldsymbol{\Lambda_{smr}} \right]$ represents $\begin{bmatrix} \lambda_{asmr} & \lambda_{bsmr} & \lambda_{csmr} \end{bmatrix}^T$; and $\left[\boldsymbol{L'_{ss}} \right]$ represent the inductance matrix shown in Equation (4.13).

Equation (4.15) has two distinct terms, with the first term corresponding to the 'reluctance torque' and related to motor saliency and the second term corresponding to the 'excitation torque' and related to the induced back-EMF. For a motor without saliency,

L_{xs} equals to zero and the output torque is related to the induced back-EMF in three stator phase windings solely.

Figure 4.6 shows schematically the mechanical output system of a PM synchronous motor of the following expression

$$T_{out} = J\frac{d\omega_m}{dt} + B\omega_m + T_L \tag{4.16}$$

where J is the moments of inertia of the rotor shaft, B is the viscous damping coefficient, and T_L is the external torque load.

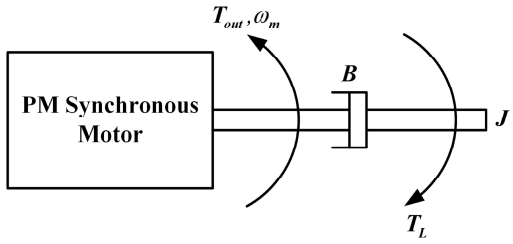

Figure 4.6 Schematic of the mechanical output system of a PM synchronous motor

Combing Equations (4.1) - (4.16), a comprehensive model for the *P*-pole, three-phase, wye-connected PM synchronous motor under stationary *abc* reference frame is resulted

$$
\begin{cases}
\dfrac{d}{dt}\left[L_{asas}i_{as}+L_{asbs}i_{bs}+L_{csas}i_{cs}\right]=-R_s i_{as}+\dfrac{P}{2}K_E\sin\left(\theta_e\right)\omega_m+v_{as} \\
\dfrac{d}{dt}\left[L_{asbs}i_{as}+L_{bsbs}i_{bs}+L_{bscs}i_{cs}\right]=-R_s i_{bs}+\dfrac{P}{2}K_E\sin\left(\theta_e-\dfrac{2\pi}{3}\right)\omega_m+v_{bs} \\
\dfrac{d}{dt}\left[L_{csas}i_{as}+L_{bscs}i_{bs}+L_{cscs}i_{cs}\right]=-R_s i_{cs}+\dfrac{P}{2}K_E\sin\left(\theta_e+\dfrac{2\pi}{3}\right)\omega_m+v_{cs} \\
\dfrac{d\omega_m}{dt}=\dfrac{1}{J}\{T_{out}-B\omega_m-T_L\} \\
\dfrac{d\theta_e}{dt}=\dfrac{P}{2}\omega_m
\end{cases}
\tag{4.17}
$$

The PM synchronous motor model is highly coupled. The induced back-EMF in each stator phase winding coil is determined by the mechanical rotation of the rotor magnets. The mechanical rotation of the rotor shaft is governed by the frequency of voltages/currents supplied to the stator phase windings. The generated electromagnetic torque T_{out} depends on motor saliency, induced back-EMFs and stator phase winding currents. To make things even worse, the majority of the electrical quantities (voltages, currents, and back-EMF) found in the model is time-variant. The complexity, together with the presence of external torque load and disturbances, is the reason for PM synchronous motors to display strong nonlinearity - an unacceptable trait in practical applications as it not only degrades motor performance, but increases power consumption as well. Proper mitigation of the nonlinearity is therefore of paramount significance.

4.3 Field Oriented Control of PM Synchronous Motors

Motion control is difficult under the classical *abc* reference frame, not only because PM synchronous motors are extremely complex and highly coupled, but also because most classical controllers have difficulty in controlling input voltages with

sinusoidal references [60]. However, by using FOC, all the downsides identified earlier can be addressed to realize improved overall performance. The first step to implement FOC is transforming the stator phase winding variables to a two-phase coordinate system which rotates at the same electrical speed along with the rotor shaft. This three-phase to two-phase transformation, known as the Park's Transformation, for a balanced system is of the form

$$\begin{bmatrix} f_d \\ f_q \end{bmatrix} = \left[\boldsymbol{T}_{abc\text{-}dq} \right] \begin{bmatrix} f_a \\ f_b \\ f_c \end{bmatrix} \tag{4.18}$$

where $\begin{bmatrix} f_a & f_b & f_c \end{bmatrix}^T$ can be voltages/currents/flux linkages under the three-phase stator stationary reference frame; $\begin{bmatrix} f_d & f_q \end{bmatrix}^T$ is the *d*-axis component, and *q*-axis component under the two-phase stator rotating reference frame, respectively; $\left[\boldsymbol{T}_{abc\text{-}dq} \right]$ is the transformation matrix, which is not unique and depends on the reference axis and phase sequence.

For the reference axis and phase sequence shown in Figure 4.1 and Figure 4.4, where all the three phases are separated by 120 electrical degrees and the *c*-phase leads the *b*-phase which in turns leads the *a*-phase, $\left[\boldsymbol{T}_{abc\text{-}dq} \right]$ equals to

$$[\boldsymbol{T}_{abc\text{-}dq}] = K_1 \begin{bmatrix} \cos(\theta_e) & \cos(\theta_e - \frac{2\pi}{3}) & \cos(\theta_e + \frac{2\pi}{3}) \\ -\sin(\theta_e) & -\sin(\theta_e - \frac{2\pi}{3}) & -\sin(\theta_e + \frac{2\pi}{3}) \end{bmatrix} \tag{4.19}$$

The inverse of $\left[\boldsymbol{T}_{dq\text{-}abc} \right]$ is

$$[\boldsymbol{T}_{dq\text{-}abc}] = K_2 \begin{bmatrix} \cos(\theta_e) & -\sin(\theta_e) \\ \cos(\theta_e - \frac{2\pi}{3}) & -\sin(\theta_e - \frac{2\pi}{3}) \\ \cos(\theta_e + \frac{2\pi}{3}) & -\sin(\theta_e + \frac{2\pi}{3}) \end{bmatrix} \tag{4.20}$$

where K_1 and K_2 are constants selected from Table 4.1.

Figure 4.7 further illustrates this transformation by showing the original three phase quantities under the stator stationary reference frame, the transformed *d*- and *q*-axis components under the stator rotating reference frame, and the alignment of the stator and rotor rotating reference frames.

Table 4.1 Common values for K_1 and K_2

Symbol	Magnitude Invariant	Power Invariant
K_1	$\frac{2}{3}$	$\sqrt{\frac{2}{3}}$
K_2	1	$\sqrt{\frac{2}{3}}$

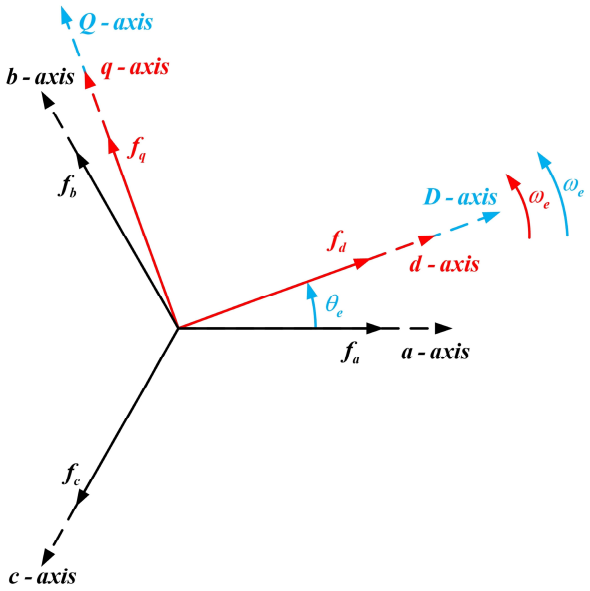

Figure 4.7 Illustration of Park's Transformation

Applying the Park's Transformation to the developed three phase PM synchronous motor model under the *abc* reference frame, the transformed stator phase winding voltages and currents are:

$$\begin{bmatrix} v_{ds} \\ v_{qs} \end{bmatrix} = \begin{bmatrix} \boldsymbol{T}_{abc\text{-}dq} \end{bmatrix} \begin{bmatrix} v_{as} \\ v_{bs} \\ v_{cs} \end{bmatrix} \tag{4.21}$$

$$\begin{bmatrix} i_{ds} \\ i_{qs} \end{bmatrix} = \begin{bmatrix} \boldsymbol{T}_{abc\text{-}dq} \end{bmatrix} \begin{bmatrix} i_{as} \\ i_{bs} \\ i_{cs} \end{bmatrix} \tag{4.22}$$

where v_{ds} and v_{qs} are *d*-axis and *q*-axis voltages, respectively; i_{ds} and i_{qs} are *d*-axis and *q*-axis currents, respectively. The transformed flux linkages are

$$\begin{aligned}\begin{bmatrix}\lambda_{ds}\\ \lambda_{qs}\end{bmatrix} &= \left[\boldsymbol{T}_{\boldsymbol{abc\text{-}dq}}\right]\left[\boldsymbol{\Lambda}_{\boldsymbol{s}}\right] \\ &= \left[\boldsymbol{T}_{\boldsymbol{abc\text{-}dq}}\right]\left[\boldsymbol{L}_{\boldsymbol{ss}}\right]\left[\boldsymbol{T}_{\boldsymbol{dq\text{-}abc}}\right]\left[\boldsymbol{I}_{\boldsymbol{dqs}}\right] + \left[\boldsymbol{T}_{\boldsymbol{abc\text{-}dq}}\right]\left[\boldsymbol{\Lambda}_{\boldsymbol{smr}}\right] \\ &= \begin{bmatrix}L_{ds} & 0\\ 0 & L_{qs}\end{bmatrix}\begin{bmatrix}i_{ds}\\ i_{qs}\end{bmatrix} + \begin{bmatrix}\lambda_{mr}\\ 0\end{bmatrix}\end{aligned} \tag{4.23}$$

where λ_{ds} and λ_{qs} are *d*-axis and *q*-axis flux linkages, respectively; $\left[\boldsymbol{\Lambda}_{\boldsymbol{s}}\right]$ represents $\left[\lambda_{as} \quad \lambda_{bs} \quad \lambda_{cs}\right]^T$; $\left[\boldsymbol{L}_{\boldsymbol{ss}}\right]$ represents the inductance matrix shown in Equation (4.3); $\left[\boldsymbol{I}_{\boldsymbol{dqs}}\right]$ represents $\left[i_{ds} \quad i_{qs}\right]^T$;

$$L_{ds} = L_{ls} + \frac{3}{2}(L_{os} - L_{xs}) \tag{4.24}$$

is the *d*-axis synchronous inductance;

$$L_{qs} = L_{ls} + \frac{3}{2}(L_{os} + L_{xs}) \tag{4.25}$$

is the *q*-axis synchronous inductance; and

$$\lambda_{mr} = \frac{3}{2}K_1 K_E \tag{4.26}$$

is the flux linkage due to the permanent magnets mounted on the rotor.

The electrical dynamic equation of the PM synchronous motor in stator rotating reference frame is

$$
\begin{aligned}
\begin{bmatrix} v_{ds} \\ v_{qs} \end{bmatrix} &= \left[\boldsymbol{T}_{\boldsymbol{abc\text{-}dq}}\right]\left[\boldsymbol{V}_{\boldsymbol{s}}\right] \\
&= \left[\boldsymbol{T}_{\boldsymbol{abc\text{-}dq}}\right]\left[\boldsymbol{R}_{\boldsymbol{s}}\right]\left[\boldsymbol{I}_{\boldsymbol{s}}\right] + \left[\boldsymbol{T}_{\boldsymbol{abc\text{-}dq}}\right]\frac{d}{dt}\left[\boldsymbol{\Lambda}_{\boldsymbol{s}}\right] \\
&= \left[\boldsymbol{T}_{\boldsymbol{abc\text{-}dq}}\right]\left[\boldsymbol{R}_{\boldsymbol{s}}\right]\left[\boldsymbol{T}_{\boldsymbol{dq\text{-}abc}}\right]\left[\boldsymbol{I}_{\boldsymbol{dqs}}\right] + \left[\boldsymbol{T}_{\boldsymbol{abc\text{-}dq}}\right]\frac{d}{dt}\left(\left[\boldsymbol{T}_{\boldsymbol{dq\text{-}abc}}\right]\left[\boldsymbol{\Lambda}_{\boldsymbol{dqs}}\right]\right) \\
&= \begin{bmatrix} R_s & 0 \\ 0 & R_s \end{bmatrix}\begin{bmatrix} i_{ds} \\ i_{qs} \end{bmatrix} + \left(\left[\boldsymbol{T}_{\boldsymbol{abc\text{-}dq}}\right]\frac{d}{dt}\left[\boldsymbol{T}_{\boldsymbol{dq\text{-}abc}}\right]\right)\left[\boldsymbol{\Lambda}_{\boldsymbol{dqs}}\right] + \frac{d}{dt}\left[\boldsymbol{\Lambda}_{\boldsymbol{dqs}}\right] \\
&= \begin{bmatrix} R_s & 0 \\ 0 & R_s \end{bmatrix}\begin{bmatrix} i_{ds} \\ i_{qs} \end{bmatrix} + \begin{bmatrix} 0 & -\omega_e \\ \omega_e & 0 \end{bmatrix}\begin{bmatrix} \lambda_{ds} \\ \lambda_{qs} \end{bmatrix} + \frac{d}{dt}\begin{bmatrix} \lambda_{ds} \\ \lambda_{qs} \end{bmatrix}
\end{aligned}
\tag{4.27}
$$

where $\left[\boldsymbol{V}_{\boldsymbol{s}}\right] = \begin{bmatrix} v_{as} & v_{bs} & v_{cs} \end{bmatrix}^T$; $\left[\boldsymbol{R}_{\boldsymbol{s}}\right]$ represents the diagonal resistance matrix appeared in Equation (4.2); and $\left[\boldsymbol{\Lambda}_{\boldsymbol{dqs}}\right] = \begin{bmatrix} \lambda_{ds} & \lambda_{qs} \end{bmatrix}^T$.

Applying the Park's transformation to Equation (4.15), the electromagnetic torque of a *P*-pole, three-phase PM synchronous motor becomes

$$
\begin{aligned}
T_{out} &= \frac{\partial}{\partial \theta_m}\left\{\int P_c dt\right\} \\
&= \frac{\partial}{\partial \theta_m}\left\{\frac{1}{2}\left[\boldsymbol{I}_{\boldsymbol{s}}\right]^T\left[\boldsymbol{L}'_{\boldsymbol{ss}}\right]\left[\boldsymbol{I}_{\boldsymbol{s}}\right] + \left[\boldsymbol{\Lambda}_{\boldsymbol{smr}}\right]^T\left[\boldsymbol{I}_{\boldsymbol{s}}\right]\right\} \\
&= \frac{1}{2}\left[\boldsymbol{I}_{\boldsymbol{s}}\right]^T\frac{\partial}{\partial \theta_m}\left\{\left[\boldsymbol{L}'_{\boldsymbol{ss}}\right]\right\}\left[\boldsymbol{I}_{\boldsymbol{s}}\right] + \frac{\partial}{\partial \theta_m}\left\{\left[\boldsymbol{\Lambda}_{\boldsymbol{smr}}\right]^T\right\}\left[\boldsymbol{I}_{\boldsymbol{s}}\right] \\
&= \frac{1}{2}\left\{\left[\boldsymbol{T}_{\boldsymbol{dq\text{-}abc}}\right]\left[\boldsymbol{I}_{\boldsymbol{dqs}}\right]\right\}^T\frac{\partial}{\partial \theta_m}\left\{\left[\boldsymbol{L}'_{\boldsymbol{ss}}\right]\right\}\left[\boldsymbol{T}_{\boldsymbol{dq\text{-}abc}}\right]\left[\boldsymbol{I}_{\boldsymbol{dqs}}\right] \\
&\quad + \left\{\frac{\partial}{\partial \theta_m}\left[\left[\boldsymbol{\Lambda}_{\boldsymbol{smr}}\right]^T\right]\right\}\left[\boldsymbol{T}_{\boldsymbol{dq\text{-}abc}}\right]\left[\boldsymbol{I}_{\boldsymbol{dqs}}\right] \\
&= \frac{3}{2}\frac{P}{2}\left[K_2{}^2\left(L_{ds} - L_{qs}\right)i_{ds}i_{qs} + \frac{2K_2}{3K_1}\lambda_{mr}i_{qs}\right]
\end{aligned}
\tag{4.28}
$$

Combining Equations (4.21) - (4.28), the model of a *P*-pole, three-phase PM synchronous motor under the rotating *d-q* reference frame emerges as follows

$$\begin{cases} \dfrac{di_{ds}}{dt} = \dfrac{1}{L_{ds}}(-R_s i_{ds} + \omega_e L_{qs} i_{qs} + v_{ds}) \\ \dfrac{di_{qs}}{dt} = \dfrac{1}{L_{qs}}(-R_s i_{qs} - \omega_e L_{ds} i_{ds} - \omega_e \lambda_{mr} + v_{qs}) \\ \dfrac{d\omega_m}{dt} = \dfrac{1}{J}[T_{out} - B\omega_m - T_L] \\ \qquad = \dfrac{1}{J}\{\dfrac{3}{2}\dfrac{P}{2}[{K_2}^2(L_{ds} - L_{qs})i_{ds} i_{qs} + \dfrac{2K_2}{3K_1}\lambda_{mr} i_{qs}] - B\omega_m - T_L\} \end{cases} \tag{4.29}$$

It is obvious from Equation (4.28) that the output torque of the PM synchronous motor is a function of the *d*- and *q*-axis currents. Hence, by controlling i_{ds} and i_{qs} independently and properly, precise control of PM synchronous motors can be achieved.

For PM synchronous motors without saliency, i.e., $L_{ds} = L_{qs}$, Equation (4.28) becomes

$$T_{out} = \frac{P}{2}\frac{K_2}{K_1}\lambda_{mr} i_{qs} \tag{4.30}$$

It can be seen that the electromagnetic torque of the motor consists of only the excitation torque. i_{ds} therefore has no effect on torque production, and its reference value should be set to zero at all time to reduce energy loss. For motors with saliency, i.e., $L_{ds} \neq L_{qs}$, the electromagnetic torque of the motor consists of both excitation torque and reluctance torque, meaning the electromagnetic torque under the stator rotating reference frame is nonlinear. In FOC applications, in order to linearize the torque equation and hence facilitate the control task, the reference value of i_{ds} is still set to zero [61]. However, if maximum efficiency is demanded, the optimal i_{ds} and i_{qs} for a specific output torque need to be properly calculated [62-64].

Figure 4.8 summarizes the basic idea of FOC for PM synchronous motors, where n_p is the number of pole pairs:

1: The stator phase winding currents (i_{as}, i_{bs}, and i_{cs}) are measured and send to the Park's transformation module. The *d*-axis current (i_{ds}) and *q*-axis current (i_{qs}) are then calculated.

2: i_{ds} and i_{qs} are compared to their reference values i_{ds}^* (normally set to zero) and i_{qs}^* (calculated by a PI controller based on the difference between the actual motor speed ω_m and the reference motor speed ω_m^*), respectively. The resulting differences are fed to two PI controllers, which output the *d*-axis voltage (v_{ds}) and *q*-axis voltage (v_{qs}), respectively.

3: v_{ds} and v_{qs} are sent to the inverse Park's transformation module to acquire the required input voltages v_{as}, v_{bs}, and v_{cs}. In practical applications, due to the difficulty in generating sinusoidal voltage signals with varying magnitude and frequency, inverters with modulation techniques are often adopted to imitate v_{as}, v_{bs}, and v_{cs}.

In addition, since both the Park's and inverse Park's transformations require rotor's electrical position (θ_e), a position sensor tracking θ_m is mounted on the rotor shaft and θ_e can be easily determined by Equation (4.10).

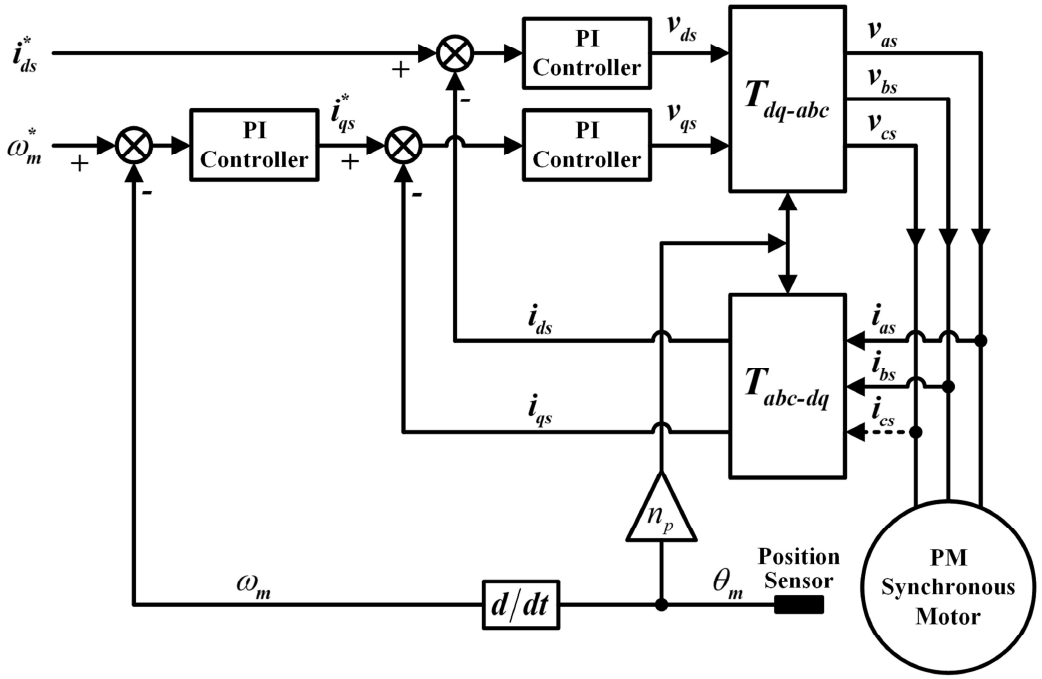

Figure 4.8 Basic control scheme of FOC for PM synchronous motors

4.4 Nonlinear Time-Frequency Control of PM Synchronous Motors

4.4.1 Nonlinear Time-Frequency Speed Control of PM Synchronous Motors

To achieve fast, precise, and robust control of PM synchronous motors, the novel nonlinear time-frequency control concept presented in section 2.4 is incorporated into the classical FOC scheme. Figure 4.9 illustrates the basic design, where the two cascaded PI controllers used for speed and *q*-axis current control in classical FOC are replaced by the nonlinear time-frequency controller.

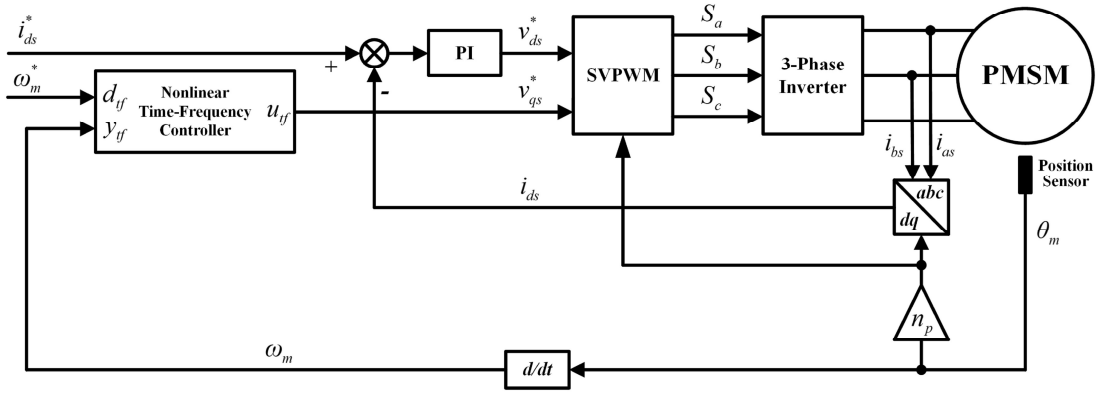

Figure 4.9 Nonlinear time-frequency control based FOC scheme for PM synchronous motor speed control

In Figure 4.9, ω_m^* is selected as d_{tf}, ω_m as y_{tf}, and v_{qs}^* as u_{tf} for the nonlinear time-frequency controller. The stator currents i_{as} and i_{bs} at time step *n* are first measured and send to the Park's transformation module in order to obtain the *d*-axis current i_{ds}. The PI and nonlinear time-frequency controllers then generate the reference control voltages v_{ds}^* and v_{qs}^* based on i_{ds}^* and i_{ds}, ω_m^* and ω_m, respectively. Same as in PI control based FOC, the desired *d*-axis control voltage (v_{ds}^*) and *q*-axis control voltage (v_{qs}^*) generated by the PI controller and nonlinear time-frequency controller are processed by a space vector pulse width (SVPWM) module [65] and converted into pulse width signals (S_a, S_b, and S_c) which drives the on-off states of the switches in the inverter.

To demonstrate the effectiveness of the presented nonlinear time-frequency control based FOC scheme, the speed tracking performance of the control design is

evaluated against a classical PI control based FOC scheme through a series of simulations using an interior-mounted PM synchronous motor whose specifications are listed in Table 4.2. The simulation is implemented in Matlab/Simulink using a fixed-step (discrete) solver running at a 50 μs sampling period. The switching frequency of the SVPWM is 20 kHz.

Table 4.2 Specifications of the interior-mounted PM synchronous motor

Parameters	Value
Rated Speed	3750 rpm
Rated Torque	1.7 N.m
Pole Pairs, n_p	2.0
Stator Resistance, R_s	4.765 Ω
d-axis inductance, L_{ds}	13.3 mH
q-axis inductance, L_{qs}	14.7 mH
Inertia of the rotor, J	0.0001051 Kg.m^2
Friction of coefficient, B	0.00004047 N.m/rad/s
Flux linkage induced by rotor magnets, λ_{mr}	0.1848 V/rad/s

The proposed nonlinear time-frequency control based FOC scheme (NTFC-FOC) and classical PI control based FOC scheme (PI-FOC) are tuned to have comparable transient responses. Figure 4.10 shows the step response of the target PM synchronous motor with PI-FOC and NTFC-FOC under zero load, respectively. Table 4.3 provides a

numeric comparison of the two control schemes in terms of rise time, settling time, and overshoot.

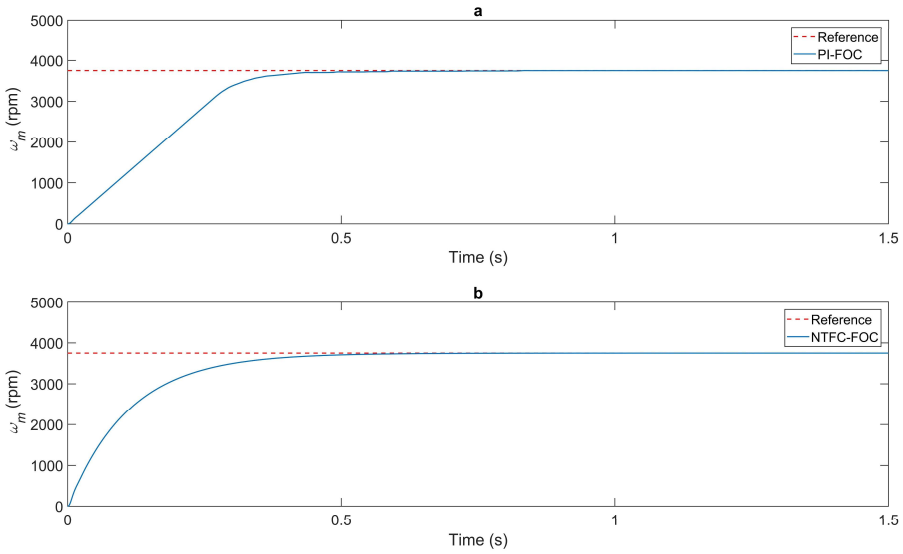

Figure 4.10 Speed step responses under zero torque load: (a) PI-FOC, (b) NTFC-FOC

Table 4.3 Speed step response comparisons of PI-FOC and NTFC-FOC

Performance	PI-FOC	NTFC-FOC
Rise Time	0.267 s	0.245 s
Settling Time	0.412 s	0.438 s
Overshoot	< 0.01%	< 0.01%

From Figure 4.10 and Table 4.3, it is evident that the two control schemes have very similar transient behaviors when there is a step change of the reference speed (0 rpm to 3750 rpm) at t = 0 s.

To illustrate the performance qualities of the introduced NTFC-FOC scheme in speed control, two studies are performed. The first is designed to test the robustness of the applied control scheme when the reference speed is abruptly switched from a positive rated speed to a negative rated speed, followed by switching back from the negative rated speed to the positive rated speed. The initial motor speed is set to the rated motor speed and a constant torque load with the rated value is applied to the rotor shaft.

Figure 4.11 illustrates the speed responses of the motor with PI-FOC and NTFC-FOC. Detailed comparisons of their performance are summarized in Table 4.4. The rise time, settling time and overshoot of NTFC-FOC are much smaller than that of PI-FOC regardless of the direction of speed-switching. Unlike PI-FOC, whose rise time, settling time and overshoot corresponding to speed variation from the negative full speed to positive full speed are all significantly greater than when switching from the positive full speed to negative full speed, NTFC-FOC displays identical rise time, settling time and overshoot in the 2 scenarios of speed switching. Furthermore, based on Table 4.4, the minimum achievable steady state error of NTFC-FOC is registered at less than 0.01% (equivalent to ±0.375 rpm in speed deviation) which is of one order of magnitude smaller than that of PI-FOC, indicating that NTFC-FOC provides a much higher control precision than PI-FOC.

It should be noted that NTFC-FOC is not only able to effectively handle variations to reference changes, but also capable of guaranteeing a fast, precise, and consistent response under large reference variation.

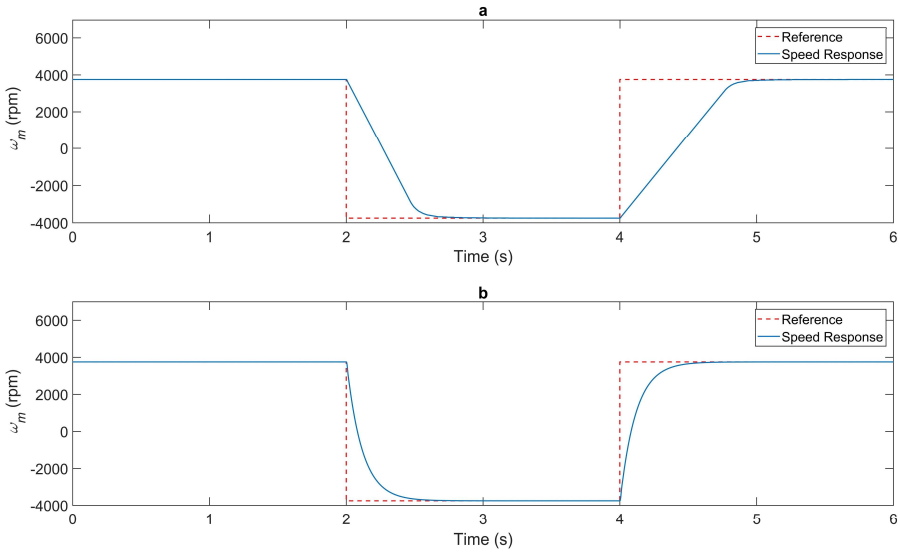

Figure 4.11 Speed response under sudden reference changes: (a) PI-FOC, (b) NTFC-FOC

Table 4.4 Comparisons of PI-FOC and NTFC-FOC under sudden reference changes

Time	Performance	PI-FOC	NTFC-FOC
2 s - 4 s	Rise time	0.426 s	0.251 s
	Settling time	0.611 s	0.449 s
	Overshoot	0.026%	0.012%
	Min. steady state error	0.03%	< 0.01%
4 s - 6 s	Rise time	0.666	0.254 s
	Settling time	0.875 s	0.455 s
	Overshoot	0.052%	0.011%
	Min. steady state error	0.08%	< 0.01%

Figure 4.12 - Figure 4.14 illustrate the motor *d-q* current response, electromagnetic torque response, and phase *a* current response of PI-FOC and NTFC-FOC, respectively. Since the electromagnetic torque is directly proportional to i_{sq} when i_{sd} is close to zero, the *q*-axis current and electromagnetic torque have very similar behaviors. NTFC-FOC is seen to provide a rapid and much smoother electromagnetic torque response than PI-FOC. In addition, when the reference speed changes from the negative rated speed to positive rated speed, the NTFC-FOC phase *a* current overshoot is a slightly higher than PI-FOC's.

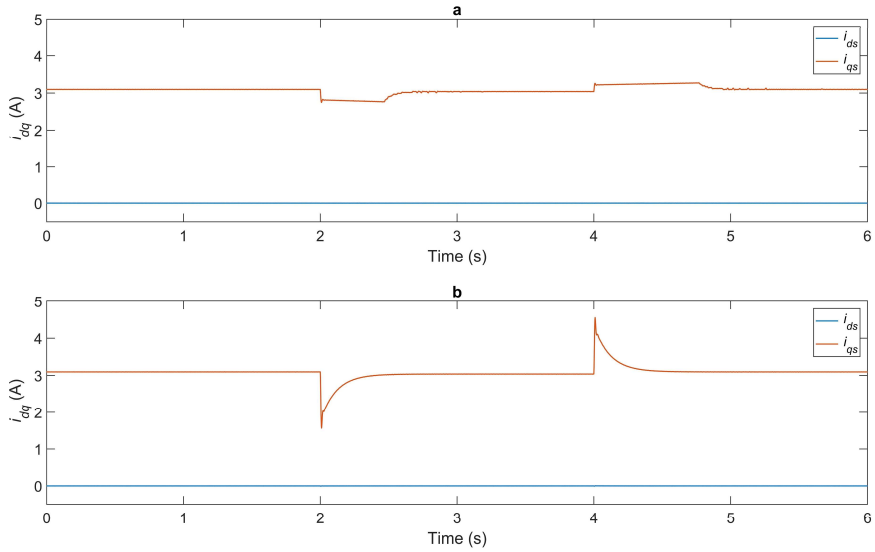

Figure 4.12 *d-q* current response under sudden reference changes: (a) PI-FOC, (b) NTFC-FOC

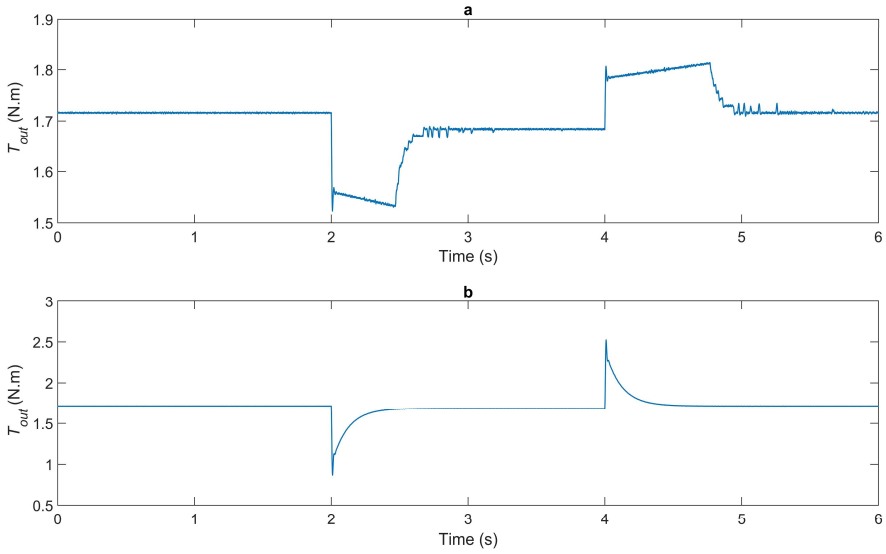

Figure 4.13 Electromagnetic torque response under sudden reference changes: (a) PI-FOC, (b) NTFC-FOC

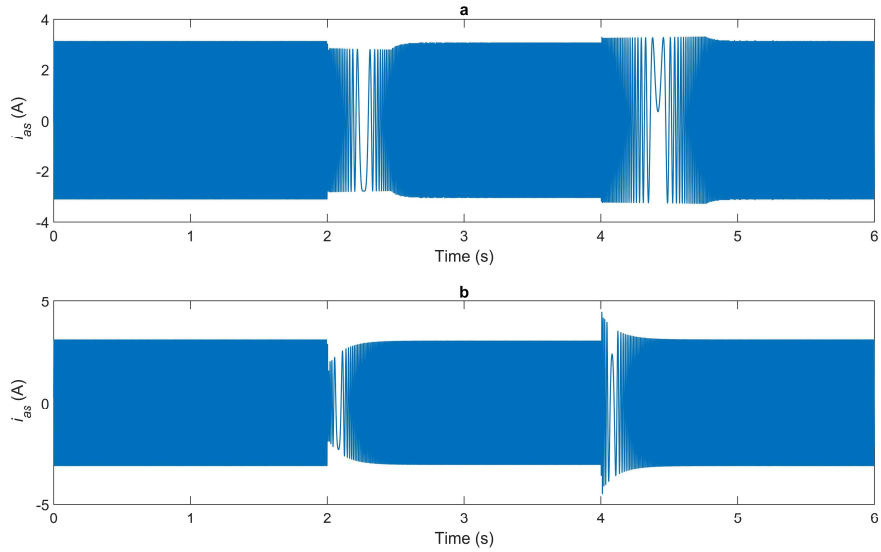

Figure 4.14 Phase *a* current response under sudden reference changes: (a) PI-FOC, (b) NTFC-FOC

Figure 4.15 is a zoom-in on the tracking error of the motor speed. The PI-FOC tracking error zigzags toward zero in the 2 switching scenarios. This is mainly caused by the two PI controllers in the *q*-axis control loop as they are not only cascaded, but operated at different sampling frequencies as well [20]. Such undesirable behaviors significantly degrade the motor's tracking performance and cause high frequency oscillations in the motor current and electromagnetic torque as shown in Figure 4.12 (a) and Figure 4.13 (a). In contrast, the NTFC-FOC tracking error is smooth and free of jagged serrations, thus a strong indication of being robust and accurate than PI-FOC when reference undergoes abrupt changes.

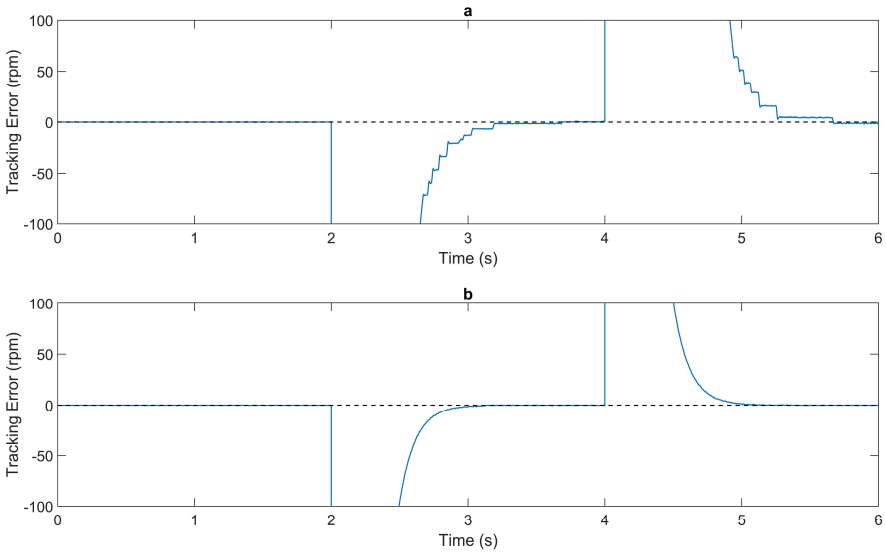

Figure 4.15 Speed tracking error under sudden reference changes: (a) PI-FOC, (b) NTFC-FOC

The second study investigates the robustness of the NTFC-FOC scheme when load torque experiences rapid changes. In the followings, the reference speed and initial speed of the motor are both set to 3,000 rpm. The torque load on the motor shaft is initially zero. A torque load with the rated value is applied at t = 1s and subsequently removed after 2 seconds. Figure 4.16 presents the speed responses of the motor with PI-FOC and NTFC-FOC. The comparison of performance given in Table 4.5 shows that the overshoots are comparable, thus implying that the 2 controllers have similar capabilities in restraining the motor speed when subject to external torque load variations. This provides the basis for further and meaningful performance comparison between the two control schemes.

As indicated in Figure 4.16 that when external torque load suddenly applied or removed, PI-FOC restores back to the reference speed at a faster rate than NTFC-FOC.

However, when the reference speed is reached, the motor takes more time to settle down to the steady state which is confirmed by the settling time tabulated in Table 4.5. Though not approaching the reference speed as fast, NTFC-FOC is seen to settle down faster to the steady state when the motor restores to the reference speed. Such speed responses are more favorable in practice as a smooth and slow speed restore curve prevents the motor from experiencing sudden jerks and hence lower impact on motor bearings. In addition, the minimum steady state error of NTFC-FOC is significantly lower than PI-FOC, as much as one order of magnitude smaller. Therefore, NTFC-FOC is preferred over PI-FOC for rapid, more accurate, and robust performances when external torque load variation is involved.

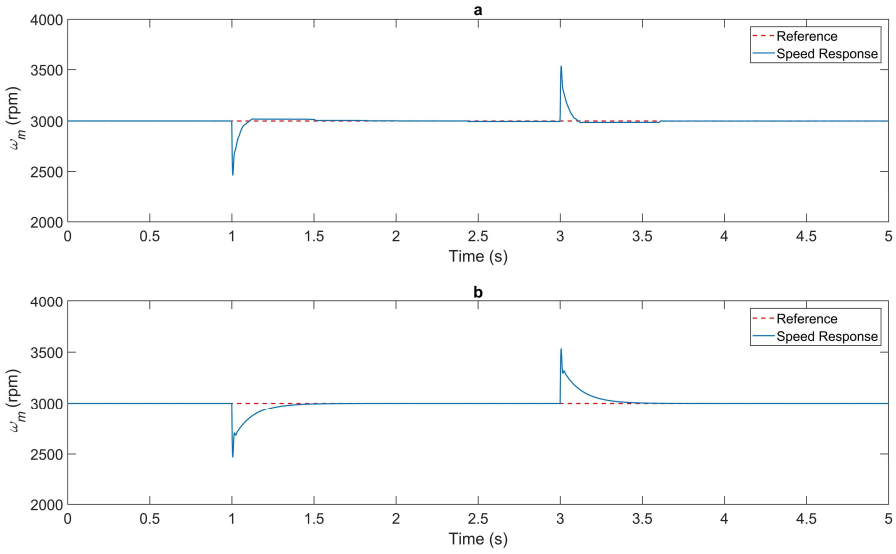

Figure 4.16 Speed response under sudden torque changes: (a) PI-FOC, (b) NTFC-FOC

Table 4.5 Comparisons of PI-FOC and NTFC-FOC under sudden torque changes

Time	Performance	PI-FOC	NTFC-FOC
1 s - 3 s	Settling time	0.507 s	0.411 s
	Overshoot	17.882%	17.689%
	Min. steady state error	1%	0.07%
3 s - 5 s	Settling time	0.606 s	0.413 s
	Overshoot	17.776%	17.710%
	Min. steady state error	0.2%	0.07%

Figure 4.17 - Figure 4.19 demonstrate the motor *d-q* current response, electromagnetic torque response, and phase *a* current response of PI-FOC and NTFC-FOC, respectively. NTFC-FOC is seen to respond notably faster than PI-FOC in electromagnetic torque at the expense of a little higher phase *a* current when torque load suddenly changes.

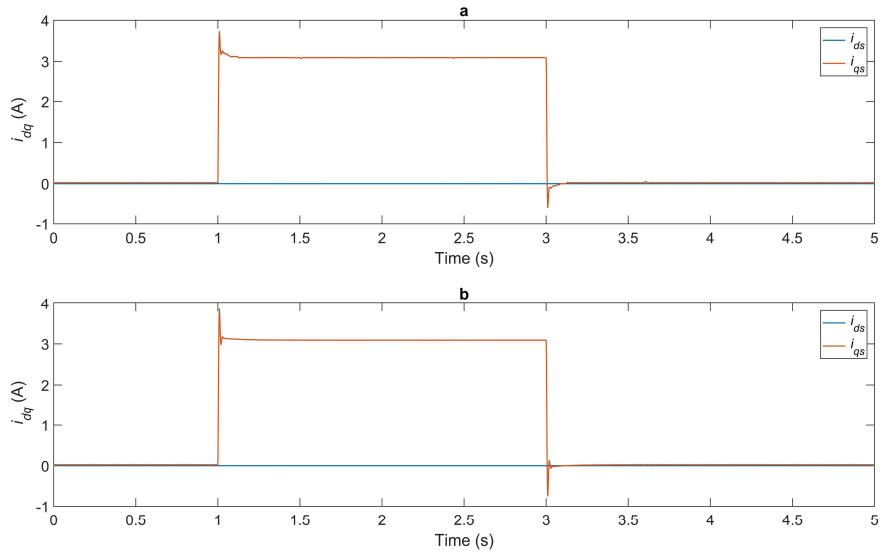

Figure 4.17 *d-q* current response under sudden torque changes: (a) PI-FOC, (b) NTFC-FOC

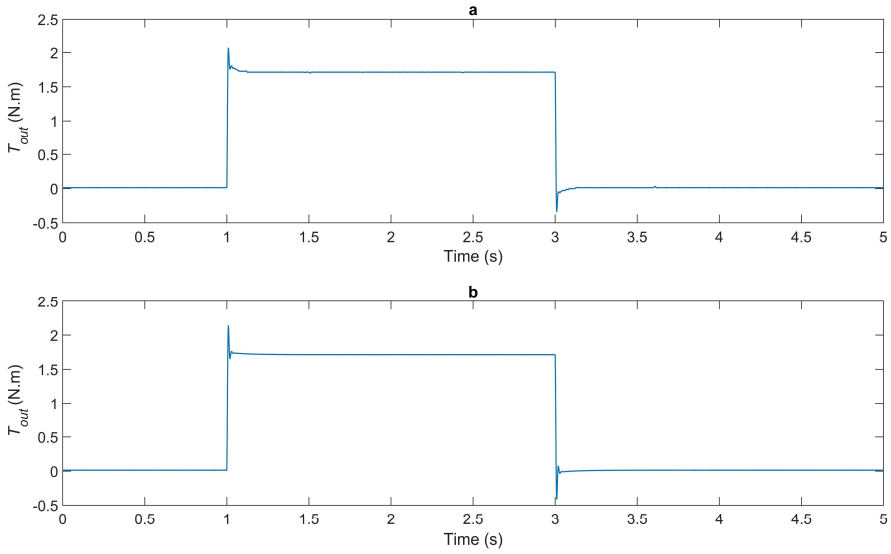

Figure 4.18 Electromagnetic torque response under sudden torque changes: (a) PI-FOC, (b) NTFC-FOC

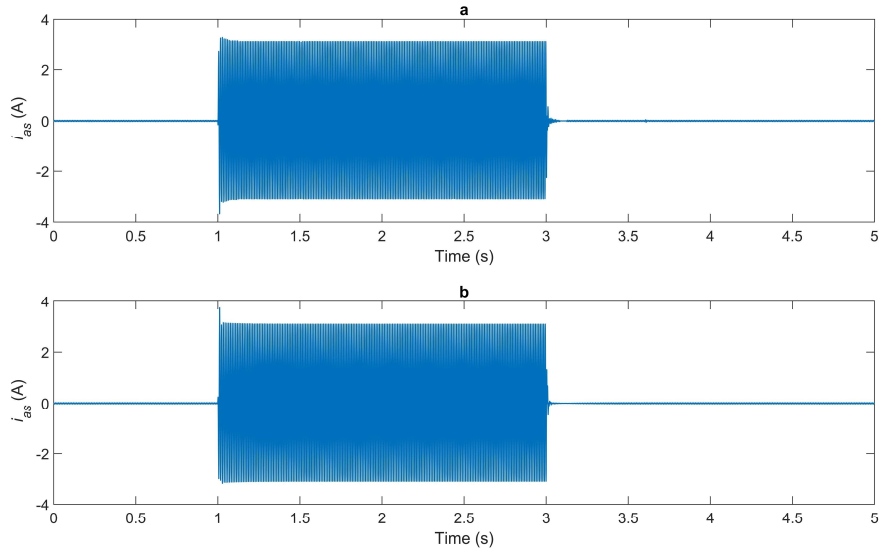

Figure 4.19 Phase *a* current response under sudden torque changes: (a) PI-FOC, (b) NTFC-FOC

Figure 4.20 provides a zoom-in on the tracking error of the motor speed. Albeit capable of restoring the motor speed back to its reference value and maintain it in the steady state margin (2% of the reference value), tracking accuracy of PI-FOC is seen to be severely compromised. This is particularly so when torque load is applied at t = 1 s and removed at t = 3 s. In comparison, the tracking error of NTFC-FOC is smooth and free of any distortion or oscillation, thus supporting the remarks made earlier that the preference is with NTFC-FOC for robustness and accuracy when torque load changes are involved.

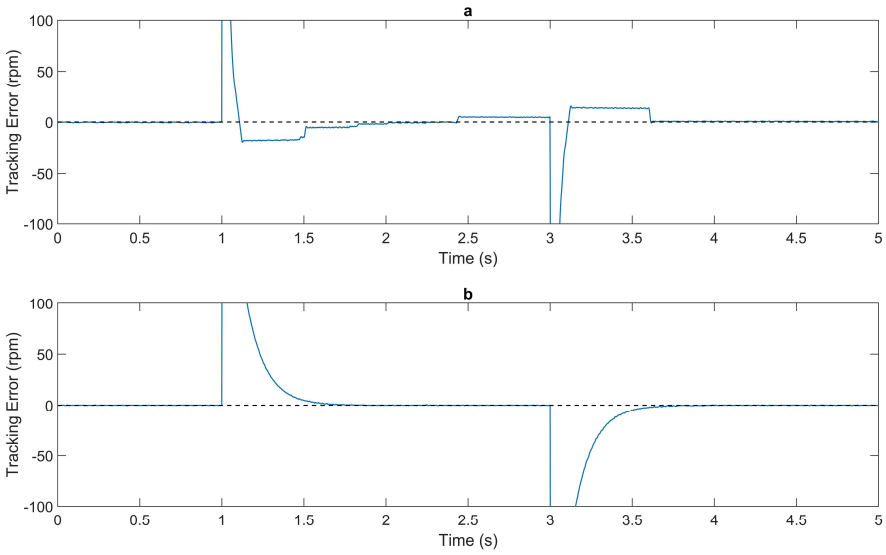

Figure 4.20 Speed tracking error under sudden torque changes: (a) PI-FOC, (b) NTFC-FOC

4.4.2 Nonlinear Time-Frequency Position Control of PM Synchronous Motors

The nonlinear time-frequency control based FOC scheme is also capable of providing precise position control of PM synchronous motors. This can be readily realized by introducing an extra control loop outside the nonlinear time-frequency controller using a simple proportional controller without making any changes to the existing controller parameters. For a detailed description of the particular controller configuration, Reference [52] and [66] are referred.

Figure 4.21 and Figure 4.22 illustrate the PM synchronous motor position response and corresponding tracking error when NTFC-FOC is used for position control. In Figure 4.21, the initial position is set at 360º. At t = 2 s, the reference position abruptly changes

to 1º, followed by returning back to 360º at t = 6 s. During the whole process, a constant torque with the rated value is applied to the rotor shaft.

It is evident from Figure 4.21 and Figure 4.22 that NTFC-FOC is able to control PM synchronous motor position with high precision. Despite rapidly switching reference position from 360º to 1º or the other way, the rotor consistently uses about 1.17 s to reach the desired position with negligibly small overshoots (0.059º from 360º to 1º and 0.983º from 1º to 360º). In addition, NTFC-FOC is able to constrain the rotor position error within 0.13º. NTFC-FOC is therefore effective in both the speed and position control of PM synchronous motors.

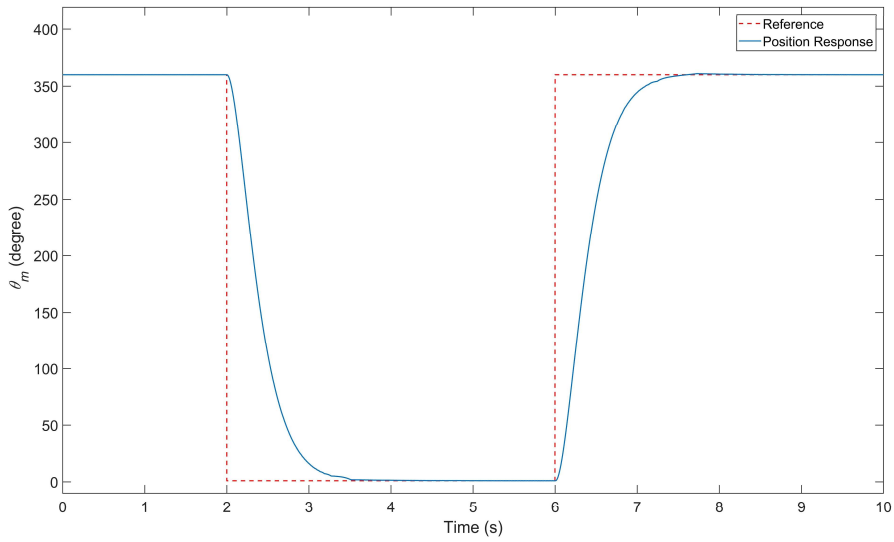

Figure 4.21 Position response with NTFC-FOC

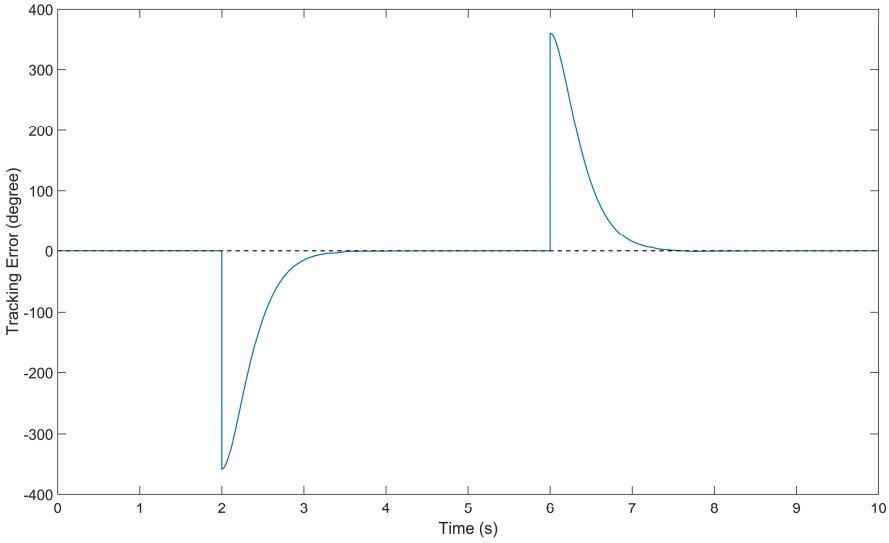

Figure 4.22 Position tracking error with NTFC-FOC

4.5 Experiment Validation

In this section, the nonlinear time-frequency control based FOC scheme is validated through experiment and its performance is compared with a typical PI control based FOC scheme. The experiment setup, illustrated in Figure 4.23, includes a PM synchronous motor, an inverter, a DC power source, a host PC, and a DSP board.

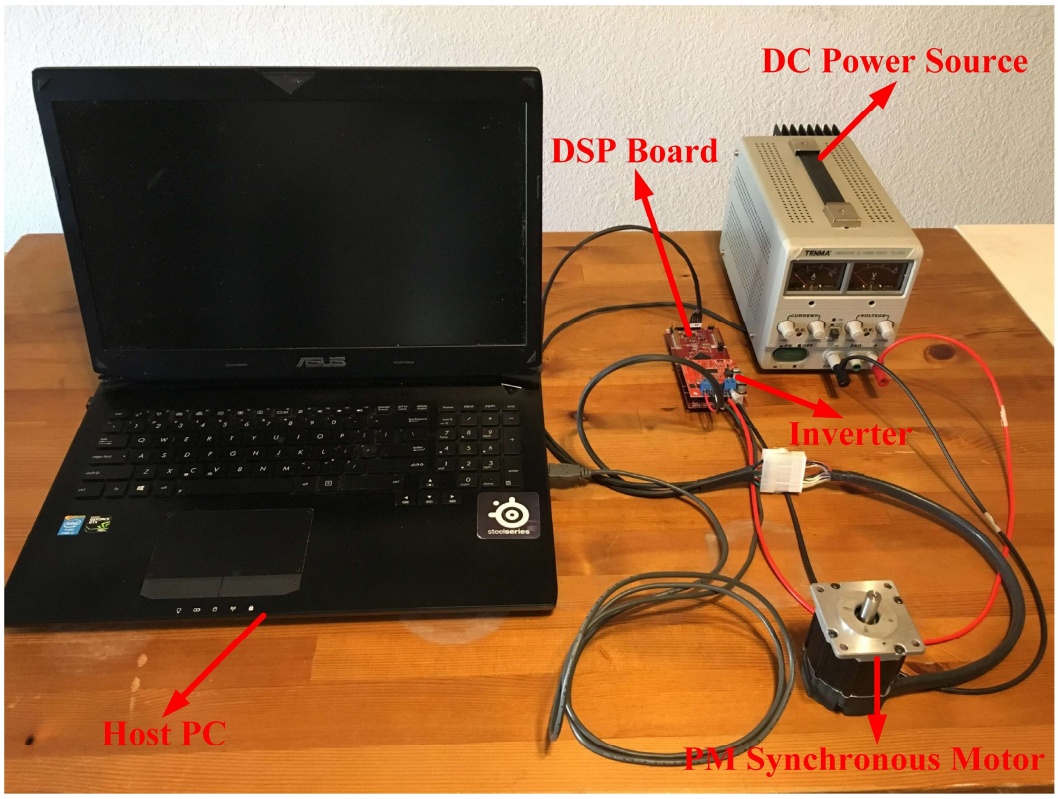

Figure 4.23 Experimental setup

The PM synchronous motor used in the experiment is an M-2310P-LN-04K surface-mounted PM synchronous motor from Teknic with an integrated incremental quadrature encoder. With high quality rare-earth, Neodymium-Iron-Boron magnets in the stator, the motor is of high power density and fade-free at high temperature. In addition, both the stator winding inductance and rotor inertia are designed to be small so that motor responses are fast. Detailed specifications of the motor are given in Table 4.6.

Table 4.6 Specifications of the PM synchronous motor

Parameters	Value
Rated Speed	4500 rpm
Rated Torque	0.2754 N.m
Pole Pairs, n_p	4.0
Stator Resistance, R_s	0.3585 Ω
d-axis inductance, L_{ds}	0.402 mH
q-axis inductance, L_{qs}	0.402 mH
Inertia of the rotor, J	0.00000706 Kg.m^2
Flux linkage induced by rotor magnets, λ_{mr}	0.00654703 V/rad/s
Maximum encoder resolution	4000 counts/rev

The inverter used is a BOOSTXL-DRV8301 three phase variable frequency inverter by Texas Instruments (TI). It is based on TI's DRV8301 three-phase pre-driver and CSD18533Q5A N-channel NexFET^{TM} power MOSFETs. The inverter supports 6 - 24 V input voltage and up to 10 A continuous (14 A peak) current.

The DC power source adopted is a regular laboratory power source. It is capable of providing 0 - 20 V output DC voltage and 0 - 10 A continuous current. The host laptop computer shown in Figure 4.23 is used to upload the control algorithm to the DSP board and acquire the speed and current information of the PM synchronous motor while the experiment is running.

The experimental DSP board is a LAUNCHXL-F28377S control board also by TI. It is based on TI's TMS320F28377S microcontroller which has a clock speed of 200 MHz,

a flash memory of 512 KB, and a RAM memory of 132 KB. The board has four analog-to-digital converters and each of them can provide a sampling frequency up to 3.5 million samples per second. It also has twelve independent enhanced PWM modules (two PWM outputs per module) and three enhanced quadrature encoder pulse modules.

To better evaluate the performance of the nonlinear time-frequency control based FOC scheme, two studies similar to those considered in section 3.3 are performed. In the first study, the motor is initially operating at 1200 rpm with zero torque load. At $t = 0$ s, it changes to 600 rpm and after 6 seconds, it changes back to 1200 rpm. Figure 4.24 and Figure 4.25 show the speed and phase-*a* current responses of the PM synchronous motor with a typical PI control based FOC scheme. The controller gains of the PI controller in the scheme are set to their default factory values.

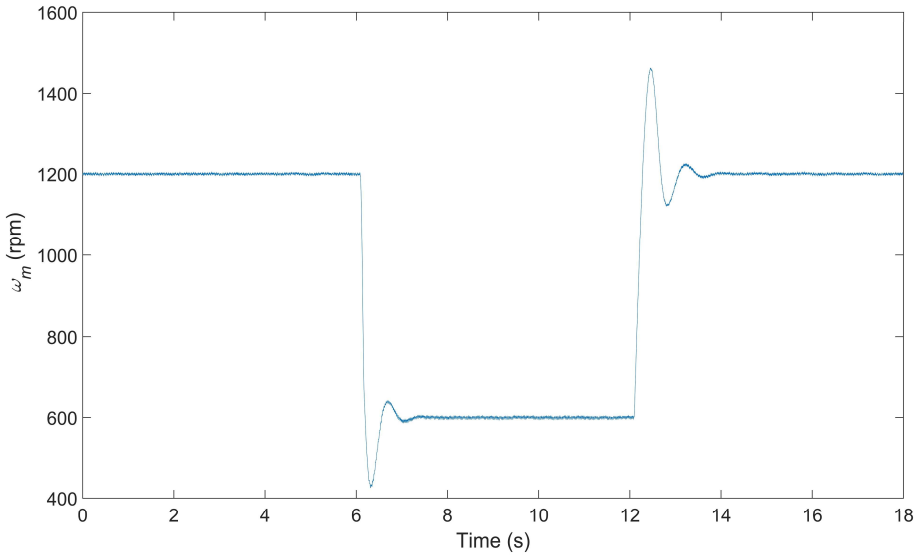

Figure 4.24 Speed response of the typical PI control based FOC scheme under sudden reference changes

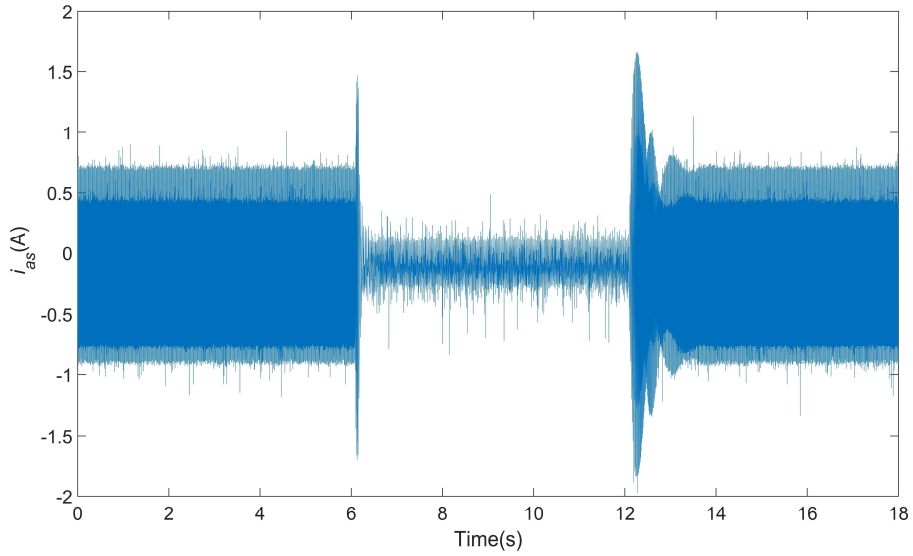

Figure 4.25 Phase-*a* current response of the typical PI control based FOC scheme under sudden reference changes

It can be seen in Figure 4.24 that the PM synchronous motor with the typical PI control based FOC scheme experiences large overshoots when the reference speed suddenly changes and small amplitude, high frequency oscillations at steady states, with the latter noticeably prominent at 1200 rpm. Based on Figure 4.25, the largest overshoot induced in phase-*a* current when the reference speed changes from 1200 rpm to 600 rpm is about 1.5 A, while this value is 1.7 A when the reference speed changes back from 600 rpm to 1200 rpm.

However, there is an issue when comparing this typical PI control based FOC scheme with the nonlinear time-frequency control based FOC scheme. Even though the structure of this typical PI control based FOC scheme largely follows the classical FOC

scheme illustrated in Figure 4.8, it adopts an infinite impulse response (IIR) filter described by,

$$b[n] = 0.01a[n] + 0.99b[n-1] \tag{4.31}$$

where $a[n]$ and $b[n]$ are input and output signal to the IIR filter, respectively, to filter the speed signal obtained from the encoder signals. While in the nonlinear time-frequency control based FOC scheme, no such IIR filters are included to process the measured speed signal. Therefore, to ensure a comparable evaluation, the performance of this typical PI control based FOC scheme without IIR filter is also considered.

Figure 4.26 and Figure 4.27 demonstrate the speed and phase-*a* current responses of the typical PI control based FOC scheme without IIR filter. It can be seen that the overshoots due to the sudden reference changes in both the speed and phase-*a* current are smaller than those registered in Figure 4.24 and Figure 4.25. This is because the IIR filter, which causes delay in the measured speed, is removed and as a result the controller reacts more quickly to the sudden reference changes. However, it is also worth noting that the steady state behaviors of the typical PI control based FOC scheme after the IIR filter is removed are extremely poor. In Figure 4.26, the motor speed is seen to oscillate around the reference speed and cause a large steady state error. This not only suggests that the typical PI control based FOC scheme cannot guarantee a better speed tracking performance without the IIR filter, but also implies that the classical PI control based FOC scheme has poor performance in the frequency domain as well. Specifically, if the speed signal calculated using the encoder signals does not pass through a filter, it will consists of many a high frequency pulse width signal. Therefore, if a control algorithm does not

acquire a strong ability in controlling both the time and frequency domain behavior of the motor, it would not be able to demonstrate satisfactory performance in speed tracking.

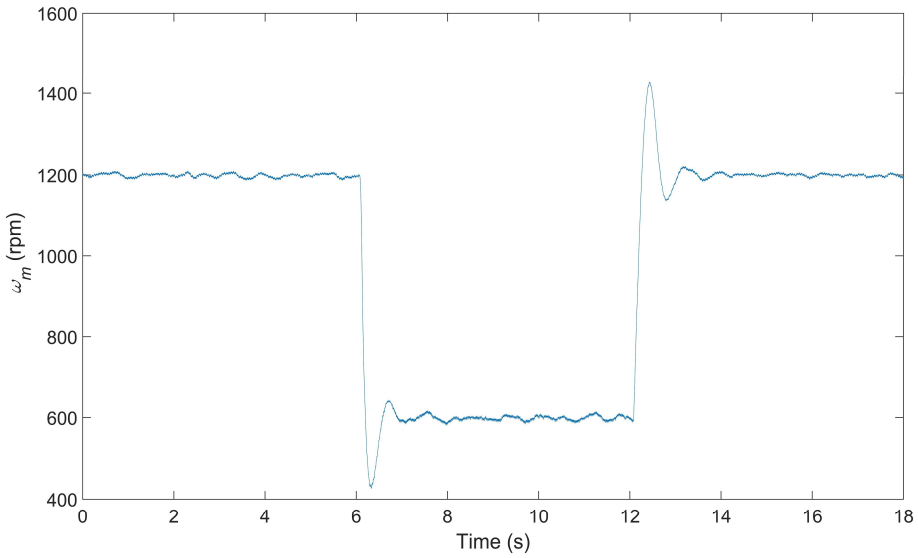

Figure 4.26 Speed response of the typical PI control based FOC scheme without IIR filter under sudden reference changes

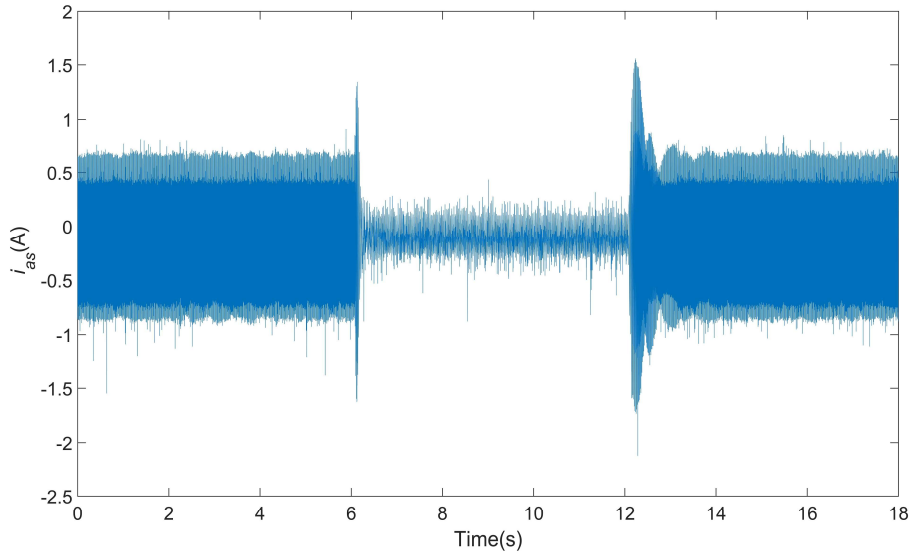

Figure 4.27 Phase-*a* current response of the typical PI control based FOC scheme without IIR filter under sudden reference changes

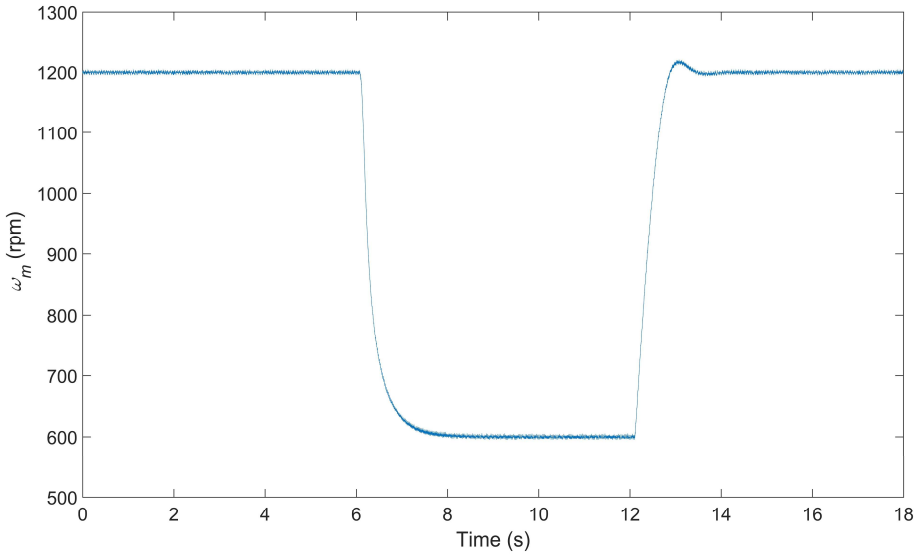

Figure 4.28 Speed response of the nonlinear time-frequency control based FOC scheme under sudden reference changes

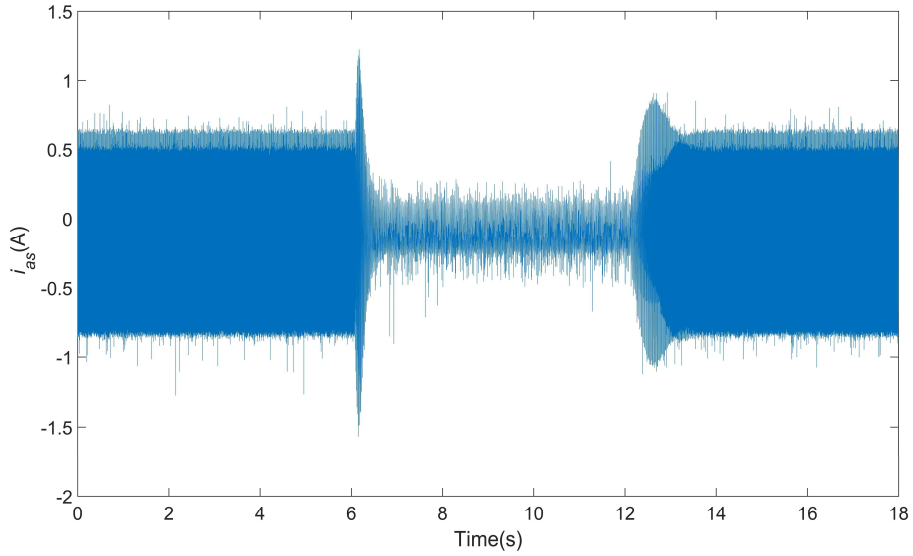

Figure 4.29 Phase-*a* current response of the nonlinear time-frequency control based FOC scheme under sudden reference changes

Figure 4.28 and Figure 4.29 display the speed and phase-*a* current responses of the nonlinear time-frequency control based FOC scheme. Clearly, regardless of the typical PI control based FOC scheme adopting the IIR filter given by Equation (4.31) or not, the nonlinear time-frequency control based FOC scheme performs significantly better than the both of them. Not only the speed and current overshoots caused by sudden reference changes are much smaller than those seen in the PI control based FOC scheme, the speed oscillations at steady state are also much less. Therefore, the nonlinear time-frequency control based FOC scheme is more precise and robust than PI control based FOC scheme when reference speed suddenly changes.

In the next study, the robustness of the typical PI control based FOC scheme and nonlinear time-frequency control based FOC scheme to torque load changes is examined.

In this study, the motor is operated at 900 rpm. At t = 5 s, a torque load is briefly applied to and removed from the rotor shaft. The motor speed is seen to drop to approximately 570 rpm in response to the exertion and removal of the torque. Figure 4.30 and Figure 4.31 illustrate the speed and phase-a current response of the typical PI control based FOC scheme with the IIR filter given in Equation (4.31). The speed and phase-a current response of the typical PI control based FOC scheme without IIR filter and the nonlinear time-frequency control based FOC scheme are provided in Figure 4.32 - Figure 4.33, and Figure 4.34 - Figure 4.35, respectively.

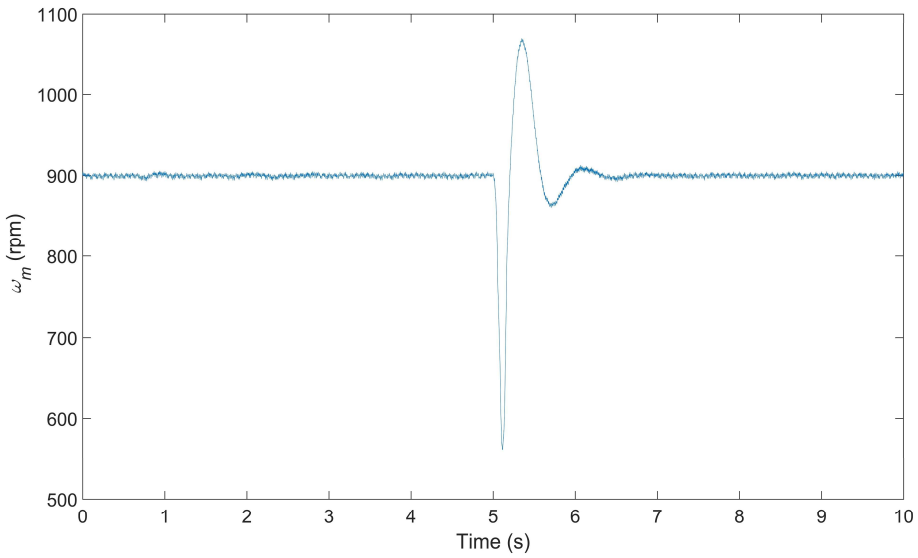

Figure 4.30 Speed response of the typical PI control based FOC scheme under sudden torque load changes

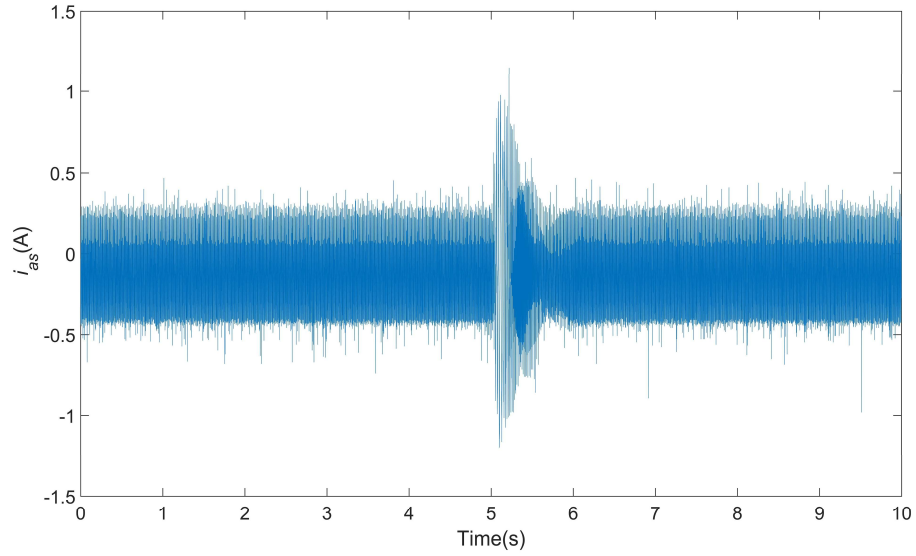

Figure 4.31 Phase-*a* current response of the typical PI control based FOC scheme under sudden torque load changes

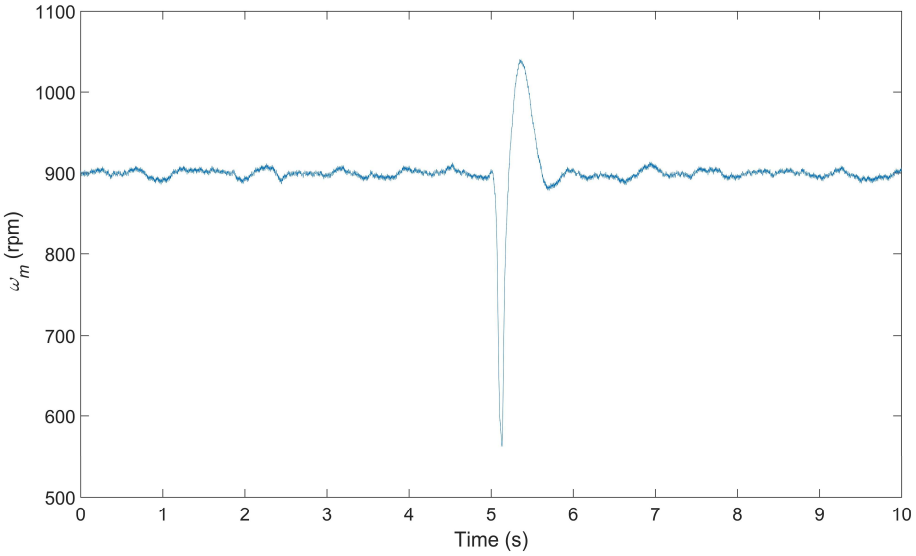

Figure 4.32 Speed response of the typical PI control based FOC scheme without IIR filter under sudden torque load changes

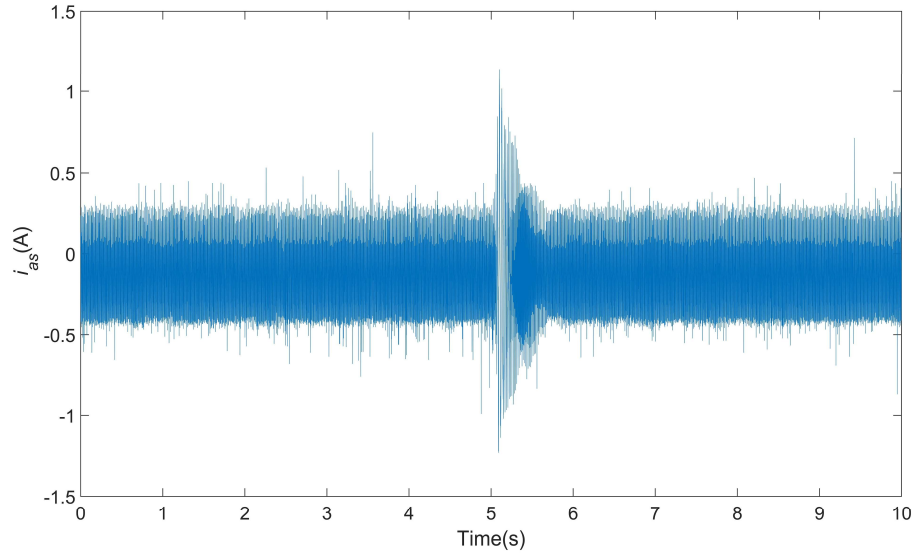

Figure 4.33 Phase-*a* current response of the typical PI control based FOC scheme without IIR filter under sudden torque load changes

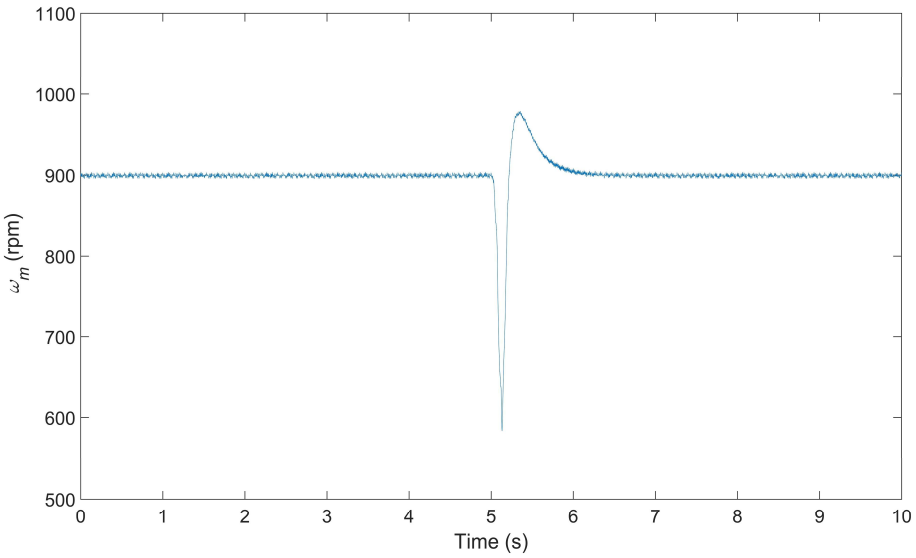

Figure 4.34 Speed response of the nonlinear time-frequency control based FOC scheme under sudden torque load changes

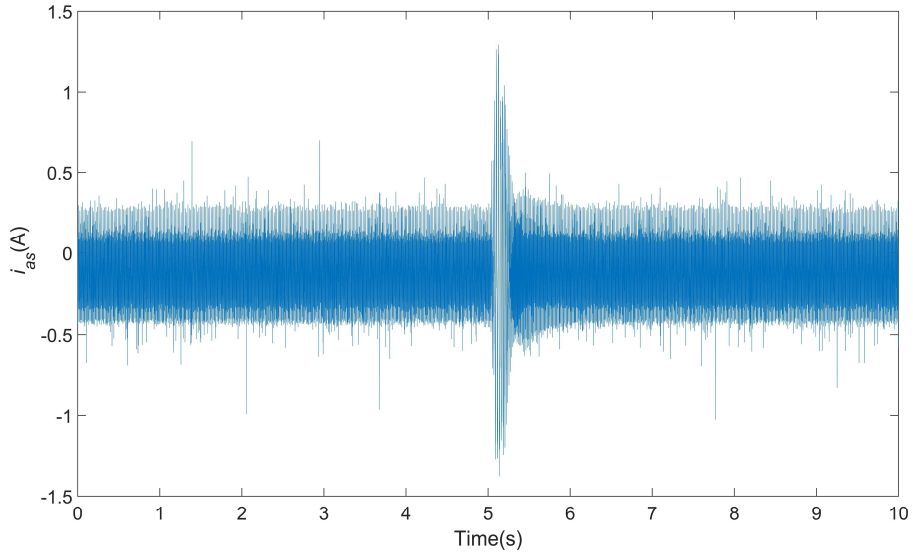

Figure 4.35 Phase-*a* current response of the nonlinear time-frequency control based FOC scheme under sudden torque load changes

From Figure 4.30, Figure 4.32, and Figure 4.34, one sees that the PM synchronous motor with the nonlinear time-frequency control based FOC has the best performance. Not only it has the best speed tracking performance at stead state, the speed overshoot induced by the external torque load is also the smallest. However, from Figure 4.31, Figure 4.33, and Figure 4.35, the current overshoot in the nonlinear time-frequency control based FOC scheme is slightly larger than the typical PI control based FOC scheme with or without IIR filter. Overall, the nonlinear time-frequency control based FOC scheme is more precise and robust than PI control based FOC scheme when external torque load suddenly changes.

4.6 Summary

A comprehensive PM synchronous motor model without damper windings was meticulously derived in the classical *abc* reference frame. In order to reduce its complexity so as to realize field oriented control, Park's transformation was applied and the corresponding transformed PM synchronous motor model defined in the stator rotating reference frame (*d-q* reference frame) was obtained. The nonlinear time-frequency control based FOC scheme for the speed control of PM synchronous motors was then presented based on the developed model. This control scheme, which featured a nonlinear time-frequency controller and a PI controller, was shown to be viable for the fast and robust control of PM synchronous motors with high control accuracy.

The speed tracking performances of the introduced controller design were first evaluated against a classic PI control based FOC scheme through a series of simulations. Its ability in achieving precision position tracking was also illustrated. The proposed nonlinear time-frequency control based FOC scheme was shown to demonstrate four specific advantages over the PI control based FOC design. The first was that the scheme provided a faster and smoother transient response to sudden reference or torque variation. The corresponding steady-state errors were also invariably smaller. Second, unlike PI control based FOC scheme, nonlinear time-frequency control based FOC scheme displayed no serrated features that would otherwise suggest motor instability in the forms of torque ripples and current oscillations. Third, since the control parameters needed not be reset or reconfigured, it is a simple task to switch between speed and position control with the nonlinear time-frequency control based FOC design. Lastly, because the cascaded

structure in PI control based FOC scheme is eliminated, the proposed nonlinear time-frequency control based FOC scheme is much easier to tune than the PI control based FOC architecture.

To validate the simulation results, the nonlinear time-frequency control based FOC scheme was implemented in an experimental setup. Its speed tracking performance was compared against the classical PI control based FOC scheme implemented with default factory settings. To guarantee fairness, the performance of the PI control based FOC scheme with and without the speed IIR filter were both considered. Experimental results confirmed the effectiveness of the nonlinear time-frequency control based FOC scheme. Its superiority in mitigating the instability resulting from rapid variations of the reference speed and external torque was also demonstrated.

5. NONLINEAR TIME-FREQUENCY CONTROL OF CHAOTIC PM SYNCHRONOUS MOTORS*

5.1 Introduction

Decades of research have been done for PM synchronous motors due to their high efficiency, high power density and high reliability over conventional motors. However, a particular challenge still remains. That is, in the event that the corresponding system parameters fall into a certain range, a PM synchronous motor could behave chaotically with the output torque changing haphazardly and motor speed oscillating over a wide range. Such occurrences can gravely degrade the stability and controllability of the PM synchronous motor, thus inevitably compromising its performance.

Control methods successfully applied to address this chaotic behavior of PM synchronous motor include feedback linearization [28], time-delayed feedback [30], Takagi-Sugeno fuzzy control [32], sliding-mode control [33], adaptive control [34], back-stepping control [35], and dither signal injection [36]. However, in addition to applying linearization to facilitate controller development, thus inevitably altering the underlying physics of the dynamic system to be controlled, all these control methods ignore the fact that chaos is a dynamic deterioration occurs in both the time and frequency domains and this route-to-chaos deterioration is a non-stationary process characterized by broadband

*Part of this section is reprinted with permission from "Nonlinear time-frequency control of PM synchronous motor instability applicable to electric vehicle application" by Wang X, Suh CS, 2016, Int J Dyn Control, 4(4), 400-412, Copyright 2016 by Springer

spectral response [37]. None of them has considered the fundamental temporal and spectral qualities inherent of PM synchronous motors and exerted control forces accordingly in both the time and frequency domains.

In this section, a nonlinear time-frequency chaotic control scheme, which is based on the novel nonlinear time-frequency control concept presented in section 2.4, is presented to negate the chaotic response in a simple two-pole, three-phase surface-mounted chaotic PM synchronous motor model. Simulation results show that the designed chaotic control scheme is feasible for alleviating chaotic PM synchronous motor motions with an unconditional state of stability characterized by low amplitude limit-cycles. The nonlinear time-frequency chaotic control scheme demonstrates a significantly better capability in resolving the chaotic states of the PM synchronous motor system with a fast convergence rate. In addition, the control scheme enables rapid PM synchronous motor torque response at high speed and considerably expands the operation range of the motor.

5.2 Chaotic PM Synchronous Motor Model

Based on the Equation (4.29) derived in section 4.3, the power invariant mathematical model of a two-pole, three-phase PM synchronous motor in the rotating *d-q* reference frame is

$$\begin{cases} \dfrac{di_{ds}}{dt} = \dfrac{1}{L_{ds}}(-R_s i_{ds} + \omega_m L_{qs} i_{qs} + v_{ds}) \\ \dfrac{di_{qs}}{dt} = \dfrac{1}{L_{qs}}(-R_s i_{qs} - \omega_m L_{ds} i_{ds} - \omega_m \lambda_{mr} + v_{qs}) \\ \dfrac{d\omega_m}{dt} = \dfrac{1}{J}\{\lambda_{mr} i_{qs} + (L_{ds} - L_{qs}) i_{ds} i_{qs} - B\omega_m - T_L\} \end{cases} \tag{5.1}$$

The system model in Equation (5.1) can be non-dimensionalized following an affine transformation of the form [67]

$$\begin{bmatrix} i_{ds} \\ i_{qs} \\ \omega_m \end{bmatrix} = \begin{bmatrix} \Lambda_d & 0 & 0 \\ 0 & \Lambda_q & 0 \\ 0 & 0 & \Lambda_\omega \end{bmatrix} \begin{bmatrix} \tilde{i}_{ds} \\ \tilde{i}_{qs} \\ \tilde{\omega}_m \end{bmatrix} \tag{5.2}$$

and a time-scaling transformation

$$t = \tau \tilde{t} \tag{5.3}$$

where $\tilde{i}_{ds}$, $\tilde{i}_{qs}$, $\tilde{\omega}_m$ and $\tilde{t}$ are non-dimensionalized version of the original variables i_{ds}, i_{qs}, ω_m and t. Equation (5.1) then becomes

$$\begin{cases} \dfrac{d\tilde{i}_{ds}}{d\tilde{t}} = \dfrac{\tau}{\Lambda_d L_{ds}} (-R_s \Lambda_d \tilde{i}_{ds} + L_{qs} \Lambda_q \Lambda_\omega \tilde{i}_{qs} \tilde{\omega}_m + v_{ds}) \\ \dfrac{d\tilde{i}_{qs}}{d\tilde{t}} = \dfrac{\tau}{\Lambda_q L_{qs}} (-R_s \Lambda_q \tilde{i}_{qs} - L_{ds} \Lambda_d \Lambda_\omega \tilde{i}_{ds} \tilde{\omega}_m - \lambda_{mr} \Lambda_\omega \tilde{\omega}_m + v_{qs}) \\ \dfrac{d\tilde{\omega}_m}{d\tilde{t}} = \dfrac{\tau}{\Lambda_\omega J} [\lambda_{mr} \Lambda_q \tilde{i}_{qs} + (L_{ds} - L_{qs}) \Lambda_d \Lambda_q \tilde{i}_{ds} \tilde{i}_{qs} - B \Lambda_\omega \tilde{\omega} - T_L] \end{cases} \tag{5.4}$$

or alternatively

$$\begin{cases} \dfrac{d\tilde{i}_{ds}}{d\tilde{t}} = (-a_1 \tilde{i}_{ds} + a_2 \tilde{i}_{qs} \tilde{\omega}_m + a_3 v_{ds}) \\ \dfrac{d\tilde{i}_{qs}}{d\tilde{t}} = (-b_1 \tilde{i}_{qs} - b_2 \tilde{i}_{ds} \tilde{\omega}_m - b_3 \tilde{\omega}_m + b_4 v_{qs}) \\ \dfrac{d\tilde{\omega}_m}{d\tilde{t}} = [c_1 \tilde{i}_{qs} + c_2 \tilde{i}_{ds} \tilde{i}_{qs} - c_3 \tilde{\omega}_m - c_4 T_L] \end{cases} \tag{5.5}$$

To streamline the analyses that follow, the number of coefficients are further reduced by setting parameters a_1, a_2, b_1 and b_2 to be 1 using $\Lambda_d = \frac{BR_s}{L_{ds}\lambda_{mr}}$, $\Lambda_q = \frac{BR_s}{L_{qs}\lambda_{mr}}$, $\Lambda_\omega = \frac{R_s}{L_{qs}}$ and $\tau = \frac{L_{qs}}{R_s}$. The transformed PM synchronous motor model is therefore

$$\begin{cases} \frac{d\tilde{i}_{ds}}{d\tilde{t}} = -\tilde{i}_{ds} + \tilde{\omega}_m \tilde{i}_{qs} + \tilde{v}_{ds} \\ \frac{d\tilde{i}_{qs}}{d\tilde{t}} = -\tilde{i}_{qs} - \tilde{\omega}_m \tilde{i}_{ds} + \gamma\tilde{\omega}_m + \tilde{v}_{qs} \\ \frac{d\tilde{\omega}_m}{d\tilde{t}} = \sigma(\tilde{i}_{qs} - \tilde{\omega}_m) + \xi \tilde{i}_{ds}\tilde{i}_{qs} - \tilde{T}_L \end{cases} \tag{5.6}$$

where $\gamma = \frac{\lambda_{mr}^2}{R_s B}$, $\sigma = \frac{L_{qs} B}{R_s J}$, $\tilde{v}_{ds} = \frac{L_{qs}\lambda_{mr}}{R_s^2 B} v_{ds}$, $\tilde{v}_{qs} = \frac{L_{qs}\lambda_{mr}}{R_s^2 J} v_{qs}$, $\xi = \frac{L_{qs} B^2 (L_{ds} - L_{qs})}{L_{ds} J \lambda_{mr}^2}$, and $\tilde{T}_L = \frac{L_{qs}^2}{R_s^2 J} T_L$.

In the case of surface-mounted PM synchronous motor, which has a smooth-air-gap ($L_{ds} = L_{qs}$), the model is further reduced as follows

$$\begin{cases} \frac{d\tilde{i}_{ds}}{d\tilde{t}} = -\tilde{i}_{ds} + \tilde{\omega}_m \tilde{i}_{qs} + \tilde{v}_{ds} \\ \frac{d\tilde{i}_{qs}}{d\tilde{t}} = -\tilde{i}_{qs} + \tilde{\omega}_m(\gamma - \tilde{i}_{ds}) + \tilde{v}_{qs} \\ \frac{d\tilde{\omega}_m}{d\tilde{t}} = \sigma(\tilde{i}_{qs} - \tilde{\omega}_m) - \tilde{T}_L \end{cases} \tag{5.7}$$

Equation (5.7) is configurationally identical to the following famous Lorenz system when $\tilde{v}_{ds} = \tilde{v}_{qs} = \tilde{T}_L = 0$,

$$\begin{cases} \dfrac{dX}{dt} = -\alpha_2 X + YZ \\ \dfrac{dY}{dt} = -Y + Z(\alpha_3 - X) \\ \dfrac{dZ}{dt} = \alpha_1 (Y - Z) \end{cases} \tag{5.8}$$

where X, Y, and Z are state variables; α_1, α_2, and α_3 are system coefficients.

5.3 Chaotic Characteristics of Chaotic PM Synchronous Motor Model

The dynamics of PM synchronous motor have been extensively studied since 1990s using established tools commonly found in nonlinear dynamics and chaos theory [67-69]. A PM synchronous motor would exhibit chaotic motions subject to a certain range of parameters. Although recent research shows that chaotic phenomena can sometime be useful under certain circumstances [70], however, it is generally unacceptable in industrial applications because such extreme dynamic states of instability would seriously degrade the motor performance. Hence, control of chaos in PM synchronous motors is of great interests.

For simplicity, three assumptions are made for the study of PM synchronous motor's chaotic responses:

Assumption 1: Information about $\tilde{i}_{ds}$, $\tilde{i}_{qs}$ and $\tilde{\omega}_m$ are available. To achieve enhanced control, the precise values indicative of the dynamic state of the chaotic PM synchronous motor system are necessary.

Assumption 2: $\tilde{T}_L$ is a known nonzero parameter and $d\tilde{T}_L / d\tilde{t}$ is small [71]. This assumption accounts for the situation when the external torque load applied on the rotor is relatively stable.

Assumption 3: $\sigma = \dfrac{L_{qs}B}{R_s J}$ is a constant, while $\gamma = \dfrac{\lambda_{mr}^2}{R_s B}$ is not. In practice, parameters R_s, B, J and L_{qs} are generally held constant, while λ_{mr}, the flux linkage due to the permanent magnets mounted on the rotor, can be greatly affected by temperature and noise.

In order to comprehensively study the chaotic behaviors of the PM synchronous motor system in Equation (5.7), three representative cases are explored by considering parameters of different values.

Case 1: $\tilde{v}_{ds} = \tilde{v}_{qs} = sin(120\pi t)$, $\tilde{T}_L = 1$, $\tilde{i}_{ds0} = \tilde{i}_{qs0} = \tilde{\omega}_{m0} = 0$; $\sigma = 3$, $\gamma = 21$.

The system is activated from stationary ($\tilde{i}_{ds0}$, $\tilde{i}_{qs0}$, and $\tilde{\omega}_{m0}$ stand for the initial value of $\tilde{i}_{ds}$, $\tilde{i}_{qs}$, and $\tilde{\omega}_m$, respectively) by oscillating voltage input and subjected to a constant external torque load. As indicated by the time responses and phase portrait given in Figure 5.1, the PM synchronous motor demonstrates a state of motion that is characteristically hyperchaotic.

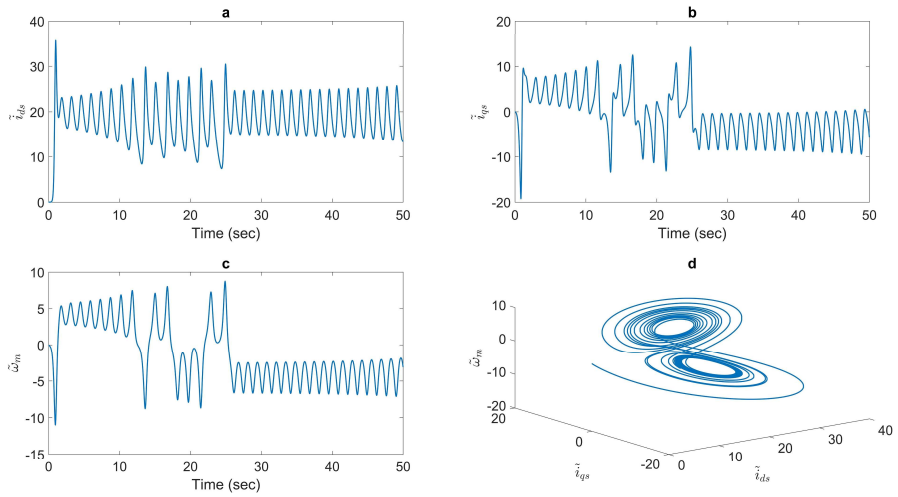

Figure 5.1 Chaotic behavior of Case 1: (a) time response of $\tilde{i}_{ds}$, (b) time response of $\tilde{i}_{qs}$, (c) time response of $\tilde{\omega}_m$, and (d) phase portrait

In addition to experiencing a brief overshoot when the PM synchronous motor first starts, $\tilde{i}_{ds}$, $\tilde{i}_{qs}$ and $\tilde{\omega}_m$ all demonstrate aperiodic behaviors. Combining all the individual dynamics together, the phase portrait of the system is a relatively symmetrical butterfly-like attractor typical of a hyperchaotic system. This chaos phenomenon in PM synchronous motor is harmful as it compromises the normal functioning of the motor, thereby impeding its proper operation. The objective of instability control is to negate this particular chaotic response and restrain the corresponding oscillation amplitude.

Case 2: $\tilde{v}_{ds} = \tilde{v}_{qs} = sin(120\pi t)$, $\tilde{T}_L = 1$, $\tilde{i}_{ds0} = \tilde{i}_{qs0} = \tilde{\omega}_{m0} = 0$; $\sigma = 3$, $\gamma = 21 + 2sin(4\pi t)$.

The case is similar to Case 1 except the system parameter γ is set to oscillate around 21. This case corresponds to the PM synchronous motor being operated under almost the same conditions as Case 1 but subjected to a harsh environment. As shown in

Figure 5.2, the responses of the PM synchronous motor indicate an aggravated state of chaos compared with Case 1.

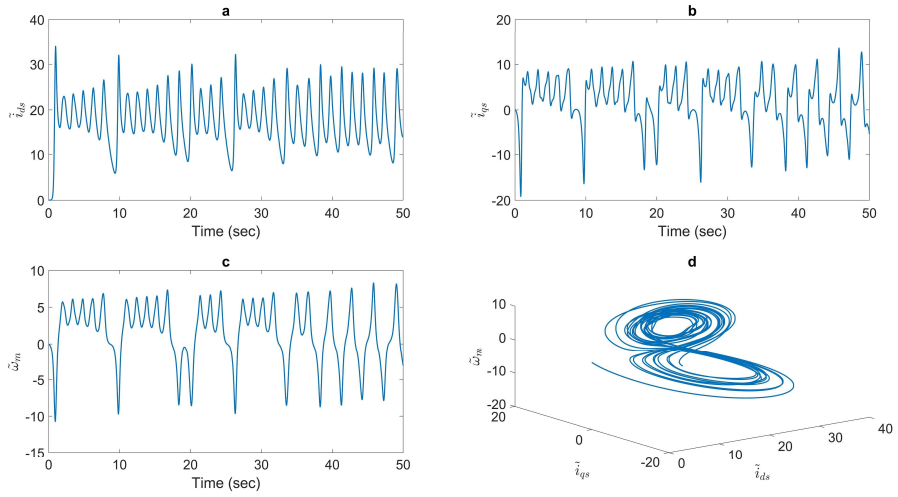

Figure 5.2 Chaotic behavior of Case 2: (a) time response of $\tilde{i}_{ds}$, (b) time response of $\tilde{i}_{qs}$, (c) time response of $\tilde{\omega}_m$, (d) phase portrait

In Figure 5.2, $\tilde{i}_{ds}$, $\tilde{i}_{qs}$ and $\tilde{\omega}_m$ all experience an overshoot initially. Afterwards the oscillations of these three variables become more prominent than Case 1. The aperiodicity of each variable state is readily seen with frequent sharp overshoots. In the time response of $\tilde{i}_{qs}$, the waveform takes on a zigzag pattern. Compare the associated phase portrait with that of the Case 1, the butterfly-like strange attractor demonstrates a certain irregularity. It is clear that the variation of γ has a strong negative impact on the overall performance of the PM synchronous motor.

Case 3: $\tilde{v}_{ds} = \tilde{v}_{qs} = sin(120\pi t)$, $\tilde{T}_L = 1 + 10sin(20\pi t)$, $\tilde{i}_{ds0} = \tilde{i}_{qs0} = \tilde{\omega}_{m0} = 0$; $\sigma = 3$, $\gamma = 21 + 2sin(4\pi t)$.

The conditions specified are similar to Case 2 except that the external torque load $\tilde{T}_L$ is set to oscillate around 1 with a relatively large amplitude. This case corresponds to the PM synchronous motor being operated under almost the same conditions as Case 2 with a small external disturbance applied on the rotor shaft. The worsen state of instability of the PM synchronous motor system under the given conditions can be seen in Figure 5.3.

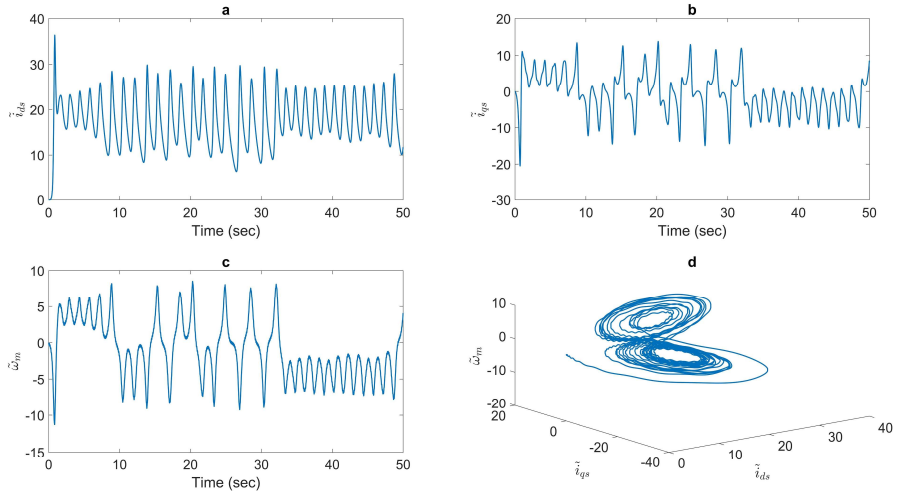

Figure 5.3 Chaotic behavior of Case 3: (a) time response of $\tilde{i}_{ds}$, (b) time response of $\tilde{i}_{qs}$, (c) time response of $\tilde{\omega}_m$, (d) phase portrait

Just as Cases 1 and 2, $\tilde{i}_{ds}$, $\tilde{i}_{qs}$ and $\tilde{\omega}_m$ all display an initial overshoot in Figure 5.3. Since both γ and $\tilde{T}_L$ are varying, the dynamic deterioration of each variable state becomes

more intense. The magnitude of the deteriorating PM synchronous motor state can be appreciated by the corresponding phase portrait which is rugged and seemingly disordered. It is evident that both γ and $\tilde{T}_L$ play a significant role in the instability and dynamic deterioration of the PM synchronous motor system.

5.4 Nonlinear Time-Frequency Control of Chaotic PM Synchronous Motors

Like all chaos systems, the chaotic two-pole, three-phase, surface-mounted PM synchronous motor system scrutinized for the investigation is highly sensitive to initial conditions and parameter variations. Its route-to-chaos response are also characteristically non-stationary in the time domain and broadband in the frequency domain. Such inherent qualities present several challenges to the proper negation of chaos in the PM synchronous motor system.

In this section, a nonlinear time-frequency chaotic control scheme is formulated to mitigate the three cases of chaotic PM synchronous motor states previously presented. The novel nonlinear time-frequency control scheme presented in section 2.4 is followed to realize all the major features of the controller design. Differing from all the previously mentioned methodologies which only focus on control the time-domain behavior of the chaotic PM synchronous motor, the presented control scheme denies dynamic deterioration in both the time and frequency domains simultaneously.

Figure 5.4 illustrates the basic configuration of the proposed nonlinear time-frequency chaotic control scheme for the chaotic PM synchronous motor model presented in Equation (5.7). In Figure 5.4, $\tilde{i}_{ds}$ is selected as the state variable to be controlled, $\tilde{i}_{ds}^{*}$ is the reference value of $\tilde{i}_{ds}$, and V_{dqs} is the control effort (u_{tf}) generated by the nonlinear

time-frequency controller. The control algorithm of the nonlinear time-frequency controller is identical to what was elaborated in section 2.4.

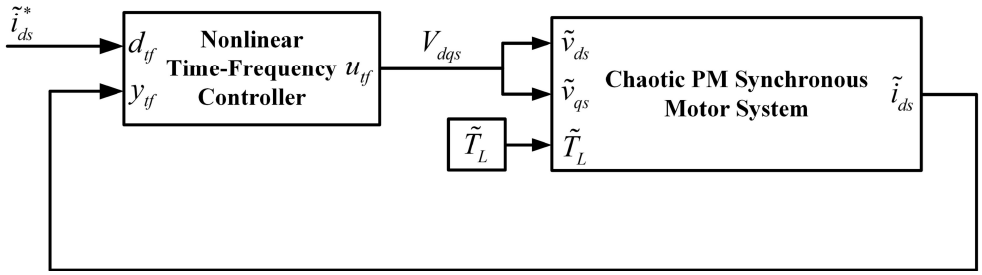

Figure 5.4 Nonlinear time-frequency chaotic control scheme for the chaotic PM synchronous motor system

To demonstrate that the developed nonlinear time-frequency chaotic control scheme is both viable and effective in negating the various states of instability that are innate properties of the PM synchronous motor system, several studies are performed. To ensure consistency with the three cases previously considered, the input signal (x_{tf}) of the nonlinear time frequency controller is set to be $sin(120\pi t)$ and the external torque load ($\tilde{T}_L$) is set to equal to its value assumed in each case.

To determine $\tilde{i}_{ds}^{*}$, the desired stable response of $\tilde{i}_{ds}$, the notion of instantaneous frequency is adopted. Figure 5.5 and Figure 5.6 display the instantaneous frequency [72] of $\tilde{i}_{ds}$ at low frequency range and its corresponding time response in Case 1, respectively. According to Figure 5.5, the dominant frequency of $\tilde{i}_{ds}$ between 0 and 50 seconds is

around 0.8Hz and its corresponding amplitude is approximately 0.05. From the time response of $\tilde{i}_{ds}$ in Figure 5.6, the amplitude of $\tilde{i}_{ds}$ is seen oscillating around 20. $\tilde{i}_{ds}^{*}$ is thus chosen to be $i_{ds}^{*} = 20 + 0.05sin(2\pi \times 0.8t)$.

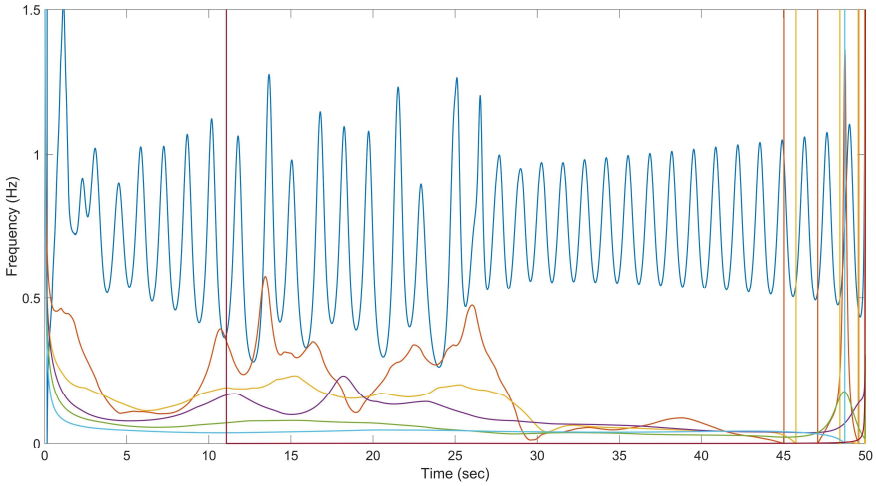

Figure 5.5 Instantaneous frequency of $\tilde{i}_{ds}$ at low frequency range in Case 1

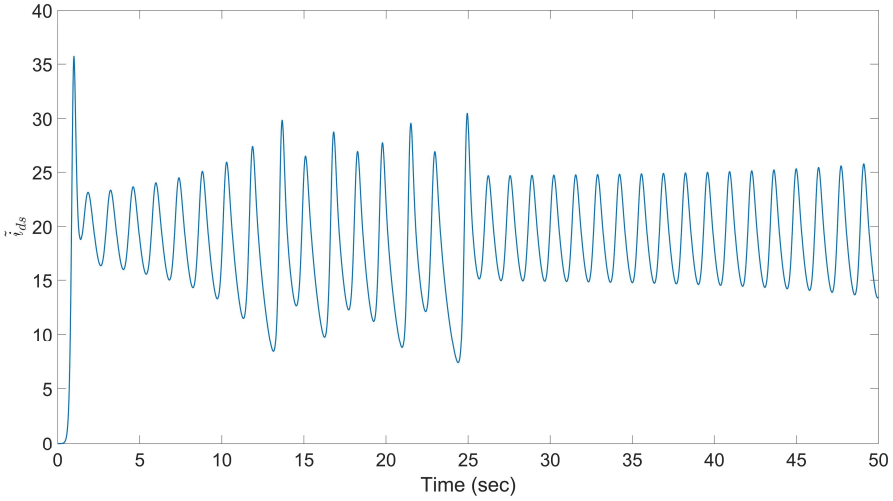

Figure 5.6 Time response of $\tilde{i}_{ds}$ in Case 1

The effectiveness of the nonlinear time-frequency chaotic control scheme for each case in mitigating the chaotic behaviors of the PM synchronous motor system is demonstrated in the following figures.

Case 1: $\tilde{v}_{ds} = \tilde{v}_{qs} = sin(120\pi t)$, $\tilde{T}_L = 1$, $\tilde{i}_{ds0} = \tilde{i}_{qs0} = \tilde{\omega}_{m0} = 0$; $\sigma = 3$, $\gamma = 21$.

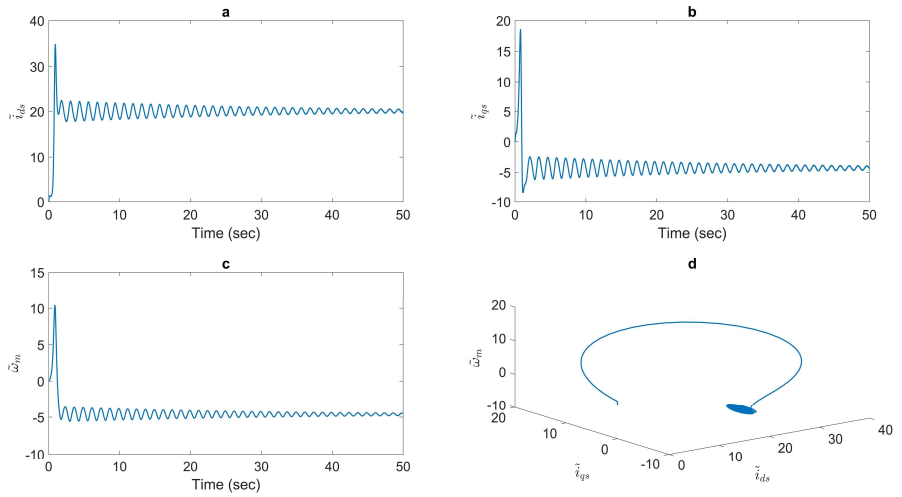

Figure 5.7 Case 1 with the nonlinear time-frequency chaotic control scheme: (a) time response of $\tilde{i}_{ds}$, (b) time response of $\tilde{i}_{qs}$, (c) time response of $\tilde{\omega}_m$, (d) phase portrait

Case 2: $\tilde{v}_{ds} = \tilde{v}_{qs} = sin(120\pi t)$, $\tilde{T}_L = 1$, $\tilde{i}_{ds0} = \tilde{i}_{qs0} = \tilde{\omega}_{m0} = 0$; $\sigma = 3$, $\gamma = 21 + 2sin(4\pi t)$.

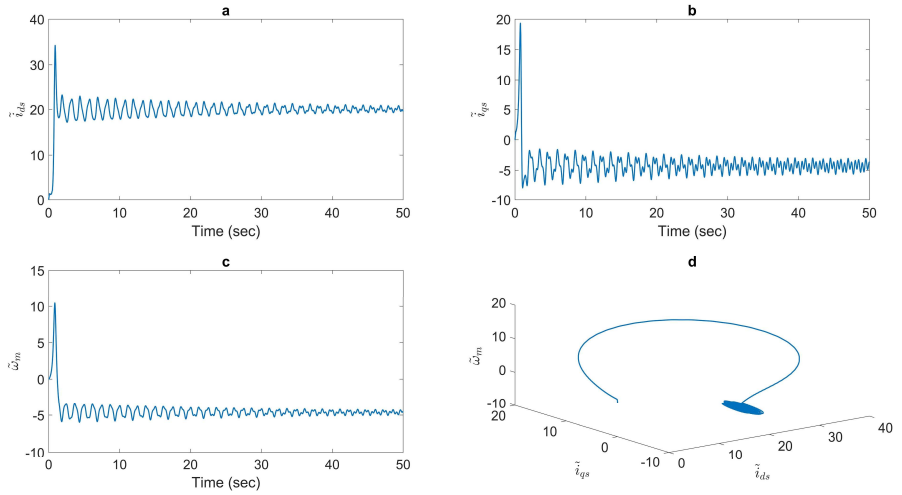

Figure 5.8 Case 2 with the nonlinear time-frequency chaotic control scheme: (a) time response of $\tilde{i}_{ds}$, (b) time response of $\tilde{i}_{qs}$, (c) time response of $\tilde{\omega}_m$, (d) phase portrait

Case 3: $\tilde{v}_{ds} = \tilde{v}_{qs} = sin(120\pi t)$, $\tilde{T}_L = 1 + 10sin(20\pi t)$, $\tilde{i}_{ds0} = \tilde{i}_{qs0} = \tilde{\omega}_{m0} = 0$; $\sigma = 3$, $\gamma = 21 + 2sin(4\pi t)$.

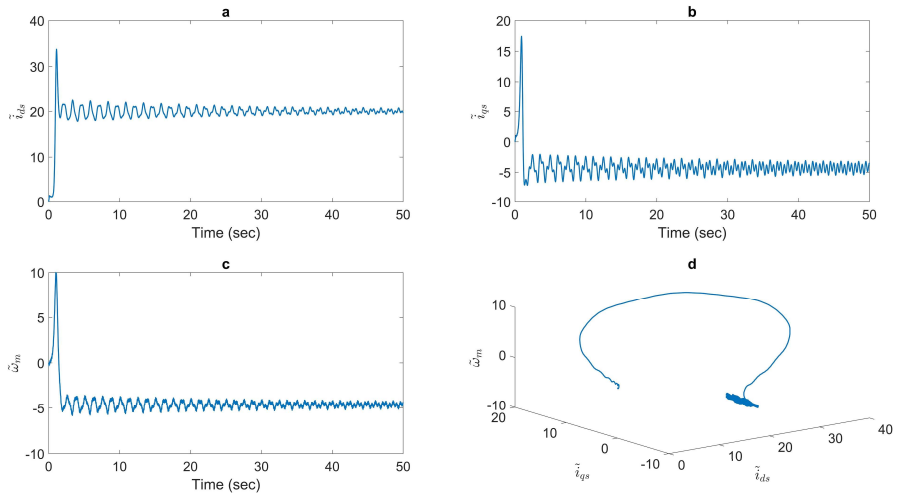

Figure 5.9 Case 3 with the nonlinear time-frequency chaotic control scheme: (a) time response of $\tilde{i}_{ds}$, (b) time response of $\tilde{i}_{qs}$, (c) time response of $\tilde{\omega}_m$, (d) phase portrait

It is evident from Figure 5.7 that the chaotic behaviors associated with the system variables in Case 1 are successfully negated with a low amplitude periodic response immediately after the overshoot (which is the inherent initiation process of the PM synchronous motor system). Quasi-periodic responses of very low amplitude are also observed for Cases 2 and 3 in Figure 5.8 and Figure 5.9. In all cases the signatory butterfly-like strange attractors seen in Figure 5.1-Figure 5.3 are invariably resolved and replaced with well-defined limit-cycles as a result. In addition, the normalized rotor angular velocity, $\tilde{\omega}_m$, is seen to quickly stabilize with diminishing oscillation amplitude,

signifying a dynamic state of stable operation that is highly desirable for PM synchronous motors. Similar observations can also be made in all the figures with the two normalized stator currents, $\tilde{i}_{ds}$ and $\tilde{i}_{qs}$. The implication of being able to mitigate nonlinearity and maintain almost time-invariant stator currents in PM synchronous motor is significant in two particular regards. The first is improved thermal stability of the associated power electronic devices, and thus ultimately the safety of the motor, as the supplying of currents can be precisely regulated with significantly less overheating. The second is necessarily implied by the above, which is less consumption of the energy.

5.5 Summary

In this section, a nonlinear time-frequency chaotic control scheme feasible for mitigating the devastating chaotic behaviors of a elementary two-pole, three-phase, surface-mounted PM synchronous motor model under high speed was considered. Through applying instantaneous frequency to resolve the target chaotic state $\tilde{i}_{ds}$ in the joint time-frequency domain, the desired output of the control scheme, $\tilde{i}_{ds}^{*}$, was determined that warranted the optimal performance of the chaotic PM synchronous motor system. By integrating discrete wavelet transform and adaptive technique, the nonlinear time-frequency chaotic control scheme was demonstrated to capture the intrinsic dynamics of the system and adjust and guide the various deteriorating states of instability and chaos to move toward the desired output ($\tilde{i}_{ds}^{*}$). Simulation results showed that the designed control scheme is viable for mitigating the instability and chaotic response of the PM synchronous motor system with highly desirable performance.

6. CONCLUSIONS

6.1 Summary

The objective of this research is to formulate proper nonlinear time-frequency control schemes for the precision and robust control of PM electrical machines. This type of electrical machines is widely popular in industrial applications due to their being ease in control, compact in size, low in power loss, and fast in response, to name only a few. However, modern control theories designed to control PM electrical machines only focus on controlling their time-domain responses while completely ignoring the corresponding frequency domain behaviors. As a result, PM electrical machines under their control do not perform well when motor nonlinearity is dominant.

To address this issue, the nonlinear time-frequency control notion formulated by Liu and Suh was adopted to develop three nonlinear time-frequency control schemes demonstrated to be feasible for the control of PM electrical machines. The nonlinear time-frequency control schemes were developed for the speed and position control of PM brushed DC motors, speed and position control of PM synchronous motors, and chaos control of PM synchronous motors, respectively.

The research first started with realizing the concurrent speed and position control of a PM brushed DC motor. A nonlinear time-frequency speed control scheme was presented for a PM brushed DC motor and its tracking performance was evaluated against popular PID and fuzzy logic speed control schemes using a series of simulations. The first case studied aimed to test the robustness of the three control schemes when reference

speed suddenly changes and the external torque load remained constant. Simulation results showed that the three control schemes demonstrated similar time-domain behaviors and the nonlinear time-frequency speed control scheme was advantageous over the other two control schemes with regard to current profile. To further demonstrate the merit of the nonlinear time-frequency speed control scheme, the impact of sensor noise was considered. Results showed that the nonlinear time-frequency control was unmatched by both the PID speed control and fuzzy logic speed control in terms of time-domain behaviors, voltage and current profiles, and energy consumption. Analyses on the frequency components of the motor current also indicated that the nonlinear time-frequency speed control scheme was able to control not only the time-domain behaviors of the motor, but its frequency domain behaviors as well. The second case aimed to test the robustness of the three speed control schemes when external torque load abruptly varied while the reference operating speed was kept the same. Simulation results demonstrated that when there was no sensor noise introduced, the three speed control schemes all had satisfactory performance. However, when sensor noise was included, the nonlinear time-frequency speed control scheme performed overwhelmingly well than the other two schemes in both the time and frequency domains. Therefore, the developed nonlinear time-frequency speed control scheme is preferred over the PID and fuzzy logic control schemes under harsh working conditions where system stability, operation reliability, high control precision, fast response, and robustness are demanded. In addition to achieving satisfactory performance in speed control, the nonlinear time-frequency speed control scheme can also be applied to the precise position tracking of PM brushed

DC motors. This is readily achieved by introducing a simple proportional controller into the current nonlinear time-frequency speed control scheme without redefining any existing control parameters. Two cases similar to the cases studied in speed tracking were considered and both evaluated against the classical PID position control and fuzzy logic position control schemes. Since the PID control and fuzzy logic control failed in achieving satisfactory position tracking, the effect of sensor noise was only considered in the nonlinear time-frequency position control scheme. Final results showed that the nonlinear time-frequency position control scheme not only possessed excellent performance when the reference position or external torque suddenly varied, it was capable of maintaining this satisfactory performance in the presence of strong sensor noise. Therefore, the nonlinear time-frequency position control scheme is also recommended for the precision and robust position control of PM brushed DC motors, in particular under severe working environment. This necessarily implies that precision speed and position tracking of PM brushed DC motors can be concurrently realized using the nonlinear time-frequency speed control scheme.

Another nonlinear time-frequency speed control scheme was also developed for PM synchronous motors. The control scheme was based on the traditional PI control based FOC architecture. In the proposed scheme, the two cascaded PI controllers for speed and q-axis current were replaced with a nonlinear time-frequency controller, while the d-axis current was still controlled by a PI controller as in standard PI control based FOC schemes. To demonstrate the effectiveness of this scheme, the speed tracking performance of the design was first evaluated against a classical PI control based FOC scheme through a series

of simulations on an interior-mounted PM synchronous motor. The first case being evaluated aimed to test the robustness of the two speed control schemes when reference speed suddenly changed. Results showed that the nonlinear time-frequency control based FOC scheme not only was able to provide a more robust and accurate tracking response than the PI control based FOC scheme, it also eliminated the current ripples caused by the stair like changes when motor speed was close to the desired value in the PI control based FOC scheme. The second case considered aimed to test the robustness of the two control schemes when external torque suddenly varied. Results again demonstrated that the nonlinear time-frequency control based FOC scheme was more robust and accurate than the PI control based FOC scheme. In addition to achieving satisfactory speed tracking performance, the existing nonlinear time-frequency control based FOC scheme can also be used to achieve precise position tracking. This can be readily realized by adding an extra control loop outside the current nonlinear time-frequency control based FOC scheme using a simple proportional controller without making any changes to the current control parameters. Therefore, the nonlinear time-frequency control based FOC scheme is effective in both the speed and position control of PM synchronous motors. An experimental study has also been conducted to further validate the simulated performance of the nonlinear time-frequency control based FOC design on a surface-mounted PM synchronous motor. In the study, the speed tracking performance of the nonlinear time-frequency control based FOC scheme was compared with a classical PI control based FOC scheme. The PI control based FOC scheme was implemented with factory tuned controller parameters and its tracking performance with and without the speed IIR filters were both

considered. The final test results confirmed not only the effectiveness of the nonlinear time-frequency control based FOC scheme, but also the robustness of the design when the reference speed or external torque load abruptly changes.

To demonstrate the superior capability of the nonlinear time-frequency control concept in mitigating strong nonlinearity, a nonlinear time-frequency chaotic control scheme was developed for the chaos suppression in PM synchronous motors. A two-pole, three-phase, PM synchronous motor established in the rotating *d-q* reference frame was first transformed into a Lorenz attractor like chaotic system. Its chaotic behaviors were studied in three different cases. The presented nonlinear time-frequency chaotic control scheme was then applied to mitigate the chaotic behaviors appeared in the three cases studied. Simulation results showed that the controller design was viable for the chaos control of PM synchronous motor systems with highly desirable performance. In summary, the nonlinear time-frequency control concept is feasible for PM electrical machine control provided the corresponding control scheme is properly designed.

6.2 Achievements

This research has developed three nonlinear time-frequency control schemes employing the novel nonlinear time-frequency control concept for the speed and positon control of PM brushed DC motors, speed and position control of PM synchronous motors, and chaos control of PM synchronous motors, respectively. The most advantageous feature of the designed control schemes is their ability in generating a proper control effort that controls the system response in both the time and frequency domains. It is expected that the developed nonlinear time-frequency control schemes to have a significant impact

on the proper control of electrical machines thus contributing to their broader applications. Specifically, the research has achieved the followings:

1. Developed a nonlinear time-frequency control scheme for the speed and positon control of PM brushed DC motors.

The designed nonlinear time-frequency speed control scheme for PM brushed DC motors controls the motor speed directly as in the classical PID speed control scheme and fuzzy logic speed control scheme. It is an integration of discrete wavelet transformation and adaptive control. Unlike contemporary control theories such as PID speed control scheme and fuzzy logic speed control schemes, which only focus on reducing the time-domain steady state error, the designed speed control scheme can resolve motor time and frequency information simultaneously and generate an appropriate armature control voltage. Through incorporating an extra proportional controller to the speed control scheme while keeping all controller parameters unchanged, precise and robust position control can readily be realized.

2. Developed a nonlinear time-frequency control scheme for the speed and positon control of PM synchronous motors.

The developed nonlinear time-frequency speed control scheme is based on the standard field oriented control concept. It consists of one PI controller and one nonlinear time-frequency controller. The PI controller is used for the *d*-axis current control, while the nonlinear time-frequency controller replaces the two cascaded PI controllers used for the speed and *q*-axis current control in the classical field oriented control. In terms of

position control, only an extra position control loop needs to be added to the existing speed control scheme using a simple proportional controller.

3. Developed a nonlinear time-frequency control scheme for the chaos control of PM synchronous motors.

The developed nonlinear time-frequency chaos control scheme for PM synchronous motors is based on a transformed chaotic two-pole, three-phase, PM synchronous motor model. The non-dimensionalized *d*-axis current is selected as the state variable to be controlled by the nonlinear time-frequency controller and its desired reference response is obtained through using instantaneous frequency analysis.

6.3 Contribution and Impact of Research

The effectiveness and superiority of the three developed nonlinear time-frequency control schemes have been tested through simulations and experiments. The contribution and impact of their being available are in the following areas:

1. Reduced power requirement for PM electrical machines.

It is demonstrated through simulations that the average input power of the nonlinear time-frequency control scheme developed for PM brushed DC motors are lower than the classical PID control scheme and fuzzy logic control scheme when sensor noises are considered. As for the nonlinear time-frequency control based field oriented control scheme developed for PM synchronous motors. Based on the performance evaluated through both simulation and experiment, the motor controlled by the nonlinear time-frequency control based field oriented control scheme has a lower current ripple than the standard PI control based filed oriented control scheme. This necessarily implied that the

nonlinear time-frequency control based field oriented control scheme imposes a lower switching burden on the associated power electronic devices, thus having a lower power consumption than the standard PI control based field oriented control scheme. The excellent capability of the nonlinear time-frequency chaotic control scheme in reducing the power consumption for the chaotic PM synchronous motor is equally obvious. According to the simulation results, the highly disordered states of the two-pole, three-phase chaotic PM synchronous motor model is successfully suppressed, thus indicative of a reduced power consumption.

2. Enhanced tracking resolution for PM electrical machines.

The excellent speed and position tracking resolution of the nonlinear time-frequency control scheme developed for PM brushed DC motors has been demonstrated by evaluating against the classical PID control scheme and fuzzy logic scheme. It is observed that when sensor noise is present, the nonlinear time-frequency speed control scheme has a better tracking performance than the PID and fuzzy logic speed control schemes. For the nonlinear time-frequency positon control scheme, it acquires a much better performance than the PID position control and fuzzy logic position control schemes regardless of the sensor noise is considered or not. Regarding the nonlinear time-frequency control based field oriented control scheme developed for the speed and position control of PM synchronous motors, both simulation and experiment show that the nonlinear time-frequency control based field oriented control scheme has a lower steady-state error than the standard PI control based field oriented control scheme.

3. Improved stability and robustness for PM electrical machines.

The nonlinear time-frequency speed and position control scheme developed for PM brushed DC motors is shown to have excellent robustness to sensor noise, while the classical PID and fuzzy logic speed and position control schemes do not. As for the nonlinear time-frequency control based field oriented control scheme, compared with the standard PI control based field oriented control scheme, it has less current ripples and is more robust to sudden reference and torque load changes. Lastly, the chaotic response in the chaotic two-pole, three-phase, PM synchronous motor is significantly suppressed by the developed nonlinear time-frequency chaotic control scheme even when the system parameters vary, thus indicative of an improved stability and robustness of the chaotic motor system.

4. Broadening the application area of PM electrical machines.

Based on the aforementioned merits of the three developed nonlinear time-frequency control schemes in terms of tracking resolution, power consumption, stability and robustness, it is expected that PM electrical machines with the nonlinear time-frequency controller can be used under harsh working conditions such as frequent variations of the reference and external torque load, strong noise, and limited power supply, among others, where contemporary control algorithms fail to render satisfactory performance.

5. Expanding the impact of nonlinear time-frequency theory.

The ideal of nonlinear time-frequency control is relatively new. It is initially proposed by Liu and Suh in 2012 for the mitigation of chaotic behaviors in nonlinear dynamical systems. It has since been applied to the precise control of cutting vibration in

macro and nano machining. The three control schemes developed in this dissertation are the first time the nonlinear time-frequency theory is applied to the control of PM electrical machines. It is expected that with the results obtained in this research, the nonlinear time-frequency theory will be widely adopted to enable the ultra-stability control of PM electrical machines mandated in ever-demanding real-world applications.

REFERENCES

1. Eitel L (2015) FAQ: Where do brush DC motors still make sense? Motion ControlTips. http://www.motioncontroltips.com/2015/05/18/faq-where-do-brush-dc-motors-still-make-sense/. Accessed 25 May 2017
2. Murugesan S (1981) An overview of electric motors for space application. IEEE Trans Ind Electron Control Instrum IECI-28(4): 260 - 265
3. Sabir MM, Khan JA (2014) Optimal design of PID controller for the speed control of DC Motor by using metaheuristic techniques. Adv Artifi Neural Syst 2014(126317): 1-8
4. Pérez-Molina M, Pérez-Polo MF (2014) Steady-state, self-oscillating and chaotic behavior of a PID controlled nonlinear servomechanism by using Bogdanov-Takens and Andronov-Poincaré-Hopf bifurcations. Commun Nonlinear Sci Numer Simul 19: 3694-3717
5. Reza AH, Shahram J, Reza SN (2015) DC motor speed control by self-tuning fuzzy PID algorithm. Trans Inst Meas Control 37(2): 164-176
6. Hsu CF, Lee BK (2011) FPGA-based adaptive PID control of a DC motor driver via sliding-mode approach. Expert Syst Appl 38: 11866-11872
7. Zadeh LA (1965) Fuzzy sets. Inf Control 8: 338-353
8. Zadeh LA (1973) Outline of a new approach to the analysis of complex systems and decision processes. IEEE Trans Syst Man Cybern SMC-3(1): 28-44

9. Murugananth GR, Vijayan S (2015) Development of fuzzy controlled chopper drive for permanent magnet DC motor. J Vib Control 21(3): 555-562
10. Prasad KMA, Nair U (2014) Sensor less fuzzy control of DC motor. Nonlinear Dyn 78: 1933-1941
11. Prakash R, Vasanthi R (2015) Speed control of DC-DC converter fed DC motor using robust adaptive intelligent controller. J Vib Control 21(15): 3107-3120
12. Sun WC, Zhang YF, Huang YP, Gao HJ, Kaynak O (2016) Transient-performance-guaranteed robust adaptive control and its application to precision motion control systems. IEEE Trans Ind Electron Control Instrum 63(10): 6510-6518
13. Pillay P, Krishnan R (1991) Application characteristics of permanent magnet synchronous and brushless dc motors for servo drives. IEEE Trans Ind Appl 27(5): 986-996
14. Vu NTT, Choi HH, Jung JW (2012) Certainty equivalence adaptive speed controller for permanent magnet synchronous motor. Mechatronics 22(6): 811-818
15. Perera PDC, Blaabjerg F, Pedersen JK, Thøgersen P (2003) A sensorless, stable V/f control method for permanent-magnet synchronous motor drives. IEEE Trans Ind Appl 39(3): 783-791
16. Ancuti R, Boldea I, Andreescu GD (2010) Sensorless V/f control of high-speed surface permanent magnet synchronous motor drives with two novel stabilising loops for fast dynamics and robustness. IET Electr Power Appl 4(3): 149-157

17. Agarlita SC, Coman CE, Andreescu GD, Boldea I (2013) Stable V/f control system with controlled power factor angle for permanent magnet synchronous motor drives. IET Electr Power Appl 7(4): 278-286
18. Consoli A, Scelba G, Scarcella G, Cacciato M (2013) An effective energy-saving scalar control for industrial IPMSM drives. IEEE Trans Ind Electron 60(9): 3658-3669
19. Krause PC, Wasynczuk O, Sudhoff SD (1995) Analysis of electric machinery. Wiley-IEEE Press, Hoboken
20. Zhou CJ, Quach DC, Xiong NX, Huang S, Zhang Q, et al (2015) An improved direct adaptive fuzzy controller of an uncertain PMSM for web-based e-service systems. IEEE Trans Fuzzy Syst 23(1): 58-71
21. Ananthamoorthy N, Baskaran K (2015) High performance hybrid fuzzy PID controller for permanent magnet synchronous motor drive with minimum rule base. J Vib Control 21(1): 181-194
22. Alexandrou AD, Adamopoulos NK, Kladas AG (2016) Development of a constant switching frequency deadbeat predictive control technique for field-oriented synchronous permanent-magnet motor drive. IEEE Trans Ind Electron 63(8): 5167-5175
23. Mynar Z, Vesely L, Vaclavek P (2016) PMSM model predictive control with field-weakening implementation. IEEE Trans Ind Electron 63(8): 5156-5166

24. Zhang CM, Liu HP, Chen SJ, Wang FJ (2008) Application of neural networks for permanent magnet synchronous motor direct torque control. J Syst Eng Electron 19(3): 555-561
25. Song LP, Zhang R, Luo Y (2009) Direct torque controlling of permanent magnet synchronous motor based on the adaptive fuzzy controller. Fuzzy Inf Eng 2(AISC-62): 393-401
26. Preindl M, Bolognani S (2013) Model predictive direct torque control with finite control set of PM synchronous motor drive systems, part 1: maximum torque per ampere operation. IEEE Trans Ind Informat 9(4): 1912-1921
27. Sivaprakasam A, Manigandan T (2015) An alternative scheme to reduce torque ripple and mechanical vibration in direct torque controlled permanent magnet synchronous motor. J Vib Control 21(5): 855-871
28. Ren HP, Liu D (2006) Nonlinear feedback control of chaos in permanent magnet synchronous motor. IEEE Trans Circuits Syst II Express Briefs 53(1): 45-50
29. Andrievskii BR, Fradkov AL (2003) Control of chaos: methods and applications. I. Methods. Autom Remote Control 64(5): 673-713
30. Ren HP, Liu D, Li J (2003) Delay feedback control of chaos in permanent magnet synchronous motor. Proc Chin Soc Electr Eng 23(6): 175-178
31. Takagi T, Sugeno M (1985) Fuzzy identification of systems and its applications to modeling and control. IEEE Trans Syst Man Cybern SMC-15(1): 116-132
32. Hou YY (2012) Controlling chaos in permanent magnet synchronous motor control system via fuzzy guaranteed cost controller. Abstr Appl Anal 2012(650863): 1-10

33. Yang XH, Liu XP, Liu HS, Xu S (2013) Fuzzy sliding-mode control of chaos in permanent magnet synchronous motor. Int J of Digit Content Technol Appl 7(1): 526-535
34. Hu J, Liu L, Ma DW, Ullah N (2015) Adaptive nonlinear feedback control of chaos in permanent-magnet synchronous motor system with parametric uncertainty. J Mech Eng Sci 229(12): 2314-2323
35. Harb AM (2004) Nonlinear chaos control in a permanent magnet reluctance machine. Chaos Solitons Frac 19(5): 1217-1224
36. Wei Q, Wang XY (2012) Chaos controlling of permanent magnet synchronous motor base on dither signal. J Vib Control 19(16): 2541-2550
37. Liu MK, Suh CS (2012) Simultaneous time-frequency control of bifurcation and chaos. Commun Nonlinear Sci Numer Simul 17(6): 2539-2550
38. Liu MK (2012) Nonlinear time-frequency control theory with applications. Ph.D. Dissertation, Texas A&M University, USA
39. Suh CS, Liu MK (2013) Control of cutting vibration and machining instability: a time-frequency approach for precision, micro and nano machining. Wiley, Hoboken
40. Kuo SM, Morgan DR (1996) Active noise control systems: algorithms and DSP implementations. Wiley, Hoboken
41. Vér IL, Beranek LL (2005) Noise and Vibration Control Engineering: Principles and Applications. Wiley, Hoboken
42. Lueg P (1936) Process of silencing sound oscillations. USA Patent 2043416, 9 Jun 1936

43. Kuo SM, Morgan DR (1999) Active noise control: a tutorial review. Proc IEEE 87(6): 943-973
44. Bochner S, Chandrasekharan K (1949) Fourier transforms. Princeton University Press, Princeton
45. Gröchenig K (2001) Foundations of time-frequency analysis. Springer, Berlin
46. Polikar R (1999) The story of wavelets. In: IMACS/IEEE CSCC'99 proceedings, Marathon, Florida, USA, 25-29 July 1999. pp 5481-5486
47. Polikar R (2001) The wavelet tutorial. http://users.rowan.edu/~polikar/WAVELETS/WTtutorial.html. Accessed 20 May 2017
48. Jensen A, Cour-Harbo A (2001) Ripples in mathematics: the discrete wavelet transformation. Springer, Berlin
49. Attallah S (2000) The wavelet transform-domain LMS algorithm: a more practical approach. IEEE Trans Circuits Syst II Analog Digit Signal Process 47(3): 209-213
50. Wang X, Suh CS (2015) Concurrent Speed and Position Tracking of PM Brushed DC Motors. In: Proceedings of the ASME 2015 International Mechanical Engineering Congress and Exposition, Houston, Texas, USA, 13-19 Nov 2015. vol IMECE2015-50839. pp V04BT04A022
51. Wang X, Suh CS (2016) Nonlinear time-frequency control of PM synchronous motor instability applicable to electrical vehicle application. Int J Dyn Control 4(4): 400-412

52. Wang X, Suh CS (2016) Precision concurrent speed and position tracking of brushed dc motors using nonlinear time-frequency control. J Vib Control. doi: 10.1177/1077546316628974

53. Wang X, Suh CS (2016) Nonlinear time-frequency control of permanent magnet synchronous motors. In: ASME 2016 International Mechanical Engineering Congress and Exposition, Phoenix, Arizona, USA, 11-17 Nov 2016. vol IMECE2016-67363. pp V04BT05A040

54. Wang X, Suh CS (2017) Time-frequency based field oriented control of permanent magnet synchronous motors. Int J Dyn Control. doi: 10.1007/s40435-017-0327-5

55. Mohan N (2012) Electric machines and drives: a first course. Wiley, Hoboken

56. Morales R, Somolinos JA, Sira-Ramírez H (2014) Control of a DC motor using algebraic derivative estimation with real time experiments. Measurement 47: 401-417

57. Keljik JJ (2012) Electricity 4: AC/DC motors, controls, and maintenance. Delmar, New York

58. Ziegler JG, Nichols NB (1993) Optimum Settings for automatic controllers. J Dyn Syst Meas Control 115: 220-222

59. Sekalala S (2006) Performance of a three-phase permanent magnet motor operating as a synchronous motor and a brushless DC motor. Thesis, Louisiana State University, USA

60. Texas Instruments Europe (1998) Field oriented control of three-phase AC-motors. http://www.ti.com/lit/an/bpra073/bpra073.pdf. Assessed 20 May 2017

61. Rahman MA, Vilathgamuwa DM, Uddin MN, Tseng KJ (2003) Nonlinear control of interior permanent-magnet synchronous motor. IEEE Trans Ind Appl 39(2): 408-416
62. Foo G, Rahman MF (2010) Sensorless sliding-mode MTPA control of an IPM synchronous motor drive using a sliding-mode observer and HF signal injection. IEEE Trans Ind Electron 57(4): 1270-1278
63. Cheng B, Tesch TR (2010) Torque feedforward control technique for permanent-magnet synchronous motors. IEEE Trans Ind Electron 57(3): 969-974
64. Jahns TM, Kliman GB, Neumann TW (1986) Interior permanent-magnet synchronous motors for adjustable-speed drives. IEEE Trans Ind Appl IA-22(4): 738-747
65. Peddapelli SK (2016) Pulse Width Modulation. De Gruyter Oldenbourg, Berlin
66. Kumar V, Gaur P, Mittal AP (2014) ANN based self tuned PID like adaptive controller design for high performance PMSM position control. Expert Syst Appl 41(17): 7995-8002
67. Li Z, Zhang B, Tian LF, Mao ZY, Pong MH (1999) Strange attractor in permanent-magnet synchronous motors. In: Proceedings of the IEEE international Conference on Power Electronics and Drive Systems, Hong Kong, China, 27-29 Jul 1999. pp 150-155
68. Li Z, Park JB, Joo YH, Zhang B, Chen GR (2002) Bifurcation and chaos in a permanent-magnet synchronous motor. IEEE Trans Circuits Syst I Fundam Theory Appl 49(3): 383-387

69. Neyram H (1994) Strange attractors in brushless DC motors. IEEE Trans Circuits Syst I Fundam Theory Appl 41(1): 40-45

70. Gao Y, Chau KT (2002) Chaotification of permanent-magnet synchronous motor drives using time-delay Feedback. In: IEEE 28th Annual Conference of the Industrial Electronics Society, Sevilla, Spain, 5-8 Nov 2002. pp 762-766

71. Goedtel A, Silva INd, Serni PJA (2007) Load torque identification in induction motor using neural networks technique. Electr Power Syst Res 77: 35-45

72. Huang NE, Shen Z, Long SR, Wu MC, Shih HH, et al (1998) The empirical mode decomposition and the Hilbert spectrum for nonlinear and non-stationary time series analysis. Proc R Soc Lond A 454: 903-995